Different approaches to improve perovskite-based photovoltaic and optoelectronic devices

Marta Vallés Pelarda

November 2021


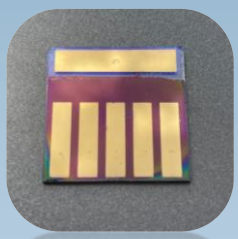
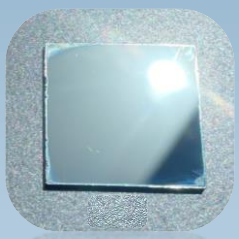

Supervised by:

Prof. Iván Mora Seró

Dr. Eva Maria Barea Berzosa

Programa de Doctorado en Ciencias

Escuela de Doctorado de la Universitat Jaume I

Different approaches to improve perovskite-based photovoltaic and optoelectronic devices

Memoria presentada por Marta Vallés Pelarda **para optar al grado de doctora por la Universitat Jaume I**

Marta Vallés Pelarda

MARTA| VALLES| PELARDA

Firmado digitalmente por MARTA|VALLES|PELARDA
Fecha: 2021.11.16 17:07:51 +01'00'

Prof. Iván Mora Seró

Firmado por IVAN MORA SERO - NIF:33453681C el día 17/11/2021 con un certificado emitido por ACCVCA-120

Dr. Eva María Barea Berzosa

EVA MARIA| BAREA| BERZOSA

Firmado digitalmente por EVA MARIA|BAREA|BERZOSA
Fecha: 2021.11.16 22:46:52 +01'00'

Castelló de la Plana, Noviembre 2021

Financiación

Esta tesis se ha realizado gracias a la financiación recibida por:

- Ayuda Predoctoral para la Formación de Personal Investigador de la Universitat Jaume I, dentro del Plan de promoción de la investigación (FPI-UJI) (PREDOC/2017/40)
- Ayuda para realizar estancias temporales en otros centros de investigación de la Universitat Jaume I, dentro del Plan de promoción de la investigación (E-2018-14)
- No-LIMIT. Boosting photovoltaic performance by the synergistic interaction of halide perovskites and semiconductor quantum dots (ERC-2016-COG-724424)
- Perovskitas fotovoltaicas estabilizadas de alto rendimiento (MAT2016-76892-C3-1-R)
- Desarrollo integral de células solares mesoscópicas y producción de combustible solar (PROMETEOII/2014/020)
- Desarrollo de emisores de luz policristalinos de bajo coste basados en perovskitas de haluro híbridas (MAT2015-70611-ERC)

Thesis by compendium of publications:

- Sebastian F. Völker, Marta Vallés-Pelarda, Jorge Pascual, Silvia Collavini, Fernando Ruipérez, Elisabetta Zuccatti, Luis E. Hueso, Ramón Tena-Zaera, Iván Mora-Seró, Juan Luis Delgado. Fullerene-Based Materials as Hole-Transporting/Electron Blocking Layers. Applications in Perovskite Solar Cells. Chemistry - A European Journal, 2018, 24,34, 8524-8529. DOI: http://dx.doi.org/10.1002/chem.201801069. Impact factor: 5.160 (JCR).

- Sandy Sánchez, Marta Vallés-Pelarda, Jaume-Adrià Alberola-Borràs, Rosario Vidal, José J. Jerónimo-Rendón, Michael Saliba, Pablo P. Boix, Iván Mora-Seró, "Flash infrared annealing as a cost-effective and low environmental impact processing method for planar perovskite solar cells" Materials Today, 31, 39-46 (2019). DOI: https://doi.org/10.1016/j.mattod.2019.04.021. Impact factor: 26.416 (JCR).

- Vallés-Pelarda, M., Gualdrón-Reyes, A. F., Felip-León, C., Angulo-Pachón, C. A., Agouram, S., Muñoz-Sanjosé, V., Miravet, J. F., Galindo, F., Mora-Seró, I., High Optical Performance of Cyan-Emissive CsPbBr3 Perovskite Quantum Dots Embedded in Molecular Organogels. Adv. Optical Mater. 2021, 2001786. https://doi.org/10.1002/adom.202001786. DOI: https://doi.org/10.1002/adom.202001786. Impact factor: 9.926 (JCR, 2020).

This thesis has been accepted by the co-authors of the publications listed above that have waved the right to present them as a part of another PhD thesis.

Contents

Agradecimientos

Lo primero de todo, me gustaría agradecer a mi director Prof. Iván Mora Seró y a mi codirectora Dr. Eva María Barea Berzosa por toda su dedicación, apoyo y tiempo dedicado a este trabajo. Gracias por los consejos y conocimientos que habéis compartido conmigo a lo largo de esta etapa.

Aparte de a mis directores, me gustaría agradecer a todos los miembros del Grupo de Semiconductores Avanzados (GAS) y todos los visitantes que han pasado en estos años, compartiendo su conocimiento y experiencia. De ellos, me gustaría agradecer especialmente a Jesús y Azhar. Por su amabilidad, por esas conversaciones de despacho y por esas intensas conversaciones a primeras horas de la mañana. Y a Rafael Sánchez, por su apoyo y su aportación a este trabajo. Al resto de miembros del Instituto de Materiales Avanzados (INAM) y, por supuesto, al director del instituto, Prof. Juan Bisquert. Además, quería agradecer a toda la gente de Servicios Centrales de Investigación Científica (SCIC) de la UJI que han contribuido a este trabajo.

También agradecer a toda la gente maravillosa que he conocido en mis estancias, tanto en Adolphe Merkle Institute (AMI) como en National Renewable Energy Laboratory (NREL). De AMI, me gustaría agradecer a Dr. Sandy Sanchez por su hospitalidad y ayuda en todo momento. Y por supuesto, a Prof. Michael Saliba, por la oportunidad y su aportación a este trabajo. De NREL, me gustaría agradecer, sobre todo, a Dr. Joey Luther y su equipo, que me acogieron como una más desde el primer día.

Por supuesto, tengo que agradecer a toda la gente que ha estado ahí día a día, animando incluso en los peores momentos. Se ha convertido en una amistad que espero se conserve porque sois lo mejor. Echaré de menos todos esos almuerzos, comidas y momentos compartidos después del trabajo y en los congresos (siempre nos quedará el recuerdo de Benidorm). Agradezco a aquellos que han estado ahí desde el principio, aguantando todas mis locuras, que no han sido pocas: Eva, Loles y Nuria. A aquellos que se han ido incorporando, aunque

reconozco que también han tenido que aguantar muchas: Marisé, Roser, Ramón y Sandra. Y a aquellos que ya están en otras etapas de su vida.

Ha sido una experiencia maravillosa que agradezco de corazón a toda la gente que ha participado de una manera o de otra. A mi familia y amigos, pero, sobre todo, a los dos que más me han apoyado y alegrado la vida. Gracias a todos.

List of Abbreviations

a-Si:H	Amorphous Hydrogenated Silicon
AM	Air Mass
AS	Antisolvent
c-Si	Crystalline Silicon
CB	Conduction Band
CdTe	Cadmium Telluride
CdS	Cadmium Selenide
CIGS	Copper Indium Gallium Selenide
CO_2	Carbon Dioxide
Cs_2CO_3	Caesium carbonate
CuI	Copper(I) Iodide
CuO_2	Cuprous Oxide
CuSCN	Copper(I) Thiocyanate
DMF	Dimethylformamide
DMSO	Dimethyl sulfoxide
DSSCs	Dye Sensitized Solar Cells
EDX	Energy-Dispersive X-Ray
ETM	Electron Transporting Material
FA	Formamidinium
FF	Fill Factor
FIRA	Flash Annealed Infrared Annealing
FTIR	Fourier Transform Infrared
FTO	Fluoride-doped Tin Oxide
GaAs	Gallium Arsenide
GaSe	Gallium Selenide
GBL	Gamma-butyrolactone
GO	Graphene Oxide
HI	Hot Injection
HOMO	Highest Occupied Molecular Orbital
HTM	Hole Transporting Material
IR	Infrared
IS	Impedance Spectroscopy
ITO	Indium-doped Tin Oxide
J-V	Current density-Voltage
J_{mp}	Current density at Maximum Power

J_{sc}	Short Circuit Current density
LARP	Ligand Assisted Reprecipitation
LED	Light Emitting Diode
Li-TFSI	Lithium bis(trifluoromethylsulphonyl) imide
LUMO	Lowest Unoccupied Molecular Orbital
MA	Methylammonium
MAI	Methylammonium Iodide
$MAPbI_3$	Methylammonium Lead Iodide
MoO_x	Molybdenum Oxide
NC	Nanocrystal
NiO_x	Nickel(II) Oxide
NIR	Near Infrared
NMP	N-methyl-2-pyrrolidone
OPV	Organic Photovoltaic
P3HT	Poly(3-hexylthiophene)
$PbBr_2$	Lead (II) Bromide
PbI_2	Lead (II) Iodide
PbS	Lead (II) Sulfide
PbSe	Lead (II) Selenide
PCBM	[6,6]-phenyl-C_{61}-butyric acid methyl ester
PEDOT:PSS	Poly(3,4-ethylenedioxythiophene):poly(styrene sulfonic) acid
PL	Photoluminescence
PLQY	Photoluminescence Quantum Yield
PNC	Perovskite Nanocrystal
PSC	Perovskite Solar Cell
PTAA	Poly[bis(4-phenyl)(2,4,6-trimethylphenyl)amine]
QD	Quantum Dot
QDSSC	Quantum Dot Sensitized Solar Cell
SAED	Selected Area Diffraction
SC	Solar Cell
SEM	Scanning Electron Microscopy
Spiro-OMeTAD	2,2′,7,7′-tetrakis(N,N-di-p-methoxyphenylamine)-9,9′-spirobifluorene
TAA	Triarylamine
tBP	4-tertbutylpyridine
TCO	Transparent Conductive Oxide

TEM	Transmission Electron Microscopy
TRPL	Time Resolved Photoluminescence
TiO_2	Titanium dioxide
UV	Ultraviolet
UV-Vis	Ultraviolet-Visible
VB	Valence Band
V_{mp}	Voltage at Maximum Power
V_{oc}	Open Circuit Voltage
VO_x	Vanadium Oxide
WO_3	Tungsten Oxide
XRD	X-Ray Diffraction

Abstract

Halide perovskites have had a huge impact on different fields in the last decade due to their versatility and amazing optoelectronic properties. In the case of solar cells, in the last years they have reached efficiencies comparable to the other most efficient existent photovoltaic technologies.[1] Since 2009 when the first perovskite solar cell was developed with an efficiency of 3%[2], they have achieved efficiencies over 25%.[1] But these materials, both bulk and low dimensional materials, like quantum dots, are not only appropriate for photovoltaic applications, due to their outstanding properties, they have also been applied to LEDs[3], lasers[4] and detectors.[5] Nevertheless, there are still some issues to improve towards their future utilization and commercialization in large scale systems.

In this thesis, three of these issues to improve perovskite-based devices are addressed. In relation to the first work, perovskite quantum dots have been studied, owing to their suitable properties for the different mentioned applications. $CsPbBr_3$ perovskite quantum dots have been embedded in two different molecular organogels. One of them shows a strong effect on the optoelectronic properties of the nanoparticles, varying the emission from green to blue.[6]

The second issue studied is the replacement of the most employed hole transporting material in perovskite solar cells, spiro-OMeTAD, by a fullerene derivative, which are usually employed as electron transporting materials. The devices are characterized and compared with reference devices with spiro-OMeTAD, both efficiency and stability. The use of fullerene derivatives shows an improvement in the stability of the devices.[7]

In the last study, a method for the deposition and formation of the perovskite layer in solar cells, compatible with large scale processes, is studied. It has been evaluated the impact of this methodology on the properties of the perovskite film and the final devices. Besides having similar performance and properties, this new method reduces the cost and time of the preparation of the solar cells.[8]

These studies provide an overview of the versatility of these materials and highlight how a focused research can further improve the already excellent properties of halide perovskite materials and devices.

Resumen

Las perovskitas de haluro han revolucionado diferentes campos debido a su gran versatilidad y propiedades optoelectrónicas excepcionales. En el caso de las celdas solares, en los últimos años se han conseguido alcanzar eficiencias comparables a las otras tecnologías fotovoltaicas más eficientes existentes .[1] Desde el 2009 donde se obtuvo un 3% de eficiencia[2], se han alcanzado ya valores superiores al 25%.[1] Pero no solo son apropiados para su aplicación en fotovoltaica tanto en bulk como en materiales de baja dimensionalidad, como los puntos cuánticos, sino que, debido a sus propiedades extraordinarias, se han abierto camino en otras aplicaciones como en LEDs[3], láseres[4] y detectores.[5] Sin embargo, hay ciertos aspectos que se pueden mejorar de cara a su futura utilización y comercialización a gran escala.

En esta tesis se van a tratar tres de esos aspectos para mejorar dispositivos basados en perovskita. En relación al primer trabajo, se han estudiado sistemas con nanopartículas de perovskita, dadas sus magníficas propiedades para las diferentes aplicaciones mencionadas. Puntos cuánticos de $CsPbBr_3$ son introducidos en dos organogeles moleculares similares. Uno de ellos muestra un efecto sobre las propiedades de las nanopartículas, variando su emisión de verde a azul.[6]

El segundo aspecto estudiado es el reemplazo del material más utilizado como transportador de huecos en celdas solares basadas en perovskita, spiro-OMeTAD, por un fullereno funcionalizado, que normalmente se utiliza como transportador de electrones. Los dispositivos se han caracterizado y comparado en términos de eficiencia y estabilidad con dispositivos de referencia con spiro-OMeTAD. El uso de este tipo de materiales muestra un aumento en la estabilidad de las muestras.[7]

En el último trabajo se ha estudiado un método de deposición y formación de la capa de perovskita en celdas solares compatible con procesos a gran escala. Se ha evaluado el impacto que tiene esta metodología en las propiedades de la perovskita y en los dispositivos finales. Además de presentar eficiencia y propiedades similares, este método reduce el coste y el tiempo de preparación de los dispositivos.[8]

Estos estudios aportan una visión sobre la versatilidad de estos materiales y enfatizan como se pueden mejorar las ya excelentes propiedades de las perovskitas y dispositivos.

References

[1] NREL Best Research-Cell Efficiency Chart, https://www.nrel.gov/pv/assets/pdfs/best-research-cell-efficiencies.20200104.pdf, accessed: Mar., 2021.

[2] A. Kojima, K. Teshima, Y. Shirai, T. Miyasaka, *J. Am. Chem. Soc.* **2009**, *131*, 6050.

[3] K. Zhang, N. Zhu, M. Zhang, L. Wang, J. Xing, *J. Mater. Chem. C* **2021**, *9*, 3795.

[4] S. Yakunin, L. Protesescu, F. Krieg, M. I. Bodnarchuk, G. Nedelcu, M. Humer, G. De Luca, M. Fiebig, W. Heiss, M. V Kovalenko, *Nat. Commun.* **2015**, *6*, 8056.

[5] Q. Chen, J. Wu, X. Ou, B. Huang, J. Almutlaq, A. A. Zhumekenov, X. Guan, S. Han, L. Liang, Z. Yi, J. Li, X. Xie, Y. Wang, Y. Li, D. Fan, D. B. L. Teh, A. H. All, O. F. Mohammed, O. M. Bakr, T. Wu, M. Bettinelli, H. Yang, W. Huang, X. Liu, *Nature* **2018**, *561*, 88.

[6] M. Vallés-Pelarda, A. F. Gualdrón-Reyes, C. Felip-León, C. A. Angulo-Pachón, S. Agouram, V. Muñoz-Sanjosé, J. F. Miravet, F. Galindo, I. Mora-Seró, *Adv. Opt. Mater.* **2021**, *n/a*, 2001786.

[7] S. F. Völker, M. Vallés-Pelarda, J. Pascual, S. Collavini, F. Ruipérez, E. Zuccatti, L. E. Hueso, R. Tena-Zaera, I. Mora-Seró, J. L. Delgado, *Chem. – A Eur. J.* **2018**, *24*, 8524.

[8] S. Sánchez, M. Vallés-Pelarda, J.-A. Alberola-Borràs, R. Vidal, J. J. Jerónimo-Rendón, M. Saliba, P. P. Boix, I. Mora-Seró, *Mater. Today* **2019**, *31*, 39.

Chapter 1. Introduction

1.1. Brief introduction to solar cells and perovskites

Nowadays, the world is constantly changing and adapting to the new technologies that are emerging. This has an impact on the global energy demand, added to the population growth, which is increasing significantly as a consequence. Actually, the most employed energy sources are still fossil fuels among other non-renewable sources. These energy sources generate CO_2 and other gas emissions, which are associated to greenhouse effect, climate change and global warming. All these concerns are more and more present every day. For that, renewable energies are taking an important role in our society and research is focused on developing new technologies to take advantage of renewable sources like solar, wind, biomass, geothermal and hydropower energy.

Solar energy is one of the best alternatives to non-renewable energies because it is an unlimited and inexhaustible source, from which we are not taking full advantage. As an example, the energy consumed by humankind in one year is the energy that the sun supplies in one hour. Despite the benefits of solar energy, there are still some key points that need to be improved. These aspects are technological, environmental and economic; which are still issues to solve for a better inclusion of this energy.[1–3]

Solar energy can be converted to heat, electricity and solar fuels. Solar cells (SCs) are the devices that convert solar energy directly to electricity. The basis of these devices is the so-called photovoltaic effect. Essentially, it is the generation of electric voltage when light shines on the cell.[3,4] Over the last 45 years, different types of solar cells have been studied and improved as shown in Figure 1.1. In the last 10 years, some emergent photovoltaic technologies have gained visibility due to the fact that they have reached relatively high efficiencies in a short period of time.

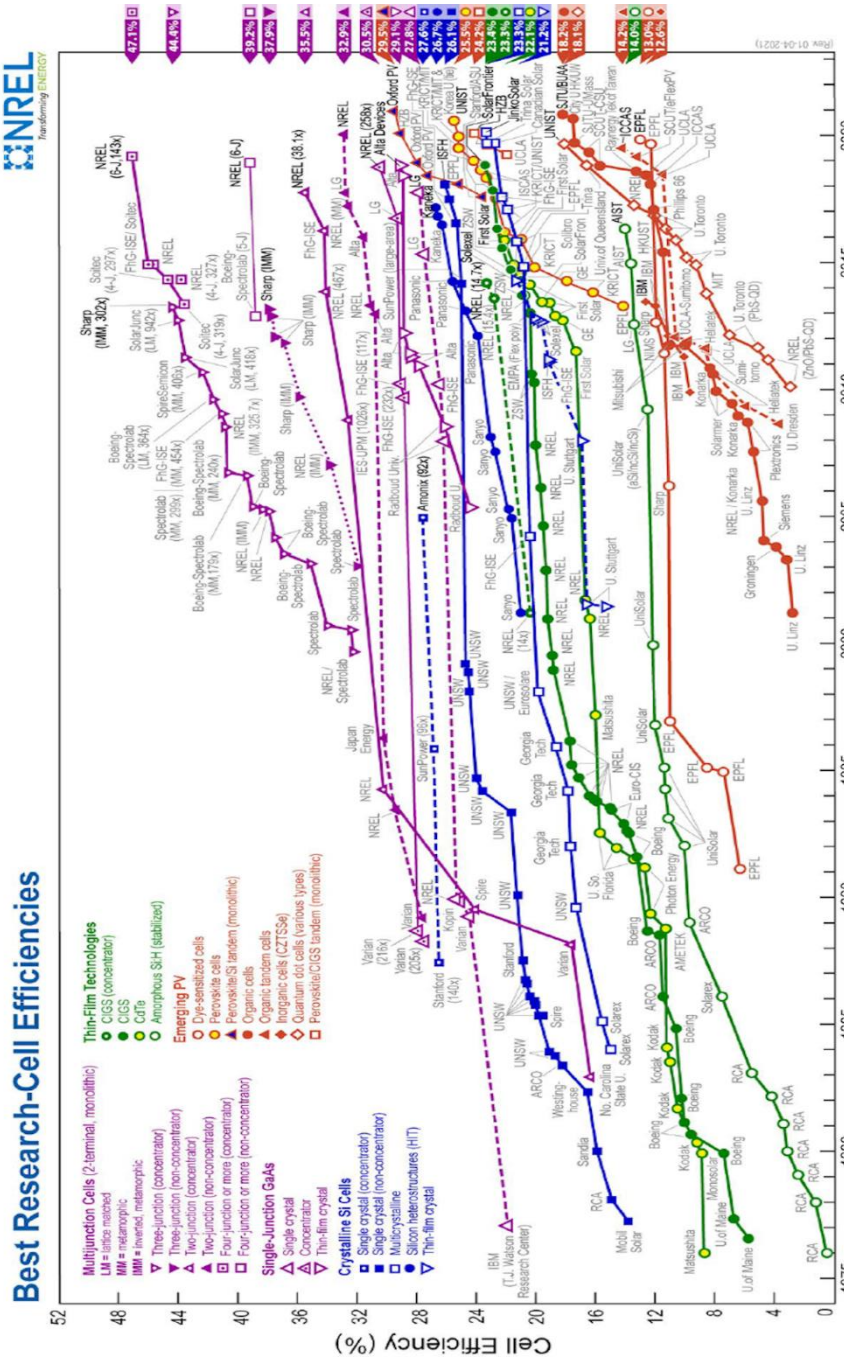

Figure 1.1. Solar cell efficiency chart from 1976 to 10/03/2021. This plot is courtesy of the National Renewable Energy Laboratory, Golden, CO.[5]

All this research for the different technologies is due to the necessity of fulfilling some requirements for an ideal solar cell. The main features for an ideal solar cell are: [4]

- The absorber material is a direct band gap semiconductor with energy band gap between 1.1-1.7eV. In the case of a single absorber, the highest theoretical efficiency is obtained for a band gap close to 1.34eV.[6,7] Direct band gap semiconductors are those in which the valence band (VB) and the conduction band (CB) are aligned with the same momentum, as shown in Figure 1.2.[8]
- The materials are available and non-toxic.
- The methods employed in its fabrication are low-cost, reproducible and allow large scale production.
- The device has a high photovoltaic conversion efficiency.
- The solar cell is long-term stable.

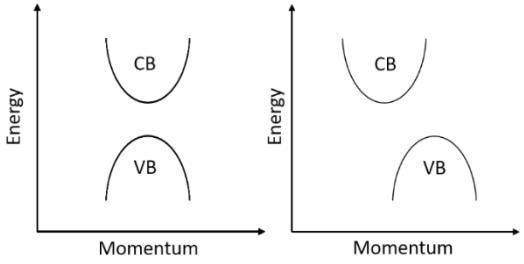

Figure 1.2. Scheme of a direct (left) and indirect (right) band gap semiconductor.

As commented, an important issue to consider is the Shockley-Queisser limit. In 1961, William Shockley and Hans-Joachim Queisser first calculated the maximum efficiency that a single absorber SCs could achieve. The maximum theoretical efficiency is achieved with semiconductors with a band gap of 1.34eV.[6,7]

Solar cells are commonly classified in three generations, based on the time they appeared. First generation solar cells are crystalline silicon solar cells (c-Si) and gallium arsenide solar cells (GaAs). The second-

generation solar cells are thin-film technologies like copper indium gallium selenide solar cells (CIGS), cadmium telluride (CdTe) and hydrogenated amorphous silicon (a-Si:H). The emerging thin film photovoltaics are the third generation. It refers to quantum dot (QD), organic photovoltaics (OPV), dye-sensitized solar cells (DSSCs) and hybrid inorganic-organic perovskite and nanocrystals.[9,10] Below, a brief description of them is exposed.

Crystalline silicon solar cell is one of the most commercialized devices for several reasons, such as the abundance of this material, the photo-conversion efficiency and long-term stability. However, it is an indirect band gap semiconductor with a band gap energy of 1.11eV and the quality needed for high efficiency and the amount of material are prejudicial for the cost, despite the massive production has reduced enormously the fabrication cost in the last years.[3,9,11,12] There are different types of crystalline Si solar cells: single crystal, crystalline thin film, polycrystalline and heterostructures.[13]

Gallium arsenide solar cells are other type of monocrystalline solar cells that in fact reported the highest efficiency.[5] The advantage of this semiconductor is that has a direct bandgap around 1.43eV and a high absorption coefficient, which implies the possibility of using films of micrometres instead of hundreds of micrometres as in crystalline Si solar cells. In addition, this material has a good resistance to radiation and heat. The main drawback of this technology is the high cost of producing it in the necessary monocrystalline form to avoid recombination losses, which makes large scale production nonprofitable; besides the toxicity of arsenic.[13–15]

In CIGS solar cells, the absorber composition is $CuIn_{1-x}Ga_xSe_2$, where a percentage of indium has been replaced by gallium. This permits to tune the band gap from 1.04 to 1.7eV. It is a direct band gap semiconductor with high absorption coefficient.[16] It presents benign defect physics allowing a relatively high efficiency polycrystalline films, with a cost reduction as polycrystalline film fabrication is less demanding than monocrystalline one.[17] It can be deposited on top of different substrates (from glass to flexible substrates). However, the

materials needed to fabricate them are not abundant and at least a thickness of 1µm of CIGS is employed, which can cause an increase in the cost. In addition, large scale productions are not easily performed due to the uniformity of the film, which translates to lower efficiencies than Si cells.[16]

Cadmium telluride is also a direct band gap semiconductor and has also a high absorption coefficient. The band gap is around 1.45eV, close to the ideal values for solar cells. Compared to other thin film technologies, it has an easy and low-cost deposition and manufacture; however, the main drawback is the toxicity caused by the cadmium and the low abundance of tellurium.[13,18–20]

Hydrogenated amorphous Si is also a direct band gap material and low-cost technology. Even though in this case the band gap (around 1.7eV) is higher than the crystalline Si (1.1eV) and efficiencies are lower. This technology has been developed in different types of SCs: tandem, double or triple junctions. It is suitable for glass or flexible substrates, which is an advantage despite the efficiency.[18,20]

Dye-sensitized solar cells (DSSCs) consist of a dye sensitizing a nanostructured material (usually TiO_2), an electrolyte (in a solution or a polymer) and a counter electrode. When the dye absorbs a photon, an electron is excited from the HOMO (highest occupied molecular orbital) to the LUMO (lowest unoccupied molecular orbital). The electron is injected to the conduction band of the nanostructured material and the electron transport occurs until it reaches the electrode. The electrolyte, the most common is the redox couple (I_3^-/ I^-), regenerates the dye. The oxidized form diffuses to the counter electrode where it is reduced with the electrons. These solar cells can be semi-transparent, low cost and applicable to flexible substrates. However, the light absorption of the dye molecules is limited to its chemical structure, until now a dye that absorbs all the radiation from the solar spectrum that reaches the earth has not been designed. This has a direct consequence on the efficiencies. In addition, the long term stability of the devices is not the desired, mostly due to the use of a liquid electrolyte.[21–23]

Quantum dot solar cells are another emerging photovoltaic technology. Different types of these solar cells have been developed: metal-semiconductor or Schottky junction cells, heterojunction solar cells and QD sensitized solar cells (QDSSCs). In the Schottky junction cells, the QDs are between a layer of a transparent metal oxide and a metal. In the heterojunction solar cells, different types are studied. On one hand, quantum junctions are studied, which can be of the same material but doped to achieve p-type and n-type materials. On the other hand, depleted heterojunctions are employed, such as oxide/QDs, organic/QDs and bulk heterojunctions. In QDSSCs, the QDs are sensitizing the surface of a semiconductor metal oxide, the electron transporting material. The quantum dots employed as absorbing material are usually binary compounds, like lead sulfide (PbS)[24,25], lead selenide (PbSe)[26] or cadmium sulfide (CdS)[27], among others. The most important advantage of this technology is the ability to tune the band gap of the QDs varying their size or shape. However, one of the limitations of these materials is that it is not easy to achieve an appropriate band gap width and conduction edge, and reduce recombination. In order to solve this problem, researchers started to use QD alloys, core-shell structures or other materials like perovskite nanocrystals.[28–31]

Organic photovoltaics (OPV) are slightly different to the other solar cells. This type employs organic molecules as absorbers, either small molecules or polymers. As they have low dielectric constant, when absorbing light, they generate electron-hole pairs that are bounded by coulomb interaction (excitons) that have limited diffusion lengths (around 10nm). To dissociate these charges, a two-component system is needed, which consists in an electron donor and electron acceptor. It is a lightweight low-cost technology which uses solution processes and flexible substrates. Among the main drawbacks, they have poor stability and the polymers employed are not quite reproducible. In addition, they still have relatively low efficiency. However, a significant increase of the performance has been reported in the last years, see Figure 1.1, mostly due to the use of non-fullerene electron transporting materials.[21,32]

In this context, perovskite solar cells have irrupted in the last decade as one of the most promising solar cells for their high efficiency achieved in a relatively short research period. Perovskites were first used in 2009 as an electrolyte in a dye-sensitized solar cell. The efficiency was quite low, almost 4%.[33] With the work by Im *et al.*[34] higher efficiencies were reported. However, a significant breakthrough was attained with the works of Kim *et al.*[35] and Lee *et al.*[36], which presented their work with perovskites in film, avoiding the liquid electrolyte in DSSC configuration that was the problem of previous perovskite devices stability. Since that moment, an impressive effort has been made to increase these low efficiencies until an efficiency of 25.5%.[5] Their unique properties make them valuable for optoelectronic applications. Apart from this, the processes involved in the preparation of this technology are solution-based and low temperature, which is also an advantage towards their large-scale production and commercialization.[37]

1.2. Perovskite

Perovskite is the name of a type of crystalline structure which formula is ABX_3. In this case, "A" is a monovalent cation either organic or inorganic like cesium (Cs^+), methylammonium ($CH_3NH_3^+$, MA) or formamidinium ($CHN_2H_4^+$, FA). "B" is a metal ion like lead (Pb^{+2}), tin (Sn^{+2}) or germanium (Ge^{+2}). And "X" is a halide (iodide (I^-), bromide (Br^-) or chloride (Cl^-)). Depending on the "A" cation, they can be classified into two types: hybrid organic-inorganic perovskite and inorganic perovskite.[9] The first compositions employed for perovskite solar cells were $MAPbI_3$ and $MAPbBr_3$.[33] Lead halide perovskites are the most common due to the instability of Sn-based and Ge-based perovskites, as they get easily oxidized in ambient air.[38]

Perovskites show different crystalline phases depending on the temperature, for example, $MAPbI_3$ shows three different phases: α phase (cubic), β phase (tetragonal) and γ phase (orthorhombic).[39,40] Figure 1.3 shows the cubic symmetry for perovskites. Halide atoms (red spheres) are disposed on the vertex of an octahedron, in which centre a lead ion (grey sphere) is located.[9]

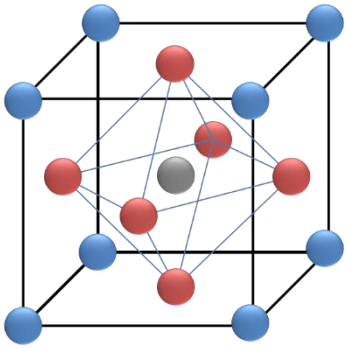

Figure 1.3. Perovskite cubic structure. Halides are represented by red spheres; blue spheres represent the monovalent cation and grey sphere represents the metal ion.

To have the required crystal perovskite symmetry, Goldschmidt defined a tolerance factor that perovskites must fulfil. This tolerance factor (τ) was defined as[41]:

$$\tau = \frac{R_a + R_x}{\sqrt{2}\,(R_b + R_x)}$$

where R_a is the ionic radius of the "A" cation, R_b is the ionic radius of the "B" cation and R_x are the ionic radius of the "X" anion. [9,42] However, it is not the only parameter that should be considered. Li *et al.*[43] defined the octahedral factor as:

$$\mu = \frac{R_b}{R_x}$$

Although with these two parameters, the phase stability of the different perovskites could be predicted,[44] in a recent work, Bartel *et al.* developed a more complex tolerance factor which also predicts the perovskite stability.[45]

The tolerance factor required to have the perovskite structure is $0.8<\tau<1$ and the octahedral factor $0.44<\mu<0.90$.[42,43] Lower or greater tolerance factor implies a non-perovskite tetragonal or hexagonal phase, respectively.[46] The tolerance factors of perovskites like $CsPbI_3$ and $FAPbI_3$ are close to the limits and exhibit a non-perovskite phase, also called yellow phase, at room temperature due to lattice distortion.[42,47,48] To stabilize these structures, different approaches have been studied: compositional engineering, low dimensional materials and external additives.[49] With compositional engineering, the mixture of cations is used to reduce the effective cationic radius, a small percentage of methylammonium and cesium is added to $FAPbI_3$-based solar cell.[48,50] Another composition that has been studied is also introducing a small amount of rubidium (Rb).[51]

The second approach to stabilize the perovskite black phase of these compositions is using low dimensional materials. $CsPbI_3$ and $FAPbI_3$ nanocrystals have proven that it is possible to obtain the photoactive phase of these materials at room temperature.[49,52] And the last one is the addition of additives of different nature. Among them, bulky cations[53], chemical stabilizers[54] and other QDs[55,56] have been used and proven the improvement of the stability.[49] Bulky cations lead to 2D perovskites, it results in a 2D/3D mixture which sometimes does not modify the band gap.[49,57]

Regarding the stability of these materials, the most stable perovskite films are the ones with cesium as cation, due to its inorganic nature. It is worth to mention that, as explained with the tolerance and octahedral factors, $CsPbI_3$ perovskite phase films are not stable in ambient conditions, there is a phase transition from cubic to orthorhombic non-perovskite phase. About the organic cations, according to its nature, the film stability varies. For example, $FAPbX_3$ are more stable than $MAPbX_3$. This fact is attributed to the volatile species formed by $MAPbX_3$ decomposition, while the species formed by $FAPbX_3$ decomposition are less volatile.[58]

Concerning the properties of these materials, perovskites present direct band gap, one of the properties described for ideal absorbers for photovoltaics.[9] According to the Shockley-Queisser limit[6], $MAPbI_3$ band gap (around 1.55eV) or FAPbI3 band gap (around 1.48eV) are close to the appropriate band gap for photovoltaic applications.[59] But this is not the only property suitable for their application to photovoltaics and optoelectronics. Regarding the optical properties of the perovskite, it has high absorption coefficient, even higher than other inorganic materials (Si, GaAs) in the visible region. This enables the use of hundreds of nanometres instead of microns as in Si solar cells.[9,37,59,60] In addition, its band gap can be tuned obtaining different absorption edges/emissions which is valuable for the applications of perovskites.[9] Moreover, the electronic properties of these materials are also attractive for optoelectronic applications. Among them, halide perovskites have benign defect physics, allowing that polycrystalline films have low trap density, high mobility and high diffusion length.[60] It is a defect tolerant material unlike other semiconductors, which implies that the defects do not form electrically active mid-gap states.[61] Another advantage is that the processes involved could be low temperature and low cost.[37,59]

As mentioned above, the band gap of this material can be easily tuned. It can be achieved with different methodologies: compositional engineering and modifying the morphology. In compositional engineering, it is possible to change the halide (X), the cation (A) and the metal ion (B), however, the latter is less employed due to the oxidation of the other alternatives. Changing the halide has the strongest effect on the band gap energy (see Figure 1.4).[60] As an example, in $MAPbX_3$ perovskites only changing the halide from iodide to bromide, the band gap is tuned from 1.5eV to 2.02eV.[37] In A-site changes, $FAPbI_3$, $MAPbI_3$ and $CsPbI_3$ show a band gap of 1.48eV, 1.52eV and 1.67eV, respectively. This is attributed to the distortions in the structure by the cation size.[47,48,62] Another approach to modify the band gap is modifying the morphology of the materials to low dimensional materials.[63] Below, in section 1.2.1, this will be explained in detail.

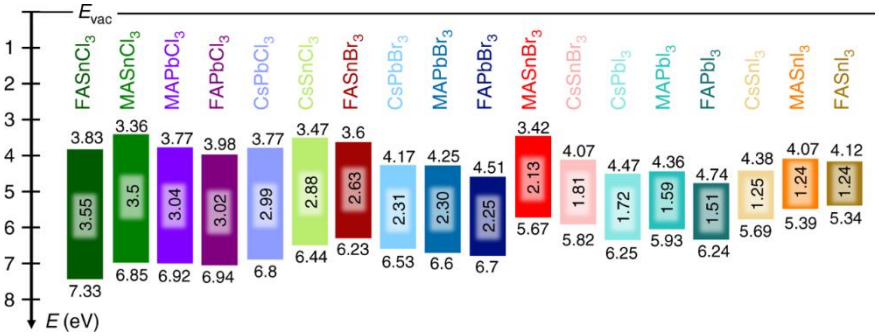

Figure 1.4. Band gap energies of different perovskites. Reproduced from ref.[64], under Creative Commons license http://creativecommons.org/licenses/by/4.0/. Copyright 2019, The Author(s).

1.2.1. Perovskite Quantum Dots

Nanocrystals are those particles whose size is in the nanoscale range. These nanoparticles are referred as quantum dots when one or more dimensions are around or below the excitonic Bohr radius and quantum confinement effect is shown.[65] These materials can be divided depending on the confined dimensions into 0D (quantum dots), 1D (nanowires) and 2D (nanoplatelets, nanosheets).[63]

This effect, quantum confinement, implies that the bandgap of the semiconductor increases when the size is decreased and, consequently, the optical and electronic properties of these materials vary significantly.[66] This feature is interesting for optoelectronic and photovoltaic applications because the emission/absorption edge can be tuned, obtaining a wide range of emissive nanoparticles.

Perovskite nanocrystals (NCs) embedded in a solid matrix were first reported in the 1990s, however, it was not until perovskites were employed as absorbers in SCs that they got more attention.[65,67–70] In 2014, $MAPbBr_3$ colloidal NCs were synthesized by Schmidt *et al.*[71], but it was in 2015 when Protesescu *et al.*[72] successfully synthesized $CsPbX_3$ colloidal QDs with high photoluminescence quantum yield (PLQY) and narrow emission. Colloidal syntheses allowed the preparation of PNCs with very high crystal quality. In 2017, Protesescu *et al.*[73] and Chen *et al.*[74] also demonstrated the possibility of tuning the emission from blue to NIR with colloidal $FA_yCs_{1-y}PbX_3$ PNCs.

Figure 1.5 shows a picture of some PQDs solutions and PL emission spectra, it exhibits the effect of halide in their emission.

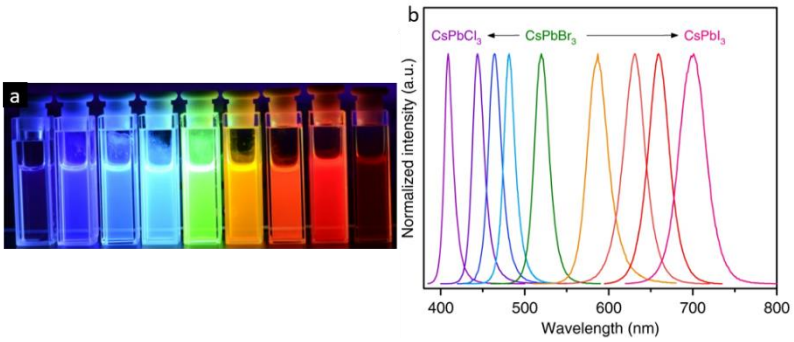

Figure 1.5. a) Picture of $CsPbX_3$ solutions under UV excitation. b) PL spectra of the different solutions. Adapted from ref.[75], under Creative Commons license http://creativecommons.org/licenses/by/4.0/. Copyright 2018, The Author(s).

Nowadays, all perovskite QDs show narrow emission and high PLQY for the visible range and NIR. However, for blue emitting unmodified chloride-based perovskites lower PLQY is reported due to defect states.[76] $CsPbX_3$ QDs have an additional interest. As mentioned before, the excitonic Bohr diameter is determining in the variation of the optical and electronic properties of the QDs. In this case, it is up to 12 nm, which permits the tunability of their emission within the entire visible range.[77]

A great effort has been dedicated to synthesize blue-emissive QDs with high PLQY, because these are the only ones with low efficiency. In Chapter 3, highly emissive $CsPbBr_3$ perovskite QDs are presented. Blue and green emissive QDs are obtained after embedding them in two different molecular organogels.

There are different methodologies to prepare PQDs, however, the most commonly used are ligand assisted reprecipitation (LARP) method[78] and hot injection (HI) method[72]. LARP consists in dissolving the precursor salts and ligands in a good solvent and dropping this solution into a solvent where the NCs precipitate. It is a room temperature technique, however, in this methodology the polar solvents employed usually dissolve or degrade the perovskite NCs.[65]

The HI method was already employed in the synthesis of other NCs. In this method, a precursor solution is heated in a high boiling solvent and another precursor solution is rapidly injected in an inert atmosphere. This method enables obtaining monodispersed size-controlled materials. It has several parameters to control the size and shape of the NCs, such as the ratio between ligands, the reaction temperature and the concentration of the precursors.[65,77]

These techniques employ organic ligands to stabilize the PQDs, the most common capping ligands are oleylamine and oleic acid. Although these ligands stabilize and protect the QDs, they are not suitable for the application of these materials to photovoltaic devices or light emitting diodes. They limit the transport properties needed for a good performance of the devices. This is solved by removing part of these ligands with purification steps, which are basically reprecipitation processes. A balance between high PLQY, stability and charge transport must be studied to reach high efficiency devices. Previous reports show that this can be achieved with two purifications with ethyl acetate or methyl acetate.[79,80]

1.2.2. Applications

Due to the intrinsic electronic and optical properties mentioned before, together with the low cost and facile synthesis, they have many applications in the photovoltaic and optoelectronic fields. Some of the applications of perovskites are shown in Figure 1.6. For each application, the requirements are different and the film composition and deposition are key factors.

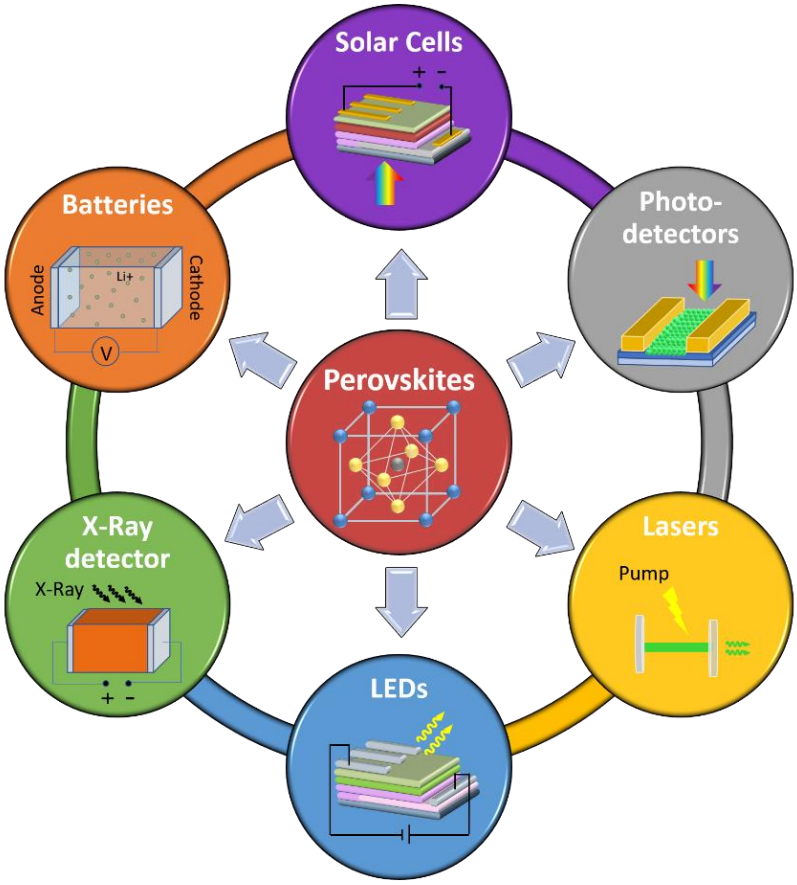

Figure 1.6. Scheme of the different applications of perovskites.

The most studied application is in the photovoltaic field. As mentioned before, in the last decade, the efficiency of this emerging technology has reached 25.5%.[5] PSCs have been successfully prepared using both perovskite bulk and QDs films.[60,81]

The other application that has been widely studied is in Light Emitting Diodes (LEDs). PNCs have attracted more attention owing to the optical properties, specially the high PLQY, narrow emission bandwidth and tunability of these materials.[60,82] There are three factors important for an efficient LED: high stability, PLQY and efficient charge injection. This can be achieved by the purification steps to remove part of the ligands, as aforementioned.[83]

In addition, they have been studied in lasers and photodetectors. Photodetectors are devices sensitive to light or other electromagnetic waves. The material should have a high carrier mobility and lifetime, to extract the carriers before they recombine, and these fit in with perovskites.[83] Lasers are emitting devices whose light is optically amplified through stimulated emission. In this case, the perovskite (especially $CsPbX_3$ NCs) properties which awakened the interest in this field were the size tunability and the amplified spontaneous emission at room temperature in the visible range. [83,84]

They have also been employed in X-ray detection and imaging. They have been used as scintillators and direct conversion detectors because they are X-ray sensitive, due to the high atomic number of the elements forming the perovskite, and have high absorption coefficient.[85–87] Moreover, they have been studied in lithium-ion batteries. In a lithium-ion battery, in presence of a bias, ions move to the anode and intercalate in the structure, which we know as charging. In the discharge cycle, the ions move back to the cathode. Some reports have tested perovskite materials as electrode, showing structural stability when ions intercalate and in the charge/discharge cycles. [87]

1.3. Perovskite solar cells

Perovskite solar cells (PSCs) have been fabricated in a broad range of configurations. For the most extended configurations, the different layers are shown in Figure 1.7a: a transparent conductive oxide (TCO), an electron transporting material (ETM), an absorber (perovskite), a hole transporting material (HTM) and a metal contact. The TCO is a material that should have high transmittance and low sheet resistance. The most employed are fluoride-doped tin oxide (FTO) and indium-doped tin oxide (ITO). The ETM acts as selective contact allowing the electron transport to the contact and blocking the hole transport. In an analogous way, the HTM blocks the electrons and allows the hole transport to the metal contact. Both materials must be good selective contacts to avoid recombination. The light absorber is a semiconductor, in this case a perovskite.

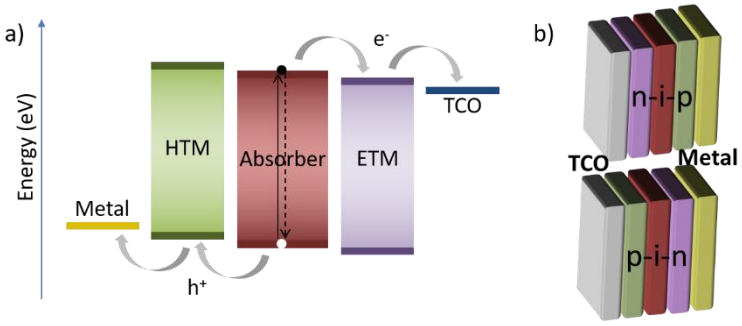

Figure 1.7. a) Scheme of the different layers and main processes involved in the solar cell. b) Different architectures of solar cells.

Figure 1.7a shows the main processes involved in the solar cell, light absorption and charge separation. When the light is absorbed, electrons are excited to the conduction band of the perovskite and electron-hole pairs are generated. These photogenerated charges must be selectively extracted by the HTM and ETM before they recombine.[21,88] Then, the charge transport takes place and the charges go to the contacts. One important characteristic of the ETM and HTM is shown in the scheme, the band alignment that they should have with the perovskite.[60]

There are two types of architectures: regular (n-i-p) and inverted (p-i-n), see Figure 1.7b. In regular architectures, the n-type semiconductor is below the perovskite and on top the p-type semiconductor. In this configuration, the most common materials are TiO_2 or SnO_2 as ETMs and Spiro-OMeTAD as HTM. Whereas in the inverted or p-i-n architectures, the p-type semiconductor is below the perovskite layer and on top the n-type semiconductor. The most common materials employed in this configuration are PEDOT:PSS or NiO_x (HTM) and PCBM (ETM).

On the other hand, they can also be classified into planar or mesoscopic structures. Planar devices are composed by thin films, while mesoscopic devices incorporate a layer of nanoparticles before the perovskite layer, either hole or electron transporting material.[21,88]

Apart from the composition and phase of the perovskite layer, its quality is also a key factor for the efficiency of the solar cells. Good film quality can be determined by the homogeneity and crystallinity.[21] One factor that affects the quality of the perovskite layer is the charge transporting layer below the perovskite (in n-i-p the ETM and in p-i-n HTM).[60]

Beyond the photovoltaic efficiency, a solar cell has to prove a significant long-term stability. Regarding the stability of this type of solar cells, several works have focused on addressing this issue. Degradation of perovskite solar cells is mainly due to: UV light,[89,90] moisture,[91] oxygen,[91] electric field[92,93] and temperature[94,95] [88,96,97]. Oxygen and moisture degradation could be prevented by encapsulation, however, it increases the cost of the solar cell and does not solve all the stability issues. An alternative to that, the HTM or other hydrophobic layers deposited on top could be a possible solution to protect the perovskite layer.[97]

A recent study by Akbulatov *et al.*[58] showed a comparison of the stability of different perovskite solar cells. They studied the effect of thermal annealing and light soaking and observed the cation plays an important role on the stability as mentioned above. The results they

obtained also indicate that other layers such as the electron/hole transporting layers can prevent part of the degradation, as above-mentioned. In addition, they demonstrated that the interfaces are a key point for the stability of the devices.[58,98]

Apart from the thermal instability of certain perovskite compositions, spiro-OMeTAD is another important issue.[97] There are also some degradation processes that take place under illumination, both in the perovskite layer and the other ones.[94,99]

Another objection that concerns society about this technology is the toxicity of lead. The most employed perovskite light absorber contains lead, as already discussed, and other commercialized photovoltaic technologies employ toxic elements on their devices, such as CIGS, GaAs, GaSe and CdTe; and it is a point that should be controlled looking for recyclability and safety. Moreover, the amount of lead in PSCs is low compared to these other technologies that use lead or other toxic materials.[97] Although lead-free perovskites have been also tested as absorber, they currently present lower stability and have lower efficiency, but both aspects are continuously increasing in the last reports.[100]

1.3.1. Hole Transporting Materials

Hole transporting materials are in charge of extracting the holes from the absorber and injecting them to the metal. And so, they have to meet some requirements for a good performance of the devices. First of all, they should have high hole mobility, which translates to a reduction of losses and recombination. Besides, the HOMO (for polymers or organic molecules) or the valence band (for inorganic materials) should be close to the valence band of the perovskite to minimize losses. In addition, it should be thermally stable and resistant to moisture and oxygen. In regular architectures, this feature is especially important, as it protects the active layer from both moisture or oxygen. Apart from these properties, it should involve low cost

processes and low-cost materials. There are different possibilities when referring to the different architectures of the solar cells.[96,101,102]

The most employed hole transporting material in regular PSSCs is a small organic molecule called Spiro-OMeTAD (2,2′,7,7′-tetrakis(N,N-di-p-methoxyphenylamine)-9,9′-spirobifluorene). Some of the main advantages are its rigid structure and its high solubility. However, this molecule has low charge mobility and conductivity. For that reason, some additives are employed to solve this issue, such as lithium bis(trifluoromethylsulfonyl) imide (Li-TFSI), 4-tertbutylpyridine (tBP) and Co(III) complexes. Although they improve the properties, they are also one of the reasons of its degradation and the degradation of the device.[38] For example, it has been reported that lithium salt accelerates the oxidation of spiro-OMeTAD, which favours the hole mobility.[103] However, as it is highly hygroscopic, it enables the water penetration into the layer. tBP prevents this hydration and the aggregates of the lithium salt inside the layer, but it is volatile so the amount decreases with time. It can also react with the perovskite layer, forming complexes with PbI_2.[104,105] Regarding the cobalt complexes, they also oxidize spiro-OMeTAD and improve the hole mobility.[88,96,101,106–108]

Apart from the detrimental effect of the dopants on the layer, there are other disadvantages. It is an expensive material due to the processes and materials involved, the layer is not thermally stable[95] and other issues like UV light degradation[89] have been reported.[101,109] A recent work reported an alternative to the use of dopants with spiro-OMeTAD, preparing the layer by vacuum sublimation and improving the stability of the layer. However, it needs to be optimized to achieve the efficiency of solution-processed spiro-OMeTAD.[110] In any case, despite these drawbacks, spiro-OMeTAD is a good HTM at lab scale, as provides high performance but alternatives are needed for a future scalability,

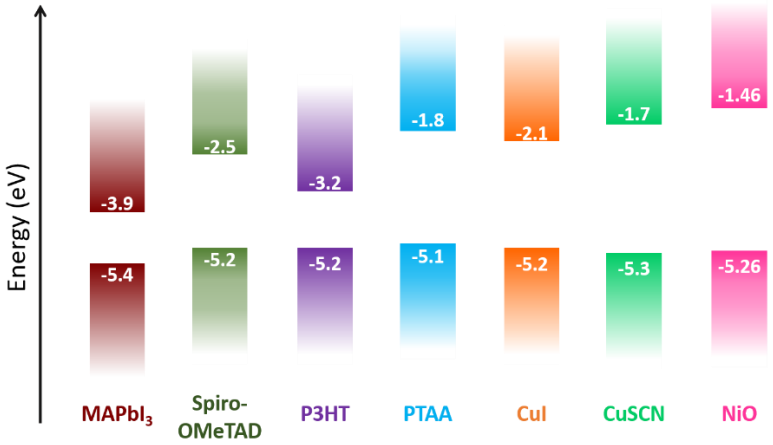

Figure 1.8. Energy levels of some HTMs employed in perovskite solar cells compared with $MAPbI_3$ VB and CB. Original figure can be found at ref.[111], under Creative Commons license http://creativecommons.org/licenses/by/4.0/; the figure has been modified.

To replace the spiro-OMeTAD, other small molecules, polymers or even p-type inorganic semiconductors have been reported, see Figure 1.8. The advantage of the small molecules is that the synthesis and purification is controllable, which translates to reproducibility. One of the derivatives studied are triarylamine derivatives, to which spiro-OMeTAD also belongs. They are good electron donors, making them suitable for a hole transporting material. They can be classified depending on their structure in: spiro-type, star-shaped, four-armed and linear.[112] Recently, two star-shaped triarylamine derivatives were reported as an alternative to spiro-OMeTAD, but the dopants (lithium salt, tBP and Co complex) was required to obtain a comparable efficiency with the reference.[113] Other type of organic molecules that have been studied as HTM is thiophene derivatives. Zhang *et al.*[114] reported two molecules with efficiencies close to the one with spiro-OMeTAD. Other ones that have been studied are carbazole derivatives. One example is the work of Liu *et al.*[115], which reported several molecules based on carbazole-arylamine with good performance. Despite the effort to substitute spiro with these organic molecules and other types, most of them need the addition of dopants.[96,112]

Polymeric materials are usually deposited in solution and at low temperatures, which make them suitable for flexible substrates. Moreover, they have good hole mobility due to the conjugated structures. The most well-known polymeric materials are poly(3,4-ethylenedioxythiophene):poly(styrene sulfonic) acid (PEDOT:PSS), poly[bis(4-phenyl)(2,4,6-trimethylphenyl)amine] (PTAA) and poly(3-hexylthiophene) (P3HT). PTAA, P3HT and PEDOT:PSS are polymeric forms of two types of small molecules mentioned before, triarylamines and thiophenes. PTAA is one of the best choices; the performance of the solar cells is comparable to the ones with spiro-OMeTAD, showing thermal stability. On the other hand, in this case dopants are also needed and its costs is even higher than for spiro-OMeTAD.[38,88,116] PEDOT:PSS shows an appropriate HOMO level, transparency and flexibility. On the other hand, it is hygroscopic, not stable and its acidic behaviour can cause the etching of the substrates.[117] P3HT is a low cost alternative, however, pure P3HT has low hole mobility and conductivity.[96,101,107,118,119]

P-type inorganic semiconductors are the other alternative. They are usually wide bandgap materials and have the advantages of being thermally and chemically stable. In addition, they present high hole mobility, high conductivity and they are usually dopant-free. As inorganic materials, the materials reported are copper(I) thiocyanate (CuSCN)[120], nickel(II) oxide (NiO_x)[121], copper(I) iodide (CuI)[122], graphene oxide (GO)[119], molybdenum oxide (MoO_x)[123], vanadium oxide (VO_x)[124], tungsten oxide (WO_3) and cuprous oxide (Cu_2O). The main drawback of this kind of materials is the deposition in regular architectures. They are not usually soluble in solvents that do not damage or dissolve the perovskite layer and they need sometimes an annealing process to form a good quality layer. In inverted configurations, other deposition techniques like spray-pyrolysis could be employed to obtain thin films. However, these methods are at high temperature, which is a disadvantage for the overall cost.[96,101,118,125]

In polymers, as well as in small organic molecules, there is a huge field that could be explored by molecular engineering. In this work, we have chosen, as a proof of concept, a fullerene derivative functionalized with TAA fragments to act as hole transporting material. In OPV, fullerenes and derivatives have been employed as acceptors, as well as electron transport layers in PSCs.[32,126] It demonstrated to passivate traps in perovskite surface and grain boundaries.[88,126] Fullerenes have a hydrophobic nature which could prevent, to a certain extent, moisture to permeate. Consequently, fullerene derivatives could improve this protection against moisture.[126] In this case, as it will be explained in Chapter 4, a fullerene derivative is successfully employed to replace spiro-OMeTAD, without additives. Note that this HTM has the additional interest of using a fullerene derivative as electron blocking layer, while this family of materials is well known for the development of hole blocking systems. Consequently, this work also broadens the application of this family of materials with potential implications for the development of other system or devices.

1.3.2. Fabrication. Deposition techniques

There are several techniques developed to deposit bulk perovskite films. The deposition of the perovskite layer is a crucial step in the preparation of any perovskite-based device. The quality of the film is essential for good performances. The deposition techniques can be classified into two categories: single-step and two-step deposition. The single-step deposition is the most employed owing to the compositional engineering to prepare different perovskite layers. In Figure 1.9, a scheme of some one-step deposition techniques is shown. Perovskite precursors are usually dissolved in an aprotic polar solvent (dimethylformamide (DMF), dimethyl sulfoxide (DMSO), gamma-butyrolactone (GBL), N-methyl-2-pyrrolidone (NMP)). This solution is spin-coated on top of a conductive oxide coated with an electron/hole transporting layer and then the film is annealed. However, this method is not suitable for large area devices. For that reason, some modifications to this deposition have been developed.[9,46,97]

One modification of the single-step deposition is antisolvent crystallization, it increases the growth rate and nucleation, improving the crystallinity. In this case, the crystallization is caused by an antisolvent dripping in the spin-coating process. Different antisolvents have been tested, such as chlorobenzene, diethyl ether, ethanol or toluene among others. Although these methods are the most employed, they are not suitable for large area devices.[37,97]

Another technique that is performed in one step is thermal evaporation.[127] In this technique, the precursor salts are evaporated simultaneously under vacuum. However, the evaporation of some precursors like MAI are not easy to control. One approach employed was forming first the lead salt film and then evaporate the other precursor. Although this improved the performance, it implies a time increase and a two-step deposition. Both techniques present disadvantages, lead salt require high temperature to evaporate and high vacuum.[9,97]

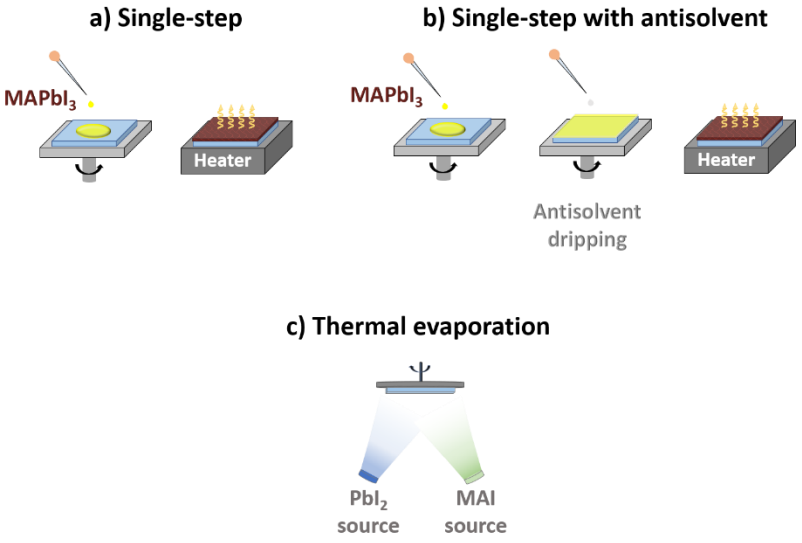

Figure 1.9. One-step deposition techniques for perovskite films. a) Single-step deposition: spin-coat the solution followed by a heating step. b) Single-step deposition with antisolvent: antisolvent dripping while spin-coating the solution followed by a heating step. c) Thermal evaporation: evaporation of both precursors.

Two-step deposition[128] consists in depositing first a layer of a lead precursor and then it is exposed to the other precursor and forms the perovskite layer. In Figure 1.10, some two-step techniques are outlined. The second step is usually spin-coated or dip-coated. One variant of this technique is vapor assisted deposition[129], in which the second step for $MAPbI_3$ preparation is made by exposing the lead iodide film to vapor of MAI at 150ºC in an inert atmosphere. But this technique has some drawbacks, it requires vacuum and the gas-solid reaction could last hours, two inconvenient features for large scale manufacturing.[9,97]

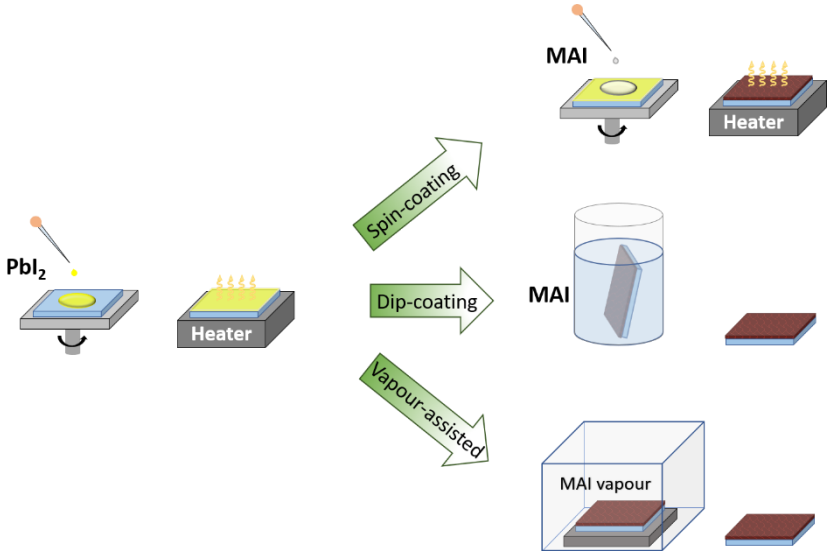

Figure 1.10. Two-step deposition methods for perovskite films. First step common: spin-coat PbX_2 solution followed by heating step. Second step: spin-coat and heat, dip-coat and vapour-assisted.

There are other techniques, usually in one step as shown in Figure 1.11, which are suitable for large area manufacturing. For example, one technique consists in drop casting[130] the perovskite solution on the substrate followed by an annealing to evaporate the solvent. But this technique should be automated to have reproducible results and the performance of the devices is not high.[97]

Another large-scale deposition technique is doctor blade coating.[131] In this case, the perovskite solution is poured on the substrate and a glass blade is swiped to distribute the perovskite. Here, the substrate needs to be heated to obtain uniform and pinhole free films.[97]

Inkjet printing[132] is the other technique for large scale manufacturing. This technique is based on printing using a perovskite ink. Among the main advantages, it does not require specific substrate shapes and it is low-cost and scalable with the possibility of different designs/patterns.[97] Recent works have reported the use of this technique in PSCs. Although an efficiency of 19.6% was achieved, the preparation of the ink is a complex process.[133]

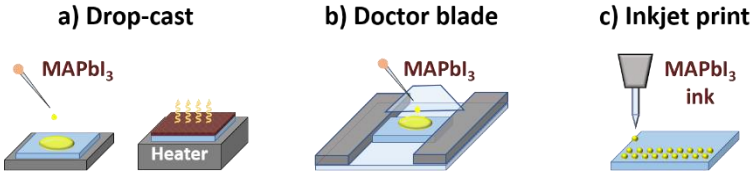

Figure 1.11. Scheme of some large-scale deposition techniques: a) drop-cast; b) doctor blade, similar to drop-casting but a blade spreads the solution, and c) inkjet print.

Most of the techniques introduced described have a final common step, the annealing, to remove the residual solvents and favour the crystallization. This could last from minutes to more than an hour. In Chapter 5, a technique called Flash Infrared Annealing (FIRA) is an industry-friendly technology employed to prepare perovskite solar cells. This technique is based on the annealing in a short time (less than 2 seconds for perovskite films) with IR, suitable for large area solar cells. This results in a fast crystallization of the perovskite film almost without increasing the substrate temperature, which enables the use of this technique also in flexible substrates. This is compared to the most employed perovskite film deposition technique for high efficiency devices: the antisolvent one-step deposition. PSCs are prepared by both techniques and characterized in order to compare and analyse the different properties.

1.4. Objectives

In the last decades, there has been an increasing energy demand and the most employed technologies are still based on the use of fossil fuels. The environmental impact and the scarcity of fossil fuels has motivated researchers to continue with the development of new technologies. It is important to keep studying new materials and improving the devices that are employed in these fields to take maximum benefit of their properties. In this work, different aspects of perovskite-based materials and devices will be treated: stability, cost and performance. The main objectives of this work are:

- Replace materials employed in perovskite solar cells that could cause the device degradation and could increase the overall cost, such as spiro-OMeTAD.

- Study techniques that could be applied to large scale procedures with low environmental impact and low cost. These should not have a detrimental effect on the performance.

- Synthesize and characterize stable perovskite quantum dots with good optoelectronic properties for their application in different fields.

1.5. Structure of the Thesis

This study is focused on the preparation and characterization of materials/devices for the photovoltaic and optoelectronic field. This thesis is divided in six chapters:

- Chapter 1 Introduction: A general introduction is presented. We started with a brief summary of the state of the art and the main issues that motivated this work is included. Also, it includes an overview of the main topic of this work: perovskites and some applications.

- Chapter 2 Characterization techniques: A description of the techniques employed to characterize the materials and devices prepared is introduced.
- Chapter 3 Publication 1: In this chapter, the first article is presented. In this work, 'High optical performance of cyan-emissive $CsPbBr_3$ perovskite quantum dots embedded in molecular organogels', perovskite quantum dots are embedded in two different molecular organogels showing a different behavior in each one. A stable blue emissive material with high PLQY is obtained.
- Chapter 4 Publication 2: Here, the second article is presented. In this work, 'Fullerene-Based Materials as Hole-Transporting/Electron Blocking Layers. Applications in Perovskite Solar Cells', the use of an alternative HTM will be described. In this case, a fullerene-derivative successfully replaces the usual HTM (spiro-OMeTAD), with the additional advantage that does not require any additive.
- Chapter 5 Publication 3: In this chapter, the last article is presented. In this work, 'Flash infrared annealing as a cost-effective and low environmental impact processing method for planar perovskite solar cells', a new methodology to prepare perovskite films is evaluated. It is demonstrated that it is possible to obtain high quality films and high-performance devices with this low-cost and low-environmental impact technique.
- Chapter 6 Discussion of the results: The results obtained in the different works are generally discussed in this chapter.
- Chapter 7 General conclusions: The conclusions of this work are exposed.

References

[1] G. K. Singh, *Energy* **2013**, *53*, 1.

[2] N. Kannan, D. Vakeesan, *Renew. Sustain. Energy Rev.* **2016**, *62*, 1092.

[3] M. B. Hayat, D. Ali, K. C. Monyake, L. Alagha, N. Ahmed, *Int. J. Energy Res.* **2019**, *43*, 1049.

[4] A. Goetzberger, J. Luther, G. Willeke, *Sol. Energy Mater. Sol. Cells* **2002**, *74*, 1.

[5] NREL Best Research-Cell Efficiency Chart, https://www.nrel.gov/pv/assets/pdfs/best-research-cell-efficiencies.20200104.pdf, accessed: Mar., 2021.

[6] W. Shockley, H. J. Queisser, *J. Appl. Phys.* **1961**, *32*, 510.

[7] S. Rühle, *Sol. Energy* **2016**, *130*, 139.

[8] G. Chen, J. Seo, C. Yang, P. N. Prasad, *Chem. Soc. Rev.* **2013**, *42*, 8304.

[9] S. A. Olaleru, J. K. Kirui, D. Wamwangi, K. T. Roro, B. Mwakikunga, *Sol. Energy* **2020**, *196*, 295.

[10] W. C. Sinke, *Renew. Energy* **2019**, *138*, 911.

[11] Y. Kato, S. Fujimoto, M. Kozawa, H. Fujiwara, *Phys. Rev. Appl.* **2019**, *12*, 24039.

[12] A. Goodrich, P. Hacke, Q. Wang, B. Sopori, R. Margolis, T. L. James, M. Woodhouse, *Sol. Energy Mater. Sol. Cells* **2013**, *114*, 110.

[13] N. Asim, K. Sopian, S. Ahmadi, K. Saeedfar, M. A. Alghoul, O. Saadatian, S. H. Zaidi, *Renew. Sustain. Energy Rev.* **2012**, *16*, 5834.

[14] E. Radziemska, *Prog. Energy Combust. Sci.* **2003**, *29*, 407.

[15] A. L. Greenaway, J. W. Boucher, S. Z. Oener, C. J. Funch, S. W. Boettcher, *ACS Energy Lett.* **2017**, *2*, 2270.

[16] J. Ramanujam, U. P. Singh, *Energy Environ. Sci.* **2017**, *10*, 1306.

[17] M. Raghuwanshi, R. Wuerz, O. Cojocaru-Mirédin, *Adv. Funct. Mater.* **2020**, *30*, 2001046.

[18] T. D. Lee, A. U. Ebong, *Renew. Sustain. Energy Rev.* **2017**, *70*, 1286.

[19] V. Fthenakis, C. Athias, A. Blumenthal, A. Kulur, J. Magliozzo, D. Ng, *Renew. Sustain. Energy Rev.* **2020**, *123*, 109776.

[20] L. El Chaar, L. A. lamont, N. El Zein, *Renew. Sustain. Energy*

Rev. **2011**, *15*, 2165.
[21] C. Wu, K. Wang, M. Batmunkh, A. S. R. Bati, D. Yang, Y. Jiang, Y. Hou, J. G. Shapter, S. Priya, *Nano Energy* **2020**, *70*, 104480.
[22] S. Shalini, R. Balasundaraprabhu, T. S. Kumar, N. Prabavathy, S. Senthilarasu, S. Prasanna, *Int. J. Energy Res.* **2016**, *40*, 1303.
[23] M. Yahya, A. Bouziani, C. Ocak, Z. Seferoğlu, M. Sillanpää, *Dye. Pigment.* **2021**, 109227.
[24] C. Zhou, Y. Geng, Q. Chen, J. Xu, N. Huang, Y. Gan, L. Zhou, *Mater. Lett.* **2016**, *172*, 171.
[25] R. Mastria, A. Rizzo, C. Giansante, D. Ballarini, L. Dominici, O. Inganäs, G. Gigli, *J. Phys. Chem. C* **2015**, *119*, 14972.
[26] W. Ahmad, J. He, Z. Liu, K. Xu, Z. Chen, X. Yang, D. Li, Y. Xia, J. Zhang, C. Chen, *Adv. Mater.* **2019**, *31*, 1900593.
[27] J. Kim, H. Choi, C. Nahm, J. Moon, C. Kim, S. Nam, D.-R. Jung, B. Park, *J. Power Sources* **2011**, *196*, 10526.
[28] P. V Kamat, *J. Phys. Chem. C* **2008**, *112*, 18737.
[29] J. S. Shaikh, N. S. Shaikh, S. S. Mali, J. V Patil, S. A. Beknalkar, A. P. Patil, N. L. Tarwal, P. Kanjanaboos, C. K. Hong, P. S. Patil, *ChemSusChem* **2019**, *12*, 4724.
[30] H. Lee, H.-J. Song, M. Shim, C. Lee, *Energy Environ. Sci.* **2020**, *13*, 404.
[31] D. A. R. Barkhouse, R. Debnath, I. J. Kramer, D. Zhitomirsky, A. G. Pattantyus-Abraham, L. Levina, L. Etgar, M. Grätzel, E. H. Sargent, *Adv. Mater.* **2011**, *23*, 3134.
[32] K. A. Mazzio, C. K. Luscombe, *Chem. Soc. Rev.* **2015**, *44*, 78.
[33] A. Kojima, K. Teshima, Y. Shirai, T. Miyasaka, *J. Am. Chem. Soc.* **2009**, *131*, 6050.
[34] J.-H. Im, C.-R. Lee, J.-W. Lee, S.-W. Park, N.-G. Park, *Nanoscale* **2011**, *3*, 4088.
[35] H.-S. Kim, C.-R. Lee, J.-H. Im, K.-B. Lee, T. Moehl, A. Marchioro, S.-J. Moon, R. Humphry-Baker, J.-H. Yum, J. E. Moser, M. Grätzel, N.-G. Park, *Sci. Rep.* **2012**, *2*, 591.
[36] M. M. Lee, J. Teuscher, T. Miyasaka, T. N. Murakami, H. J. Snaith, *Science (80-.).* **2012**, *338*, 643 LP.
[37] M. I. H. Ansari, A. Qurashi, M. K. Nazeeruddin, *J. Photochem. Photobiol. C Photochem. Rev.* **2018**, *35*, 1.
[38] T. Miyasaka, A. Kulkarni, G. M. Kim, S. Öz, A. K. Jena, *Adv. Energy Mater.* **2020**, *10*, 1902500.
[39] G. Niu, X. Guo, L. Wang, *J. Mater. Chem. A* **2015**, *3*, 8970.

[40] P. Cottingham, R. L. Brutchey, *Chem. Mater.* **2018**, *30*, 6711.
[41] V. M. Goldschmidt, *Naturwissenschaften* **1926**, *14*, 477.
[42] Q. Tai, K.-C. Tang, F. Yan, *Energy Environ. Sci.* **2019**, *12*, 2375.
[43] C. Li, X. Lu, W. Ding, L. Feng, Y. Gao, Z. Guo, *ACTA Crystallogr. Sect. B-STRUCTURAL Sci. Cryst. Eng. Mater.* **2008**, *64*, 702.
[44] W. Travis, E. N. K. Glover, H. Bronstein, D. O. Scanlon, R. G. Palgrave, *Chem. Sci.* **2016**, *7*, 4548.
[45] C. J. Bartel, C. Sutton, B. R. Goldsmith, R. Ouyang, C. B. Musgrave, L. M. Ghiringhelli, M. Scheffler, *Sci. Adv.* **2019**, *5*, eaav0693.
[46] N. Torabi, A. Behjat, Y. Zhou, P. Docampo, R. J. Stoddard, H. W. Hillhouse, T. Ameri, *Mater. Today Energy* **2019**, *12*, 70.
[47] C. C. Stoumpos, C. D. Malliakas, M. G. Kanatzidis, *Inorg. Chem.* **2013**, *52*, 9019.
[48] J.-P. Correa-Baena, M. Saliba, T. Buonassisi, M. Grätzel, A. Abate, W. Tress, A. Hagfeldt, *Science (80-.).* **2017**, *358*, 739 LP.
[49] S. Masi, A. F. Gualdrón-Reyes, I. Mora-Seró, *ACS Energy Lett.* **2020**, *5*, 1974.
[50] M. Saliba, T. Matsui, J.-Y. Seo, K. Domanski, J.-P. Correa-Baena, M. K. Nazeeruddin, S. M. Zakeeruddin, W. Tress, A. Abate, A. Hagfeldt, M. Grätzel, *Energy Environ. Sci.* **2016**, *9*, 1989.
[51] M. Saliba, T. Matsui, K. Domanski, J.-Y. Seo, A. Ummadisingu, S. M. Zakeeruddin, J.-P. Correa-Baena, W. R. Tress, A. Abate, A. Hagfeldt, M. Grätzel, *Science (80-.).* **2016**, *354*, 206 LP.
[52] A. Swarnkar, A. R. Marshall, E. M. Sanehira, B. D. Chernomordik, D. T. Moore, J. A. Christians, T. Chakrabarti, J. M. Luther, *Science (80-.).* **2016**, *354*, 92 LP.
[53] C. Shen, Y. Wu, S. Zhang, T. Wu, H. Tian, W.-H. Zhu, L. Han, *Sol. RRL* **2020**, *4*, 2000069.
[54] Q. Wang, X. Zheng, Y. Deng, J. Zhao, Z. Chen, J. Huang, *Joule* **2017**, *1*, 371.
[55] M. Liu, Y. Chen, C.-S. Tan, R. Quintero-Bermudez, A. H. Proppe, R. Munir, H. Tan, O. Voznyy, B. Scheffel, G. Walters, A. P. T. Kam, B. Sun, M.-J. Choi, S. Hoogland, A. Amassian, S. O. Kelley, F. P. García de Arquer, E. H. Sargent,

Nature **2019**, *570*, 96.

[56] S. Masi, C. Echeverría-Arrondo, K. M. M. Salim, T. T. Ngo, P. F. Mendez, E. López-Fraguas, D. F. Macias-Pinilla, J. Planelles, J. I. Climente, I. Mora-Seró, *ACS Energy Lett.* **2020**, *5*, 418.

[57] J. Rodríguez-Romero, J. Sanchez-Diaz, C. Echeverría-Arrondo, S. Masi, D. Esparza, E. M. Barea, I. Mora-Seró, *ACS Energy Lett.* **2020**, *5*, 1013.

[58] A. F. Akbulatov, L. A. Frolova, N. N. Dremova, I. Zhidkov, V. M. Martynenko, S. A. Tsarev, S. Y. Luchkin, E. Z. Kurmaev, S. M. Aldoshin, K. J. Stevenson, P. A. Troshin, *J. Phys. Chem. Lett.* **2020**, *11*, 333.

[59] Q. Chen, N. De Marco, Y. (Michael) Yang, T.-B. Song, C.-C. Chen, H. Zhao, Z. Hong, H. Zhou, Y. Yang, *Nano Today* **2015**, *10*, 355.

[60] S. Rhee, K. An, K.-T. Kang, *Cryst.* **2021**, *11*, DOI: 10.3390/cryst11010039.

[61] M. V Kovalenko, L. Protesescu, M. I. Bodnarchuk, *Science (80-.).* **2017**, *358*, 745 LP.

[62] Z. Yang, J. Song, H. Zeng, M. Wang, *Mater. Today Energy* **2019**, *14*, 100338.

[63] C. Zhang, D.-B. Kuang, W.-Q. Wu, *Small Methods* **2020**, *4*, 1900662.

[64] S. Tao, I. Schmidt, G. Brocks, J. Jiang, I. Tranca, K. Meerholz, S. Olthof, *Nat. Commun.* **2019**, *10*, 2560.

[65] J. Shamsi, A. S. Urban, M. Imran, L. De Trizio, L. Manna, *Chem. Rev.* **2019**, *119*, 3296.

[66] D. Bera, L. Qian, T.-K. Tseng, P. H. Holloway, *Mater.* **2010**, *3*, DOI: 10.3390/ma3042260.

[67] M. Nikl, K. Nitsch, K. Polák, E. Mihókova, S. Zazubovich, G. P. Pazzi, P. Fabeni, L. Salvini, R. Aceves, M. Barbosa-Flores, R. P. Salas, M. Gurioli, A. Scacco, *J. Lumin.* **1997**, *72–74*, 377.

[68] M. Nikl, K. Nitsch, K. Polak, G. P. Pazzi, P. Fabeni, D. S. Citrin, M. Gurioli, *Phys. Rev. B* **1995**, *51*, 5192.

[69] M. Nikl, K. Polak, K. Nitsch, G. P. Pazzi, P. Fabeni, M. Gurioli, *Radiat. Eff. Defects Solids* **1995**, *135*, 289.

[70] Q. A. Akkerman, G. Rainò, M. V Kovalenko, L. Manna, *Nat. Mater.* **2018**, *17*, 394.

[71] L. C. Schmidt, A. Pertegás, S. González-Carrero, O. Malinkiewicz, S. Agouram, G. Mínguez Espallargas, H. J.

Bolink, R. E. Galian, J. Pérez-Prieto, *J. Am. Chem. Soc.* **2014**, *136*, 850.

[72] L. Protesescu, S. Yakunin, M. I. Bodnarchuk, F. Krieg, R. Caputo, C. H. Hendon, R. X. Yang, A. Walsh, M. V Kovalenko, *Nano Lett.* **2015**, *15*, 3692.

[73] L. Protesescu, S. Yakunin, S. Kumar, J. Bär, F. Bertolotti, N. Masciocchi, A. Guagliardi, M. Grotevent, I. Shorubalko, M. I. Bodnarchuk, C.-J. Shih, M. V Kovalenko, *ACS Nano* **2017**, *11*, 3119.

[74] D. Chen, X. Chen, Z. Wan, G. Fang, *ACS Appl. Mater. Interfaces* **2017**, *9*, 20671.

[75] W. Zheng, P. Huang, Z. Gong, D. Tu, J. Xu, Q. Zou, R. Li, W. You, J.-C. G. Bünzli, X. Chen, *Nat. Commun.* **2018**, *9*, 3462.

[76] N. Mondal, A. De, A. Samanta, *ACS Energy Lett.* **2019**, *4*, 32.

[77] D. Chen, X. Chen, *J. Mater. Chem. C* **2019**, *7*, 1413.

[78] D. Xu, Q. Wan, S. Wu, Y. Zhao, X. Xu, L. Li, G. He, *RSC Adv.* **2020**, *10*, 17653.

[79] J. Li, L. Xu, T. Wang, J. Song, J. Chen, J. Xue, Y. Dong, B. Cai, Q. Shan, B. Han, H. Zeng, *Adv. Mater.* **2017**, *29*, 1603885.

[80] E. M. Sanehira, A. R. Marshall, J. A. Christians, S. P. Harvey, P. N. Ciesielski, L. M. Wheeler, P. Schulz, L. Y. Lin, M. C. Beard, J. M. Luther, *Sci. Adv.* **2017**, *3*, eaao4204.

[81] M. Hao, Y. Bai, S. Zeiske, L. Ren, J. Liu, Y. Yuan, N. Zarrabi, N. Cheng, M. Ghasemi, P. Chen, M. Lyu, D. He, J.-H. Yun, Y. Du, Y. Wang, S. Ding, A. Armin, P. Meredith, G. Liu, H.-M. Cheng, L. Wang, *Nat. Energy* **2020**, *5*, 79.

[82] X. Wang, Z. Bao, Y.-C. Chang, R.-S. Liu, *ACS Energy Lett.* **2020**, *5*, 3374.

[83] D. Yang, M. Cao, Q. Zhong, P. Li, X. Zhang, Q. Zhang, *J. Mater. Chem. C* **2019**, *7*, 757.

[84] H. Dong, C. Zhang, X. Liu, J. Yao, Y. S. Zhao, *Chem. Soc. Rev.* **2020**, *49*, 951.

[85] X. Xu, W. Qian, S. Xiao, J. Wang, S. Zheng, S. Yang, *EcoMat* **2020**, *2*, e12064.

[86] Y. Zhou, J. Chen, O. M. Bakr, O. F. Mohammed, *ACS Energy Lett.* **2021**, *6*, 739.

[87] H. Kim, J. S. Han, J. Choi, S. Y. Kim, H. W. Jang, *Small Methods* **2018**, *2*, 1700310.

[88] R. Wang, M. Mujahid, Y. Duan, Z.-K. Wang, J. Xue, Y.

Yang, *Adv. Funct. Mater.* **2019**, *29*, 1808843.
[89] R. S. Sanchez, E. Mas-Marza, *Sol. Energy Mater. Sol. Cells* **2016**, *158*, 189.
[90] J. Ji, X. Liu, H. Jiang, M. Duan, B. Liu, H. Huang, D. Wei, Y. Li, M. Li, *iScience* **2020**, *23*, 101013.
[91] B. Philippe, B.-W. Park, R. Lindblad, J. Oscarsson, S. Ahmadi, E. M. J. Johansson, H. Rensmo, *Chem. Mater.* **2015**, *27*, 1720.
[92] S. Bae, S. Kim, S.-W. Lee, K. J. Cho, S. Park, S. Lee, Y. Kang, H.-S. Lee, D. Kim, *J. Phys. Chem. Lett.* **2016**, *7*, 3091.
[93] C.-X. Zhang, T. Shen, D. Guo, L.-M. Tang, K. Yang, H.-X. Deng, *InfoMat* **2020**, *2*, 1034.
[94] I. Mesquita, L. Andrade, A. Mendes, *ChemSusChem* **2019**, *12*, 2186.
[95] A. K. Jena, Y. Numata, M. Ikegami, T. Miyasaka, *J. Mater. Chem. A* **2018**, *6*, 2219.
[96] Z. H. Bakr, Q. Wali, A. Fakharuddin, L. Schmidt-Mende, T. M. Brown, R. Jose, *Nano Energy* **2017**, *34*, 271.
[97] P. Roy, N. Kumar Sinha, S. Tiwari, A. Khare, *Sol. Energy* **2020**, *198*, 665.
[98] A. G. Boldyreva, A. F. Akbulatov, M. Elnaggar, S. Y. Luchkin, A. V Danilov, I. S. Zhidkov, O. R. Yamilova, Y. S. Fedotov, S. I. Bredikhin, E. Z. Kurmaev, K. J. Stevenson, P. A. Troshin, *Sustain. Energy Fuels* **2019**, *3*, 2705.
[99] J. Wei, Q. Wang, J. Huo, F. Gao, Z. Gan, Q. Zhao, H. Li, *Adv. Energy Mater.* **2020**, *n/a*, 2002326.
[100] J. Cao, F. Yan, *Energy Environ. Sci.* **2021**, *14*, 1286.
[101] G.-W. Kim, H. Choi, M. Kim, J. Lee, S. Y. Son, T. Park, *Adv. Energy Mater.* **2020**, *10*, 1903403.
[102] A. Fakharuddin, M. Vasilopoulou, A. Soultati, M. I. Haider, J. Briscoe, V. Fotopoulos, D. Di Girolamo, D. Davazoglou, A. Chroneos, A. R. bin M. Yusoff, A. Abate, L. Schmidt-Mende, M. K. Nazeeruddin, *Sol. RRL* **2020**, *n/a*, 2000555.
[103] A. Abate, T. Leijtens, S. Pathak, J. Teuscher, R. Avolio, M. E. Errico, J. Kirkpatrik, J. M. Ball, P. Docampo, I. McPherson, H. J. Snaith, *Phys. Chem. Chem. Phys.* **2013**, *15*, 2572.
[104] E. J. Juarez-Perez, M. R. Leyden, S. Wang, L. K. Ono, Z. Hawash, Y. Qi, *Chem. Mater.* **2016**, *28*, 5702.
[105] Y. Yue, N. Salim, Y. Wu, X. Yang, A. Islam, W. Chen, J. Liu, E. Bi, F. Xie, M. Cai, L. Han, *Adv. Mater.* **2016**, *28*, 10738.

[106] S. Wang, M. Sina, P. Parikh, T. Uekert, B. Shahbazian, A. Devaraj, Y. S. Meng, *Nano Lett.* **2016**, *16*, 5594.
[107] H. D. Pham, T. C.-J. Yang, S. M. Jain, G. J. Wilson, P. Sonar, *Adv. Energy Mater.* **2020**, *10*, 1903326.
[108] H. Lu, B. He, Y. Ji, Y. Shan, C. Zhong, J. Xu, J. LiuYang, F. Wu, L. Zhu, *Chem. Eng. J.* **2020**, *385*, 123976.
[109] S. Wang, Q. Wei, K. Wang, Z. Zhang, D. Zhao, C. Liang, T. Liu, J. Guo, C. Su, Y. Li, G. Xing, *Small* **2020**, *16*, 1907513.
[110] A. Barranco, M. C. Lopez-Santos, J. Idigoras, F. J. Aparicio, J. Obrero-Perez, V. Lopez-Flores, L. Contreras-Bernal, V. Rico, J. Ferrer, J. P. Espinos, A. Borras, J. A. Anta, J. R. Sanchez-Valencia, *Adv. Energy Mater.* **2020**, *10*, 1901524.
[111] I. Hussain, H. P. Tran, J. Jaksik, J. Moore, N. Islam, M. J. Uddin, *Emergent Mater.* **2018**, *1*, 133.
[112] J. Wang, K. Liu, L. Ma, X. Zhan, *Chem. Rev.* **2016**, *116*, 14675.
[113] R. Fuentes Pineda, Y. Zems, J. Troughton, M. R. Niazi, D. F. Perepichka, T. Watson, N. Robertson, *Sustain. Energy Fuels* **2020**, *4*, 779.
[114] F. Zhang, Z. Wang, H. Zhu, N. Pellet, J. Luo, C. Yi, X. Liu, H. Liu, S. Wang, X. Li, Y. Xiao, S. M. Zakeeruddin, D. Bi, M. Grätzel, *Nano Energy* **2017**, *41*, 469.
[115] X. Liu, S. Ma, M. Mateen, P. Shi, C. Liu, Y. Ding, M. Cai, M. Guli, M. K. Nazeeruddin, S. Dai, *Sustain. Energy Fuels* **2020**, *4*, 1875.
[116] S. Valero, S. Collavini, S. F. Völker, M. Saliba, W. R. Tress, S. M. Zakeeruddin, M. Grätzel, J. L. Delgado, *Macromolecules* **2019**, *52*, 2243.
[117] S. Ahn, S.-H. Jeong, T.-H. Han, T.-W. Lee, *Adv. Opt. Mater.* **2017**, *5*, 1600512.
[118] Z. Shariatinia, *Renew. Sustain. Energy Rev.* **2020**, *119*, 109608.
[119] J. Ye, X. Li, J. Zhao, X. Mei, Q. Li, *RSC Adv.* **2016**, *6*, 36356.
[120] V. E. Madhavan, I. Zimmermann, C. Roldán-Carmona, G. Grancini, M. Buffiere, A. Belaidi, M. K. Nazeeruddin, *ACS Energy Lett.* **2016**, *1*, 1112.
[121] J. Tirado, M. Vásquez-Montoya, C. Roldán-Carmona, M. Ralaiarisoa, N. Koch, M. K. Nazeeruddin, F. Jaramillo, *ACS Appl. Energy Mater.* **2019**, *2*, 4890.
[122] X. Li, J. Yang, Q. Jiang, W. Chu, D. Zhang, Z. Zhou, J. Xin, *ACS Appl. Mater. Interfaces* **2017**, *9*, 41354.

[123] L. Chen, Q. Xie, L. Wan, W. Zhang, S. Fu, H. Zhang, X. Ling, J. Yuan, L. Miao, C. Shen, X. Li, W. Zhang, B. Zhu, H.-Q. Wang, *ACS Appl. Energy Mater.* **2019**, *2*, 5862.
[124] X. Yao, J. Qi, W. Xu, X. Jiang, X. Gong, Y. Cao, *ACS Omega* **2018**, *3*, 1117.
[125] E. Rezaee, X. Liu, Q. Hu, L. Dong, Q. Chen, J.-H. Pan, Z.-X. Xu, *Sol. RRL* **2018**, *2*, 1800200.
[126] Y. Fang, C. Bi, D. Wang, J. Huang, *ACS Energy Lett.* **2017**, *2*, 782.
[127] M. Liu, M. B. Johnston, H. J. Snaith, *Nature* **2013**, *501*, 395.
[128] H.-S. Ko, J.-W. Lee, N.-G. Park, *J. Mater. Chem. A* **2015**, *3*, 8808.
[129] Q. Chen, H. Zhou, Z. Hong, S. Luo, H.-S. Duan, H.-H. Wang, Y. Liu, G. Li, Y. Yang, *J. Am. Chem. Soc.* **2014**, *136*, 622.
[130] C. Zuo, A. D. Scully, W. L. Tan, F. Zheng, K. P. Ghiggino, D. Vak, H. Weerasinghe, C. R. McNeill, D. Angmo, A. S. R. Chesman, M. Gao, *Commun. Mater.* **2020**, *1*, 33.
[131] Y. Deng, E. Peng, Y. Shao, Z. Xiao, Q. Dong, J. Huang, *Energy Environ. Sci.* **2015**, *8*, 1544.
[132] F. Mathies, H. Eggers, B. S. Richards, G. Hernandez-Sosa, U. Lemmer, U. W. Paetzold, *ACS Appl. Energy Mater.* **2018**, *1*, 1834.
[133] Z. Li, P. Li, G. Chen, Y. Cheng, X. Pi, X. Yu, D. Yang, L. Han, Y. Zhang, Y. Song, *ACS Appl. Mater. Interfaces* **2020**, *12*, 39082.

Chapter 2. Experimental section

In this Chapter, a description of the main materials, deposition methods and characterization techniques used in this thesis are exposed.

2.1. Materials and methods

In this section, a brief description of the preparation and deposition methods of the perovskites used in the different works is presented.

2.1.1. Perovskite quantum dots

The $CsPbBr_3$ perovskite quantum dots, analysed in Chapter 3, are prepared using the hot-injection method.[1] In this method, first employed in $CsPbBr_3$ perovskites by Protesescu *et al.*[2], two different solutions are prepared separately under inert atmosphere and then one is quickly injected into the other one. After 5 seconds, the reaction is quenched to stop the growth of the nanocrystals.

The first solution is the caesium precursor solution and is prepared with 0.618g caesium carbonate (Cs_2CO_3) that are dissolved in 30mL octadecene. A small amount of oleic acid, 1.9mL, is added to form caesium oleate. The solution is heated at 120ºC during 1h under vacuum. After that, the solution is heated 30min at 140ºC under nitrogen until caesium carbonate is dissolved. The caesium oleate solution is kept at 120ºC in nitrogen until it is used.

The second solution, lead bromide ($PbBr_2$) precursor solution, is prepared dissolving 1g $PbBr_2$ in 50mL octadecene. The solution is degassed at 120ºC 1h, after that, 5mL oleic acid and 5mL oleylamine are added under nitrogen atmosphere. The solution is heated to the desired temperature, in this case 175ºC, then 4mL of caesium oleate solution is quickly injected and finally the reaction is quenched in an ice bath.

After the synthesis, the nanocrystals are isolated and purified.[3] 60mL methyl acetate are added to the solution and it is centrifuged 5min at 4700rpm. After that, the precipitate is dispersed in hexane. This solution is dried and the concentration is adjusted to 50mg/mL for the final solution of the quantum dots in toluene.

2.1.2. Perovskites in solar cells

In the perovskite solar cells, studied in Chapter 4 and 5, different regular configurations have been studied.[4,5] In the contributions presented in this thesis, the substrates are glass coated with FTO. The substrates that are not patterned are first etched with 2M HCl and zinc. Then, the substrates are cleaned with soap and sonicated in a diluted soap solution, rinsed and sonicated in IPA or ethanol, sonicated in acetone and dried. Finally, all the substrates are treated with UV-ozone before depositing the materials.

On top, a compact layer of TiO_2 is deposited by spray-pyrolysis at 450ºC. For that, a solution of titanium diisopropoxide bis(acetylacetonate) in ethanol (1:9, volume) is prepared just before the deposition. The film is annealed at 450ºC during 5min before cooling down. In some samples a TiO_2 mesoporous layer is deposited before the perovskite layer. In this case, a 30-nm TiO_2 paste diluted in ethanol (1:5, weight) is spin-coated. The film is first dried at 100ºC 10min and then annealed at 450/500ºC 30min.

The following layer on top of the TiO_2 (compact or meso) is the perovskite layer. In this case, two compositions and two different deposition methods have been studied. In the work with different HTMs, the perovskite is $MAPbI_3$ and it is deposited by spin-coating with antisolvent. The solution is prepared dissolving PbI_2 and MAI (1.35M) in DMF/DMSO (1mL/80-95μL). It is spin-coated dripping diethyl ether at around 9s. The film is annealed at 100ºC during 3min. The solution is prepared in a nitrogen-filled glovebox and the deposition is carried out in ambient air, inside a fume hood.

In the other contribution, two different methodologies are compared. The perovskite solution is 1M FAI, 1.1M PbI_2, 0.2M MABr and 0.2M $PbBr_2$ in DMF:DMSO (2:1 in volume). To prepare the triple cation perovskite, 5% CsI (1.5M in DMSO) is added to the solution. For the antisolvent samples, the solution was spin-coated and 5s before the end of the spinning, 100 μL chlorobenzene is dripped. The film is annealed 1h at 100ºC. All the process is developed inside a nitrogen-filled glovebox. In the study of FIRA samples, the solution (described above) is spin-coated and the film is irradiated with IR radiation 1.2s and is left 20s for cooling down. This process is developed in ambient air inside a fume hood.

The following layer of the device is the HTM. In both contributions a layer of spiro-OMeTAD is deposited by spin-coating. The solution is prepared by dissolving 72.3mg spiro-OMeTAD, 28.8μL *t*BP and 17.5μL Li-TFSI (520mg/mL stock solution in acetonitrile) in chlorobenzene. In the last contribution, 12μL cobalt (III) tris(bis(trifluoromethylsulfonyl)imide) (0.25M in acetonitrile) are also added. This process is carried out inside a nitrogen-filled glovebox.

The last layer is a metallic contact made of gold, which is thermally evaporated at 10^{-6} mbar.

2.2. Characterization techniques

In this section, the fundamentals of the main characterization techniques are described and the different equipment employed is specified. These techniques have been exploited to study both materials and final devices.

2.2.1. Current-Voltage curves

The current-voltage curve (J-V), also known as cyclic voltammetry when it is performed in a forward and reverse cycle, is the characterization technique mostly employed for measuring the efficiency of a solar cell. It is based on applying a voltage sweep while measuring the generated current. The main parameters that are measured are: short-circuit current density (J_{sc}), open-circuit voltage (V_{oc}), efficiency (η) and fill factor (FF). FF and efficiency are defined as:

$$FF(\%) = \frac{J_{mp} \cdot V_{mp}}{J_{sc} \cdot V_{oc}} \cdot 100$$

$$\eta(\%) = \frac{P_{out}}{P_{in}} \cdot 100 = \frac{FF \cdot J_{sc} \cdot V_{oc}}{P_{in}} \cdot 100$$

Where P_{in} is the incident power, J_{mp} and V_{mp} are respectively the current density and the voltage at the maximum power point, and P_{out} is the maximum power provided by the device.[6]

For this technique, a solar simulator is employed. It consists of a Xenon lamp with an output power (P_{in}) of 1 sun (1000 Wm^{-2}) with an Air Mass (AM) filter AM1.5G. This filter simulates the sun spectrum that arrives to a 37º tilted surface, including scattered and absorbed light by the atmosphere. These are the standard conditions employed to enable the comparison of the reported results between different laboratories all over the world.[7]

An anomalous feature present in PSCs with regular architectures is an effect called hysteresis. The hysteresis is defined as a phenomenon that implies a different behaviour of the J-V curve between the different scan directions.[8]

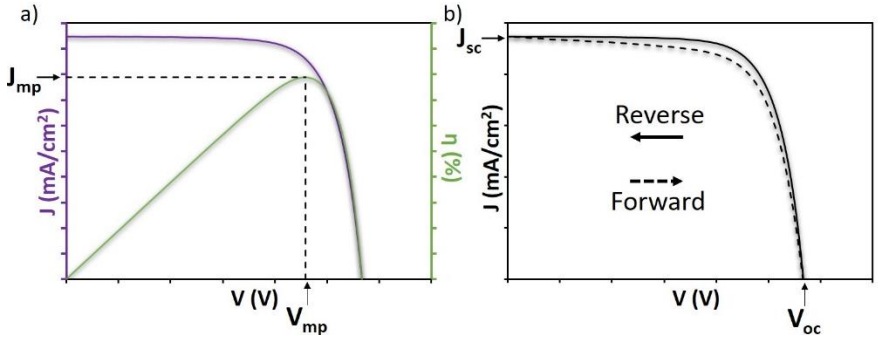

Figure 2.1. Examples of J-V curves defining some parameters: J_{sc}, V_{oc}, V_{mp}, J_{mp}, different scan directions and efficiency (η).

In Figure 2.1b, a small hysteresis is shown. However, hysteresis is strongly dependent of the sweep voltage speed.[9] In our measurements, a low scan rate is employed, usually 10 or 50 mV/s. Both forward (from 0 to V_{oc}) and reverse (from V_{oc} to 0) scan are measured.

2.2.2. X-Ray Diffraction

X-Ray Diffraction (XRD) is a technique that provides information about the crystalline structure of a material. It allows to identify the crystalline material or materials present in a powder or film. In this technique, a coherent incident beam (X-rays) interacts with the sample and the diffracted beams are detected. A crystal structure is formed by families of different crystalline planes, which are identified by Miller indices (*h k l*), and each one will generate a diffraction peak. This interaction is described in Figure 2.2 and follows Bragg's law:

$$n\,\lambda = 2\,d\,sin\theta$$

Where θ is the incident angle, d is the interplanar distance and λ is the wavelength of the beam.[10,11]

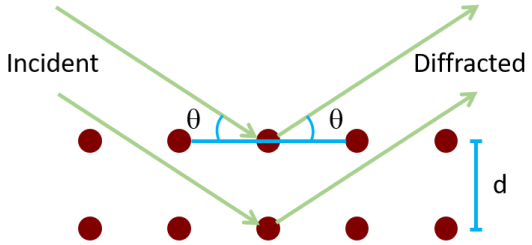

Figure 2.2. Diffraction of an incident beam of x-ray by a crystalline lattice.

Most of the crystalline materials and their different phases have a reference pattern (simulated or experimental data) with all the possible diffraction peaks and information about their intensity, diffraction angle, interplanar distance and planes. The different crystalline phases are identified by the diffraction angle, indexing the planes of the x-ray diffraction pattern.

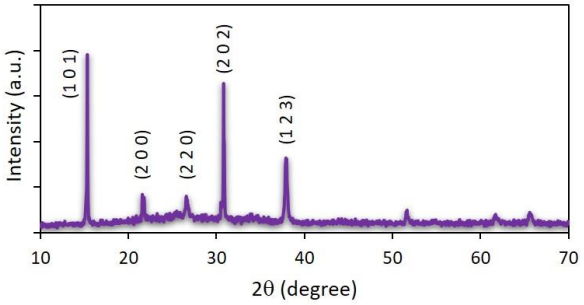

Figure 2.3. XRD pattern of $CsPbBr_3$ film. (*h k l*) indexed planes correspond to orthorhombic (Pnma) structure.[12]

2.2.3. Electron Microscopy

In this section, two techniques utilized along the thesis work are described: Scanning Electron Microscopy (SEM) and Transmission Electron Microscopy (TEM). Both techniques irradiate the sample with a high-energy electron beam and use the electron interaction with the sample to obtain information about the morphology and to characterize the chemical composition and the structure of the material, depending on the equipment.[10,11] Different electrons are generated when the electron beam interacts with the sample: primary or backscattered electrons (high energy) and secondary electrons (low energy, below 50

eV), see Figure 2.4. From the relaxation of the excited atom after interacting with the electron beam, three processes can be involved: cathodoluminescence (emission of a photon if the energy is small), X-rays (if the energy is high) or Auger electrons (an outer electron is ejected with this excess energy).[11]

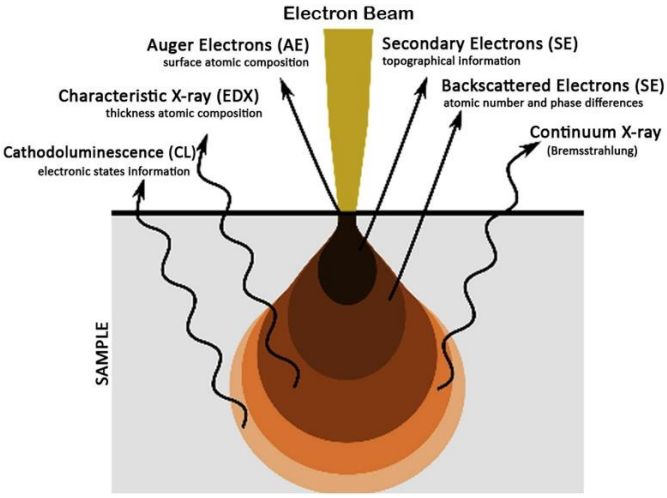

Figure 2.4. Interaction of an electron beam with the sample. The main processes involved after the incident beam arrives to the sample are shown: generated electrons (backscattered and secondary), x-ray emission (when the electrons relax), cathodoluminescence and Auger electrons. Reproduced from ref.[13] under Creative Commons license https://creativecommons.org/licenses/by-nc-nd/4.0/

2.2.3.1. Scanning Electron Microscopy

SEM is employed for obtaining an image of the surface. It generally detects secondary and backscattered electrons. Secondary electrons come from a depth of few nanometres, so they provide information about spatial surface features with more resolution. For that reason, they are more widely used for SEM images. While backscattered electrons do not enable to obtain a high spatial resolution, but they provide more information about the different composition of the material or layers.[11]

The surface must be conductive in order to avoid unwanted interactions with the electron beam by charge accumulation at the surface, so they are coated by sputtering, in this case with few nanometres of platinum.[14] Two types of measurements of prepared films were

performed: top-view and cross-section. Top-view is used to observe the quality of a film, formation of pinholes and homogeneity. And cross-section is used to evaluate the thickness of the different layers in a device.

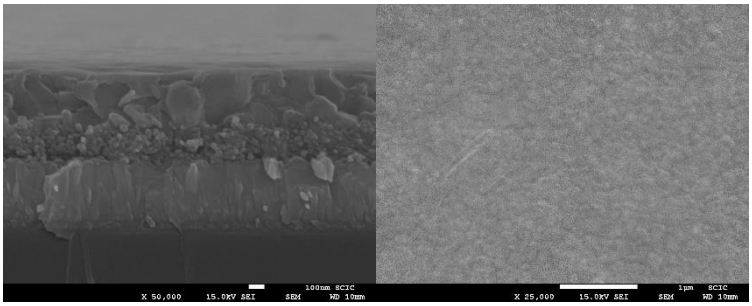

Figure 2.5. Cross-section (left) and top-view (right) of a sample. In the cross-section, different layers are observed: glass, FTO, TiO_2 (compact and mesoporous) and perovskite, from the bottom to the top. In the top-view, the morphology of perovskite layer is observed.

One measurement that could be also performed with SEM is Energy-Dispersive X-Ray (EDX) analysis. When the electron beam reaches the sample, electrons from deep energetic bands are ripped off by the electron beam and electron for shallow bands cover their places releasing the excess of energy as X-Ray radiation. This emission has a specific wavelength depending on the elements present in the sample allowing their identification. A characterization of the different elements forming the sample can be performed analysing these characteristic emissions.[11]

2.2.3.2. Transmission Electron Microscopy

TEM provides a deeper study of the material, obtaining information about the internal microstructure. In this technique, the acceleration of the electron beam is higher than in SEM, as it works at higher beam voltages.

We have used two different modes, image and electron diffraction. The former is for obtaining a magnified image. The latter is for obtaining an electron diffraction pattern that allows to recognize the crystal structure. Selected Area Diffraction (SAED) is a technique employed to obtain

the diffraction patterns of a delimited area. These diffraction patterns form rings and their radii can be related to the different interplanar crystalline distances. As commented in a previous section (2.2.2), the interplanar distances provide information about the crystal structure.[10,11,15]

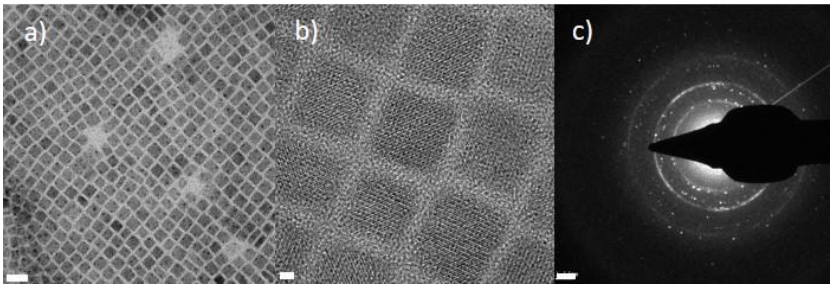

Figure 2.6. a) TEM image (scale bar 20nm), b) High Resolution TEM image (scale bar 2nm) and c) SAED pattern (scale bar 1nm^{-1}) of $CsPbBr_3$ perovskite quantum dots.

2.2.4. UV-Vis Spectroscopy

UV-Vis Spectroscopy is a technique that measures light absorption. This technique is based on Lambert-Beer law, which relates the absorbance (A) with the incident (I_0) and the transmitted intensity (I):

$$A = \log_{10} \frac{I}{I_0}$$

The sample is irradiated with different wavelengths and if the energy corresponds to an allowed transition between energy levels, incident photons can be absorbed. The UV-Vis spectrum shows the light absorption bands as function of incident wavelength.[10,14,16]

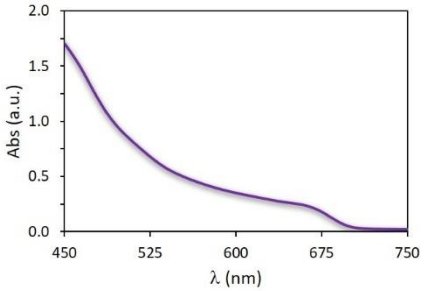

Figure 2.7. Absorption spectrum of $CsPbI_3$ perovskite quantum dots showing the absorption onset at around 700nm.

This technique provides information about the spectral region in which our material absorbs. Analysing this, its band gap can be estimated. Moreover, it is useful for determining the region where the material can be excited to characterize its emission.

2.2.5. Photoluminescence Spectroscopy

Photoluminescence (PL) spectroscopy is a technique employed to analyse the radiative recombination produced after light-induced charge excitation. It gives information about electronic transitions and the structure of the materials. When the sample is irradiated, the electrons are promoted from ground state to excited states. An electron in an excited state can release its excess energy emitting a photon, which wavelength corresponds to the difference between the initial and final state energy.[10]

Two types of photoluminescence measurements have been employed: time resolved photoluminescence (TRPL) and steady-state photoluminescence. In steady-state PL, the sample is excited with energy higher than the fundamental transition and the emission spectra is collected over a range of longer wavelengths. The photoluminescence quantum yield (PLQY) of solutions or films is an important characteristic to consider when referring to perovskites for photovoltaic applications, as depend on radiative and non-radiative recombination pathways in the sample, but also for other optoelectronic applications

like LEDs.[16] The PLQY is defined as the ratio between the absorbed and the emitted photons.[17]

In TRPL measurements, the sample is excited by a pulsed nanoLED and a single-photon detector counts the time between excitation and photon emission. The laser pulse is repeated with high frequency, usually lower than the inverse value of the sample decay time, allowing to obtain a statistic of the different decay times, so that the PL decay is obtained. In TRPL, the emission and excitation wavelengths are fixed.[18]

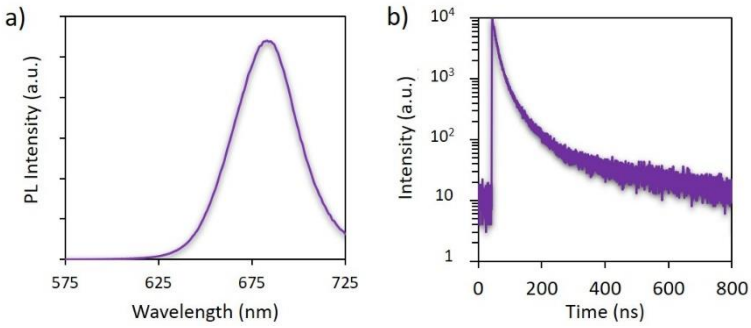

Figure 2.8. a) Photoluminescence spectrum of a $CsPbI_3$ perovskite quantum dots solution. b) Photoluminescence decay of the $CsPbI_3$ perovskite quantum dots solution. The excitation wavelength is 404nm and the signal is detected at 680nm.

2.2.6. Fourier Transform Infrared Spectroscopy

Fourier Transform Infrared Spectroscopy (FTIR) is a technique employed to identify the chemical species that are present in a sample. In our cases the species in which we are interested have been organic ligands present in the QDs surface.

In this technique, the sample is irradiated with IR radiation. The absorption of these radiation is associated with transitions between vibrational or rotational energy levels. The absorption is produced when the frequency corresponds to the frequency of the molecular vibration or rotation. In solid or liquid samples, only vibrational modes are observed.[14,19]

Each absorption band corresponds to a mode of vibration of a specific bond. For example, a strong band at around 1710cm^{-1} corresponds to C=O stretching vibration mode from a carboxylic acid.[20]

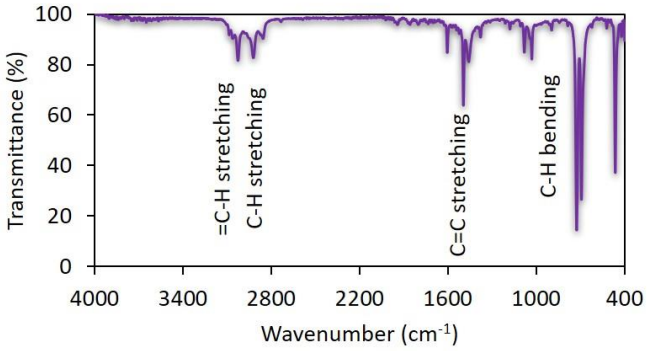

Figure 2.9. FTIR spectrum of $CsPbBr_3$ perovskite quantum dots in toluene. The different bands correspond to C-H stretching of aromatic and aliphatic groups, C=C stretching and C-H bending of the solvent.[21]

2.2.7. Impedance Spectroscopy

Impedance Spectroscopy (IS) is an electrical characterization technique in which, while applying a DC voltage, a small AC signal perturbs the sample at different frequencies. The impedance (Z) is defined as:

$$Z(\omega) = \frac{V(\omega)}{I(\omega)}$$

As V(ω) and I(ω) are sinusoidal signals depending on angular frequency (ω), it can be expressed as:

$$Z(\omega) = \frac{V_0}{I_0} e^{i\theta} = |Z(\omega)| e^{i\theta} = Z' - iZ''$$

Where V_0 is the voltage amplitude and I_0 is the current amplitude. Z' and Z'' are the real and imaginary part of the impedance respectively.

The most common representation of the results obtained is the Nyquist plot, which represents $-Z''$ as a function of Z'.[22,23]

This technique enables the characterization of different processes involved in solar cells under working conditions. If these different processes have different characteristic times (frequencies), they can be decoupled by impedance analysis, allowing their analysis separately. The results are expressed in terms of an equivalent circuit, where in an ideal situation each element is identified with one physical process.[24]

Each element has a different representation of Z, for example, in a resistor, the value is given by Ohm's law:

$$Z_R(\omega) = \frac{V(\omega)}{I(\omega)} = R$$

Where R is the resistance. It has only the real component.

Another element that is usually found in perovskite solar cells is a capacitor (C), where the relationship of the current with the voltage is:

$$I(t) = C\frac{dV(t)}{dt}$$

Where t is the time. In this case, Z results in:

$$Z_c(\omega) = \frac{1}{i\omega C}$$

Normally there are more than one element (physical process) in the device, so the total impedance is the sum of the corresponding impedance of each element.[22,23] Impedance can provide a lot of information when these elements can be linked to physical processes.

In order to have a good characterization of the solar cells, some parameters should be considered. One of the bases of IS is the linear response of the current to the small voltage perturbations and this must

be studied for each situation to ensure the linearity and a clear response (low noise level). In addition, the measurements are performed in a Faraday cage to avoid any undesired external noise.[22–24]

As IS measurements need certain measurement time, especially when low frequencies are analysed, the low stability of devices can provide non-consistent results. However, this condition is not required for comparing samples, the measure can be performed at lower light intensities, for example at 0.1 sun.

Another issue to consider when comparing different samples is the analysis at different conditions to get reliable and comparable results. Two main measurements are performed: sweeping the applied voltage at a fixed light intensity and varying the light intensity at a fixed open circuit potential (V_{oc}).[24]

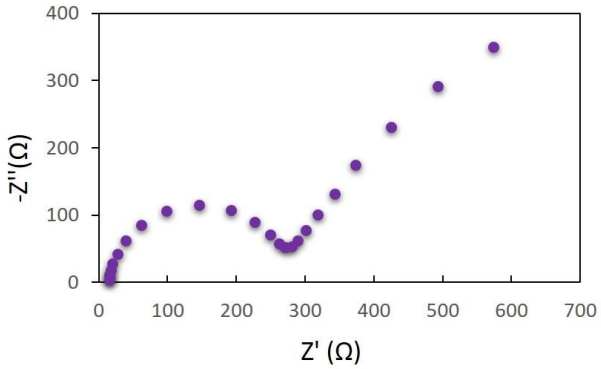

Figure 2.10. Impedance spectrum of a perovskite solar cell at 0.2V and 1sun illumination.

References

[1] M. Vallés-Pelarda, A. F. Gualdrón-Reyes, C. Felip-León, C. A. Angulo-Pachón, S. Agouram, V. Muñoz-Sanjosé, J. F. Miravet, F. Galindo, I. Mora-Seró, *Adv. Opt. Mater.* **2021**, *n/a*, 2001786.

[2] L. Protesescu, S. Yakunin, M. I. Bodnarchuk, F. Krieg, R. Caputo, C. H. Hendon, R. X. Yang, A. Walsh, M. V Kovalenko, *Nano Lett.* **2015**, *15*, 3692.

[3] E. M. Sanehira, A. R. Marshall, J. A. Christians, S. P. Harvey, P. N. Ciesielski, L. M. Wheeler, P. Schulz, L. Y. Lin, M. C. Beard, J. M. Luther, *Sci. Adv.* **2017**, *3*, eaao4204.

[4] S. F. Völker, M. Vallés-Pelarda, J. Pascual, S. Collavini, F. Ruipérez, E. Zuccatti, L. E. Hueso, R. Tena-Zaera, I. Mora-Seró, J. L. Delgado, *Chem. – A Eur. J.* **2018**, *24*, 8524.

[5] S. Sánchez, M. Vallés-Pelarda, J.-A. Alberola-Borràs, R. Vidal, J. J. Jerónimo-Rendón, M. Saliba, P. P. Boix, I. Mora-Seró, *Mater. Today* **2019**, *31*, 39.

[6] S. Rhee, K. An, K.-T. Kang, *Cryst.* **2021**, *11*, DOI: 10.3390/cryst11010039.

[7] S. Rühle, *Sol. Energy* **2016**, *130*, 139.

[8] F. Wu, R. Pathak, Q. Qiao, *Catal. Today* **2021**, DOI: https://doi.org/10.1016/j.cattod.2020.12.025.

[9] W. Tress, N. Marinova, T. Moehl, S. M. Zakeeruddin, M. K. Nazeeruddin, M. Grätzel, *Energy Environ. Sci.* **2015**, *8*, 995.

[10] A. E. Kestell, G. T. DeLorey, *Nanoparticles : Properties, Classification, Characterization, and Fabrication*, Nova Science Publishers, Incorporated, Hauppauge, UNITED STATES, **2010**.

[11] P. J. Goodhew, J. Humphreys, R. Beanland, L. E. Cartwright, F. J. Humphreys, *Electron Microscopy and Analysis*, CRC Press, London, **2000**.

[12] M. R. Linaburg, E. T. McClure, J. D. Majher, P. M. Woodward, *Chem. Mater.* **2017**, *29*, 3507.

[13] M. Ezzahmouly, A. Elmoutaouakkil, M. Ed-Dhahraouy, H. Khallok, A. Elouahli, A. Mazurier, A. ElAlbani, Z. Hatim, *Heliyon* **2019**, *5*, e02557.

[14] A. K. Shukla, S. Iravani, *Green Synthesis, Characterization and Applications of Nanoparticles*, Elsevier, San Diego, UNITED STATES, **2018**.

[15] L. Reimer, H. Kohl, *Transmission Electron Microscopy Physics of Image Formation* , Springer New York, New York, NY, **2008**.
[16] M. Pazoki, A. Hagfeldt, T. Edvinsson, *Characterization Techniques for Perovskite Solar Cell Materials*, Elsevier, San Diego, UNITED STATES, **2019**.
[17] F. Fries, S. Reineke, *Sci. Rep.* **2019**, *9*, 15638.
[18] T. Kirchartz, J. A. Márquez, M. Stolterfoht, T. Unold, *Adv. Energy Mater.* **2020**, *n/a*, 1904134.
[19] M. Tasumi, P. A. Sakamoto, S. Ochiai, *Introduction to Experimental Infrared Spectroscopy : Fundamentals and Practical Methods*, John Wiley & Sons, Incorporated, New York, UNITED KINGDOM, **2014**.
[20] J. Pan, L. N. Quan, Y. Zhao, W. Peng, B. Murali, S. P. Sarmah, M. Yuan, L. Sinatra, N. M. Alyami, J. Liu, E. Yassitepe, Z. Yang, O. Voznyy, R. Comin, M. N. Hedhili, O. F. Mohammed, Z. H. Lu, D. H. Kim, E. H. Sargent, O. M. Bakr, *Adv. Mater.* **2016**, *28*, 8718.
[21] B. H. Stuart, *Infrared Spectroscopy : Fundamentals and Applications*, John Wiley & Sons, Incorporated, Hoboken, UNITED KINGDOM, **2004**.
[22] A. Sacco, *Renew. Sustain. Energy Rev.* **2017**, *79*, 814.
[23] E. von Hauff, *J. Phys. Chem. C* **2019**, *123*, 11329.
[24] D. Pitarch-Tena, T. T. Ngo, M. Vallés-Pelarda, T. Pauporté, I. Mora-Seró, *ACS Energy Lett.* **2018**, *3*, 1044.

Chapter 3. Publication 1

3.1. High optical performance of cyan-emissive $CsPbBr_3$ perovskite quantum dots embedded in molecular organogels

Vallés-Pelarda, M., Gualdrón-Reyes, A. F., Felip-León, C., Angulo-Pachón, C. A., Agouram, S., Muñoz-Sanjosé, V., Miravet, J. F., Galindo, F., Mora-Seró, I., High Optical Performance of Cyan-Emissive CsPbBr3 Perovskite Quantum Dots Embedded in Molecular Organogels. Adv. Optical Mater. 2021, 2001786. https://doi.org/10.1002/adom.202001786.

My contribution to the work presented in this chapter has been:

- Preparation of the samples
- Optical characterization: PLQY, PL and absorption measurements
- Analysis of the FTIR and SAED patterns
- First draft preparation
- Edit part of the manuscript according to the comments of co-authors and referees

Published manuscript

High optical performance of cyan-emissive $CsPbBr_3$ perovskite quantum dots embedded in molecular organogels

Marta Vallés-Pelarda, Andrés F. Gualdrón-Reyes, Carles Felip-León, César A. Angulo-Pachón, Said Agouram, Vicente Muñoz-Sanjosé, Juan F. Miravet*, Francisco Galindo*, Iván Mora-Seró*

M. Vallés-Pelarda, Dr. A. F. Gualdrón-Reyes, Prof. I. Mora-Seró
Institute of Advanced Materials (INAM), University Jaume I. Av. de Vicent Sos Baynat, s/n 12006, Castelló de la Plana, Spain.
E-mail: sero@uji.es

Dr. C. Felip-León, Dr. C. A. Angulo-Pachón, Prof. Juan F. Miravet, Prof. Francisco Galindo
Department of Inorganic and Organic Chemistry, University Jaume I, Av. de Vicent Sos Baynat, s/n 12006, Castelló de la Plana, Spain.
E-mail: francisco.galindo@uji.es, miravet@uji.es

Dr. S. Agouram, Prof. V.Muñoz-Sanjosé
Department of Applied Physics and Electromagnetism, University of Valencia, 46100 Valencia, Spain.

Prof. I. Mora-Seró, Dr. S. Agouram, Prof. V. Muñoz-Sanjosé
Materials for Renewable Energy (MAER), Unitat Mixta d'Investigació UV-UJI

Keywords: perovskite quantum dots, organogels, blue emission, photoluminescence quantum yield

Abstract

Perovskite quantum dots (QDs) have fascinating optoelectronic properties, such as high photoluminescence quantum yield (PLQY) for a broad range of materials, and the possibility to obtain different band gaps with the same material or halide combinations. Nevertheless, blue-emissive materials generally present limited PLQY or color instability. Here, two molecular organogels, based on a derivative of an amino acid and succinic acid, were used to embed $CsPbBr_3$ quantum dots, obtaining green and blue emission. TEM and SAED measurements were performed to confirm that there were no significant changes in the average size of the QDs and the crystal structure. A high near-unity PLQY was achieved for the blue emission. This contribution opens the door to a post-synthetic treatment for synthesizing blue-emissive PQDs with high optical performance, which can be attractive for optoelectronic applications.

1. Introduction

Perovskite quantum dots (PQDs) have been widely studied due to their exceptional properties, such as high photoluminescence with narrow emission peaks and high absorption coefficient. In addition, their band gap can be easily tuned by changing their chemical composition (different halides or mixed halides) or varying the morphology of the nanoparticles (NPs).[1–4] All of these properties make them suitable for many different applications: optoelectronic devices, lasers, scintillators, sensors. [5–10] Although the emission wavelength of these NPs can be tuned from UV to near IR, the achievement of a high

photoluminescence quantum yield (PLQY) in blue emissive PQDs is still challenging. This is the case of $CsPbCl_3$ PQDs, whose PLQY is very low, the consequence of a high density of structural defects.[11] One strategy to increase the PLQY of these PQDs is by carrying out a mixture of halides (Br/Cl). However, these materials could show phase segregation and color instability.[12] Consequently, other approaches to optimize synthetic protocols for preparing PQDs with enhanced optical properties have been successfully studied.[13] In the case of $CsPbBr_3$ PQDs, the synthesis of blue-emissive nanoplatelets provides a PLQY ~70%,[1] while the preparation of sky-blue quasi-2D perovskites allows reaching a PLQY up to 88%.[10] Besides, by doping this kind of PQDs with neodymium, a PLQY up to 90% is achieved.[14] In the case of $CsPbCl_3$ PQDs, the post-treatment with $CdCl_2$ enables to obtain near-unity PLQY.[13]

Previous reports have incorporated NPs in a gel matrix, showing different effects such as an enhancement of the PL emission, a small redshift in the emission wavelength or even anion exchange reactions of PQDs that take place inside.[14–17] However, replacing the capping ligands of different NPs have shown some variations around 0.3 eV in the bandgap.[18,19] A recent work has reported a blueshift in the emission of $CsPbBr_3$ PQDs after a ligand exchange and this blueshift was explained by the reduction of particle size.[20] In addition, PQDs have been also embedded in some interesting matrices such as SiO_2,[21] poly(methylmethacrylate),[22] CaF_2 hierarchical nanospheres,[23] and so on, showing an efficient material encapsulation to improve long-term stability even in a polar ambient or moisture. However, the embedding process requires the mixture of PQDs with polar solvents in some cases,

promoting the formation of agglomerates and deteriorating their photophysical properties due to the emergence of carrier traps.[24] Thus, it is essential to provide a potential matrix where not only the stability of PQDs can be extended, but also improves their intrinsic properties.

In this work, a mixture of $CsPbBr_3$ PQDs and organogelator molecules is presented, exhibiting a modification of their optical properties, specially a blueshift in the band gap and an enhancement of the PLQY. $CsPbBr_3$ PQDs embedded in the gel matrices show different emission wavelengths, green or blue, depending on the organogelator structure. The highest PLQY, near- unity, is achieved for blue emission, keeping around 80% of the initial value after 4 months. This improvement is associated with efficient surface passivation provided by the organogelator, Hx, covering the PQDs and reducing structural defects provided mainly by the loss of capping ligands. The combination of organic gels and PQDs can be useful to improve the photophysical properties of NPs, which can increase their interest in optoelectronics.

2. Results and discussion

Molecular organogelators studied in this work are the derivatives of an amino acid and succinic acid. This type of compounds forms fibrillar structures after a heating/cooling procedure, as described in the Experimental Section and also in **Figure S1**. The difference between these is the aliphatic chain arrangement of a radical; one is a linear hexyl radical (Hx) and the other is a cyclohexyl radical (Chx) (see **Figure 1a)**.[25] This small difference has shown to have a strong influence on the PQD properties after the gel formation. Comparing these organic

molecules with the ligands surrounding the PQDs (oleic acid and oleylamine, OA and OLEA, respectively), they have similar functional groups. The gelator with the cyclohexyl moiety preserves the properties of the $CsPbBr_3$ PQDs, it emits green. However, when the chain is linear, it shows a blue emission. In **Figure 1b**, both gel matrices embedding PQDs are shown under UV light and the different behavior is observed. As mentioned before, the solutions need to be heated in order to obtain the different gels. For that reason, the effect of the temperature was first studied. A PQDs solution was heated following the procedure to form the gel and it was characterized by TEM (Figure S1). The formation of some big NPs is observed, increasing the average size by around 1 nm, which could be attributed to the Ostwald ripening process.[26,27] In addition, the effect on the PLQY was also analyzed. Although first measurements after the treatment of the NPs usually showed a decrease in the quantum yield, over the time, it was recovered almost completely.

Figure 1c shows the normalized PL spectra of the $CsPbBr_3$ PQDs colloidal solution and the PQDs embedded in both organogels. Taking as a reference the emission wavelength of the PQDs in solution at 507 nm, a small redshift of approximately 7 nm is observed for the Chx matrix (Chx-PQDs), while a blueshift of around 20 nm is observed in the Hx matrix (Hx-PQDs). The full width at half maximum (FWHM) of the PL peaks are 29 nm for the PQDs solution, 26 nm for the Hx-PQDs and 35 nm for the Chx-PQDs. As mentioned before, it has been reported the use of amino acids such as α-amino butyric acid after the synthesis of $CsPbBr_3$ PQDs, and the impact on their photophysical properties.[20] Because of the bi-functional structure of the α-amino butyric acid, it is proposed a ligand exchange process with

conventional OA and OLEA, causing better surface passivation, and thereby the enhancement in the optical performances. This fact includes a blueshift in the PL peak, indication of the surface modification with a short-capping ligand, also mediating the decrease of PQDs size. In this context, we can suggest that Hx is promoting a surface passivation of $CsPbBr_3$ PQDs, obtaining a blueshift in their optical properties. Interestingly, the opposite effect is observed for Chx, which allows to infer that the surface coverage of PQDs is hindered. In order to explain this difference, it must be recalled that Hx and Chx self-associate in a very different manner, as it was demonstrated in the past: whereas the molecular architecture of Chx enables an efficient self-assembly and packing into fibres, Hx is less prone to self-associate. This indicates that Hx molecules could be more available to participate in the passivation process than Chx molecules.[25] Diverse heating temperatures were used, analyzing their effect on the Hx-PQDs emission. In **Table S1**, a comparison of the emission wavelengths with these temperatures is shown. In addition, a sample with low concentration of the Hx was prepared to observe the behavior of the PQDs when the gel is not completely formed, see **Figure S2**. It is observed that the blueshift is also produced in these conditions, indicating the gel formation is not the determining step for this blueshift.

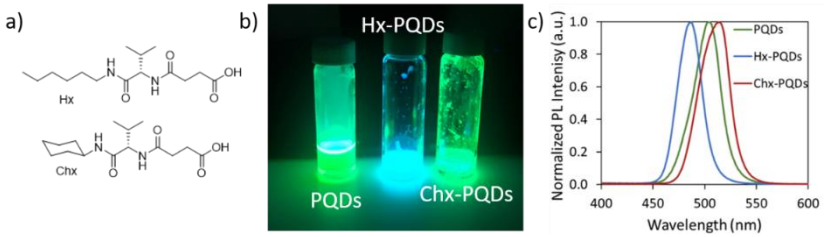

Figure 1. a) Chemical structure of the two different organogelators, Hx and Chx. b) Picture of the PQDs solution (left), Hx-PQDs (center) and Chx-PQDs (right) under UV light. c) Normalized PL spectra of the different samples: $CsPbBr_3$ PQDs solution (green), Hx matrix with $CsPbBr_3$ PQDs (blue) and Chx matrix with $CsPbBr_3$ PQDs (red).

Size, morphology and elemental composition of the Hx-PQDs and Chx-PQDs samples were analyzed by high-resolution transmission electron microscopy (HRTEM), selected area electron diffraction (SAED) and energy-dispersive X-ray spectroscopy (EDS). TEM images of PQDs colloidal solution is shown in **Figure 2a**. The chemical composition obtained from EDS measurements is shown in **Table S2**. From the TEM images in **Figure 2b-c**, an arrangement of PQDs following the fibers is observed for Hx-PQDs and Chx-PQDs samples. By estimating the particle size of the samples, we observed that the size of $CsPbBr_3$ PQDs is around 8.7 ± 2.5 nm, while Hx-PQDs show a slight decrease in the size, it is around 8.3 ± 1.9 nm. (see **Figure S3**). However, a clear difference in the particle size is seen for Chx-PQDs, around 14 ± 4 nm. The formation of smaller PQDs with a narrower size distribution in Hx-PQDs could be associated to the presence of the shorter chain ligand from the Hx. This fact induces a better uniformity and monodispersity of PQDs, which could slightly contribute to the blueshift in the PL.[20,28] Conversely, the bigger PQDs size and wider distribution obtained in presence of Chx are associated to the formation of agglomerates,

generating lower uniformity in size and causing a redshift in the PL. These effects are also observed in the absorption measurements of the different samples, as shown in **Figure S4**.

Through SAED patterns shown in **Figure 2d-f**, interplanar spacings (*d*) were measured in order to determine the crystalline phase of the PQDs before and after embedding them in Hx and Chx matrices. Attending to the *d* values obtained from SAED rings, the corresponding diffraction planes found for PQDs, Hx-PQDs and Chx-PQDs are (020), (002), (040) and (242), from the orthorhombic phase (ICSD 231019). [29–31] These results agree with HRTEM images depicted in insets of Figures 2a-c, where we can also identify some of these planes. At this point, we deduced that organic ligands do not induce changes in the crystal structure of the PQDs after the embedding process.

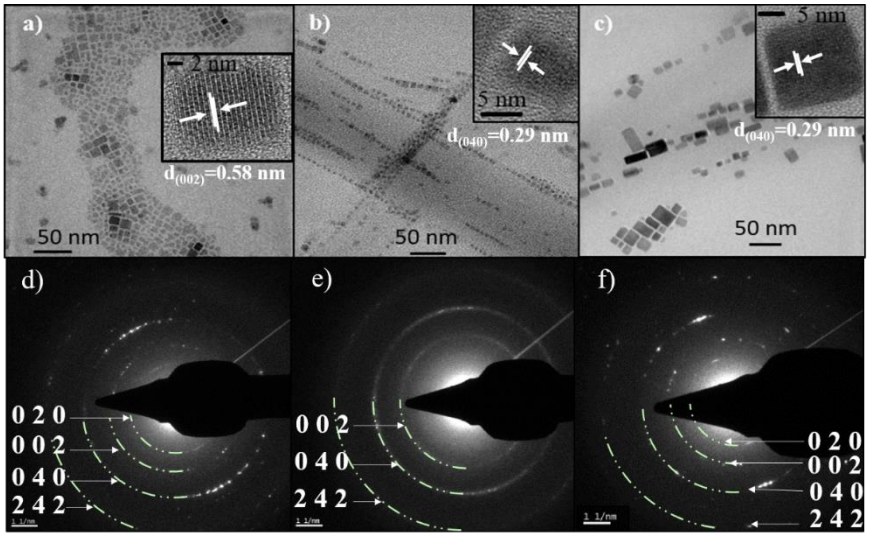

Figure 2. a) and d) TEM image and SAED patterns of the $CsPbBr_3$ PQDs solution. b) and e) TEM image and SAED patterns of the Hx-PQDs gel. c) and f) TEM image and SAED patterns of the Chx-PQDs gel. Insets in the TEM images are corresponding HRTEM images.

Fourier transformed infrared spectroscopy (FTIR) was employed to obtain information about the ligands covering the PQDs surface. In **Figure 3a**, three samples are shown: $CsPbBr_3$ PQDs solution, Hx gel and Hx-PQDs. Then, a comparison between Chx and Chx-PQDs samples is also shown in **Figure 3b**. From $CsPbBr_3$ PQDs solution, the signals in the range of 2852-2956 cm^{-1} and 1465 cm^{-1} correspond to the presence of OA and OLEA covering the PQDs surface. These bands are associated to C-H stretching and C-H bending, respectively. A broad band starting at 3300 cm^{-1} is associated to O-H stretching, while a band at 1715 cm^{-1} is ascribed to C=O stretching of the carboxylic acid.

Moreover, bands observed at 1534 and 1406 cm^{-1} are associated to the O-C-O stretching.[32,33] **Figure S5** shows the typical FTIR of OA and OLEA, where their corresponding peaks match with those of the PQDs. These results corroborate the assignment of the bands above. Then, in Hx gel spectrum, the most significant bands appear at 3283 cm^{-1} from N-H stretching, 1697 cm^{-1} from C=O (carboxylic group) and from the amides at 1632 and 1540 cm^{-1}. [9,32] In Hx-PQDs spectrum, the peaks match with the ones in the reference sample with slight variations in the position. Comparing these three samples, a decrease in the relative intensity of the assigned band at 1697 cm^{-1} in Hx-PQDs spectrum is observed, which may suggest that there is an interaction that reduces the C=O vibrational mode. However, by comparing the FTIR spectra of Chx and Chx-PQDs samples, there is no significant variation in the relative intensity of the bands.[9] At this stage, we deduce that Hx shows a high influence on the surface properties of $CsPbBr_3$ PQDs compared with Chx organic ligand, which does not seem to suffer any alteration after interacting with the perovskite colloidal solution. This observation can corroborate that Chx is more prone to self-associate due to the preorganization of its molecular structure, whereas Hx, less preorganized, is more available for the interaction at the surface of the PQDs.

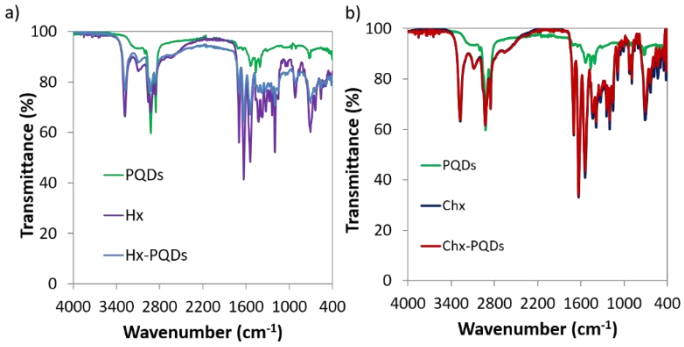

Figure 3. a) FTIR spectra of $CsPbBr_3$ PQDs in solution (green), Hx gel matrix (purple) and Hx with embedded PQDs (blue). b) FTIR spectra of $CsPbBr_3$ PQDs in solution (green), Chx gel matrix (dark blue) and Chx with embedded PQDs (red).

The stability of $CsPbBr_3$ PQDs has been also studied under ambient conditions in presence of the organogelators. By measuring the PLQY of these materials, $CsPbBr_3$ PQDs colloidal solution in absence of the matrices displays a value around 62% after one purification. By adding the gelators and forming the gel, Hx-PQDs sample shows a higher improvement of PLQY with values arriving to 95%, while Chx-QDs one was 70% (**Figure 4a**). After 6 months, Hx-PQDs and Chx-PQDs have retained the PLQY around 76% and 77% from their initial value, respectively. Simultaneously, the emission peak position of Hx-PQDs shows a slight blueshift along the time, starting at 490 nm and moving to 480 nm. Unlike the ligand exchange process, where it was described the substitution of OA and OLEA with another capping ligands,[20] we associate this phenomenon to the gradual ligand passivation provided by Hx matrix, since some OA and OLEA ligands are removed from PQDs surface after purification step. Thus, more active sites are

available for Hx to interact with the PQDs surface. Nevertheless, PL does not present any shift after some days, indicating that the ligand passivation was completed. For the case of Chx-PQDs, the emission peak position remains around 517 nm, suggesting that Chx matrix could not compensate the loss of ligands from purified PQDs. Then, by considering that the PLQY of the $CsPbBr_3$ PQDs was increased in presence of Hx, we presume that this aminoacid derivative maximizes the reduction of surface defects from PQDs, mitigating the non-radiative recombination trapping. To corroborate this hypothesis, we performed time-resolved PL (TRPL) measurements (**Figure 4c**) for the samples after 6 months, where PL parameters such as lifetime (τ_{avg}), radiative and non-radiative carrier recombination constants (k_r and k_{nr}, respectively) were estimated (**Table S3**). Although it is true that unmodified PQDs, Hx-PQDs and Chx-PQDs show similar k_r, Hx-PQDs exhibits the longest lifetime, and the lowest k_{nr} and k_{nr}/k_r. Accordingly, we deduce that Hx provides a better surface passivation than Chx matrix, hampering the non-radiative recombination mechanism and promoting the radiative channel for electron relaxation. This fact explains the PLQY improvement up to near-unity and long-term stability of Hx-PQDs. In the case of Chx-PQDs, the highest k_{nr} is a clear indication that the non-radiative recombination mechanism is facilitated, which could be associated to intraband gap energy levels formed by PQDs agglomeration.

According to the above-mentioned results, we suggest that Hx can promote a better coverage of PQDs surface due to its linear hexyl chain radical with a low grade of steric hindrance. In contrast, in the case of Chx, the cyclohexyl radical can provide a strong steric hindrance,

restraining the ligand passivation. Therefore, we concluded that Hx can be used as an efficient surface ligand passivator during the post-synthetic treatment of $CsPbBr_3$ PQDs, which increase the quality of the materials and their stability.

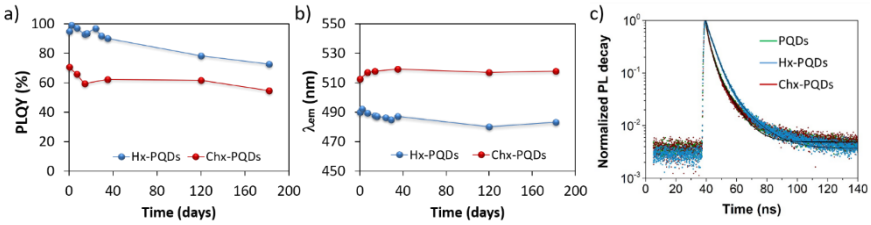

Figure 4. Evolution of a) PLQY and b) the emission wavelength of both gel matrixes: Hx (blue) and Chx (red). c) TRPL of PQDs (green), Hx-PQDs (blue) and Chx-PQDs (red) recorded 6 months after synthesis.

3. Summary and Conclusions

In this study, two different organogels with embedded $CsPbBr_3$ perovskite quantum dots, Hx-PQDs and Chx-PQDs, have been successfully prepared. The difference in the structure of these organogelators shows an effect on the PQDs, varying the emission from green to blue in the case of Hx gel. In addition to this effect, the PLQY increases, which points to an interaction between the organogels and the surface of the PQDs as shows the FTIR spectra. In the case of Hx, this short-chain amino acid derivative can slightly decrease the particle size, promoting (1) high PQDs monodispersity and blueshift of PL, and (2) efficient passivation of the PQDs

surface. This fact hinders the non-radiative carrier recombination pathway to facilitate the radiative channel. Hence, a near-unity PLQY can be achieved with a long-term stability. For Chx, the cyclohexyl radical, due to self-assembly and steric hindrance, inhibits the ligand passivation and generates a lower improvement in the photophysical features of the PQDs. Although original green emission is slightly redshifted due to PQD size increase.

Accordingly, the use of organogelators based on linear amino acids is a potential post-synthetic approach to improve the quality of PQDs. It is important to highlight that the blueshift is observed even for a low concentration of organogelators which can be widely useful for optoelectronics. Consequently, this communication points to a very interesting research line on the tunability of PQDs light emission by the use of external additives.

4. Experimental Section

Synthesis of $CsPbBr_3$ PQDs: $CsPbBr_3$ PQDs synthesis and purification were based on previously reported methods.[3,34] For the Cs-oleate solution, 0.618 g Cs_2CO_3 (Sigma-Aldrich, 99.9 %), 1.9 mL OA (Sigma Aldrich, 90 %) and 30 mL of 1-octadecene (ODE, Sigma-Aldrich, 90 %) were kept under continuous stirring under vacuum at 80 ºC and 120 °C 30 min each. Then, the solution was heated at 140 °C in nitrogen atmosphere until the Cs_2CO_3 was completely dissolved and, after that, it was kept at 120 °C.

1.0 g $PbBr_2$ (ABCR, 99.999 %) in 50 mL ODE was heated at 120 ºC under continuous stirring and kept 1 h at this temperature under vacuum. Then, under N_2, 5 mL OA and 5 mL OLEA (Sigma-Aldrich, 98 %) were added to the flask and the solution was heated to 175 °C, injecting quickly 4 mL Cs-oleate solution and after 5 s the reaction was quenched by cooling down the reaction in an ice bath.

$CsPbBr_3$ PQDs were isolated and purified by adding 60 mL of methyl acetate and centrifuging the mixture at 4700 rpm 5 min. The precipitated PQDs where dispersed in hexane (Honeywell, 99.7%). To obtain the desired concentration, the PQDs solution was dried and re-dispersed in toluene for a final concentration 50 mg mL^{-1}.

Preparation of the gels: Syntheses of Hx and Chx were based on a previous report.[25] The different gelators were weighed to obtain a 2.5 mg mL^{-1} solution in toluene for Hx and 2.0 mg mL^{-1} for Chx. To form the gel matrix, they were heated with an air gun and let it cool down. When they were completely formed, the perovskite QDs were added to obtain a final concentration of 1 mg mL^{-1} and the gels were heated and cooled again.

Characterization: PL and PLQY measurements were carried out using an absolute quantum yield spectrometer (C9920-02, Hamamatsu) with an integral sphere, fixing the absorbance values in a range around 0.3-0.6, using a Xe lamp (150 W) as light source. Samples were excited at 350 nm. Time-resolved PL measurements were performed through photoluminescence spectrophotometer (Fluorolog 3-11, Horiba) at 405 nm pulsed laser (1 MHz frequency, NanoLED-405L, <100 ps of pulse width). Transmission Electron

Microscopy (TEM) measurements were carried out in a field emission gun TECNAI G^2 F20 microscope operated at 200 kV. UV-visible absorption spectra were measured by a PerkinElmer LAMBDA 1050+ UV/Vis/NIR spectrophotometer. FTIR spectroscopy was measured using a FTIR spectrometer FT/IR-6200 (Jasco) in ATR using a diamond glass.

Supporting Information

Supporting Information is available from the Wiley Online Library or from the author.

Acknowledgements

M.V.-P. A. G.-R. and I.M.-S. acknowledge the support of the European Research Council (ERC) via Consolidator Grant (724424 - No-LIMIT) and Generalitat Valenciana via Prometeo Grant Q-Devices (Prometeo/2018/098). M. V-P. acknowledges Universitat Jaume I for the support through FPI Fellowship Program (PREDOC/2017/40). F.G. and J. F. M. acknowledge the support of Spanish Ministerio de Ciencia, Innovación y Universidades (RTI2018-101675-B-I00). S.A. and V.M.-S. acknowledge the support of the EU (FEDER) and MINECO under project TEC2017-85912-C2-2. We acknowledge SCIC from UJI for help with FTIR characterization. Authors thank Dr. Samrat Das Adhikari for his useful comments about the manuscript.

Received: ((will be filled in by the editorial staff))
Revised: ((will be filled in by the editorial staff))
Published online: ((will be filled in by the editorial staff))

References

[1] B. J. Bohn, Y. Tong, M. Gramlich, M. L. Lai, M. Döblinger, K. Wang, R. L. Z. Hoye, P. Müller-Buschbaum, S. D. Stranks, A. S. Urban, L. Polavarapu, J. Feldmann, *Nano Lett.* **2018**, *18*, 5231.

[2] Q. Van Le, K. Hong, H. W. Jang, S. Y. Kim, *Adv. Electron. Mater.* **2018**, *4*, 1800335.

[3] L. Protesescu, S. Yakunin, M. I. Bodnarchuk, F. Krieg, R. Caputo, C. H. Hendon, R. X. Yang, A. Walsh, M. V Kovalenko, *Nano Lett.* **2015**, *15*, 3692.

[4] A. Dutta, S. K. Dutta, S. Das Adhikari, N. Pradhan, *ACS Energy Lett.* **2018**, *3*, 329.

[5] S. Huang, M. Guo, J. Tan, Y. Geng, J. Wu, Y. Tang, C. Su, C. C. Lin, Y. Liang, *ACS Appl. Mater. Interfaces* **2018**, *10*, 39056.

[6] C.-Y. Huang, C. Zou, C. Mao, K. L. Corp, Y.-C. Yao, Y.-J. Lee, C. W. Schlenker, A. K. Y. Jen, L. Y. Lin, *ACS Photonics* **2017**, *4*, 2281.

[7] Y. Wang, X. Li, J. Song, L. Xiao, H. Zeng, H. Sun, *Adv. Mater.* **2015**, *27*, 7101.

[8] F. Zhou, Z. Li, W. Lan, Q. Wang, L. Ding, Z. Jin, *Small Methods* **2020**, *n/a*, 2000506.

[9] M. Fang, S. Huang, D. Li, C. Jiang, P. Tian, H. Lin, C. Luo, W. Yu, H. Peng, *Nanophotonics* **2018**, *7*, 1949.

[10] J. Xing, Y. Zhao, M. Askerka, L. N. Quan, X. Gong, W. Zhao, J. Zhao, H. Tan, G. Long, L. Gao, Z. Yang, O. Voznyy, J. Tang, Z.-H. Lu, Q. Xiong, E. H. Sargent, *Nat. Commun.* **2018**, *9*, 3541.

[11] N. Mondal, A. De, A. Samanta, *ACS Energy Lett.* **2019**, *4*, 32.

[12] N. K. Kumawat, X.-K. Liu, D. Kabra, F. Gao, *Nanoscale* **2019**,

11, 2109.

[13] A. Dutta, R. K. Behera, P. Pal, S. Baitalik, N. Pradhan, *Angew. Chemie Int. Ed.* **2019**, *58*, 5552.

[14] P. D. Wadhavane, R. E. Galian, M. A. Izquierdo, J. Aguilera-Sigalat, F. Galindo, L. Schmidt, M. I. Burguete, J. Pérez-Prieto, S. V Luis, *J. Am. Chem. Soc.* **2012**, *134*, 20554.

[15] W. J. Peveler, J. C. Bear, P. Southern, I. P. Parkin, *Chem. Commun.* **2014**, *50*, 14418.

[16] J.-M. Park, J. Park, Y.-H. Kim, H. Zhou, Y. Lee, S. H. Jo, J. Ma, T.-W. Lee, J.-Y. Sun, *Nat. Commun.* **2020**, *11*, 4638.

[17] M. Yamauchi, Y. Fujiwara, S. Masuo, *ACS Omega* **2020**, *5*, 14370.

[18] R. Nadler, J. F. Sanz, *J. Phys. Chem. A* **2015**, *119*, 1218.

[19] J. Amaya Suárez, J. J. Plata, A. M. Márquez, J. Fernández Sanz, *J. Phys. Chem. A* **2017**, *121*, 7290.

[20] S. R, H. V Vishaka, K. J, R. G. Balakrishna, *ACS Appl. Nano Mater.* **2020**, *3*, 6089.

[21] C. Sun, Y. Zhang, C. Ruan, C. Yin, X. Wang, Y. Wang, W. W. Yu, *Adv. Mater.* **2016**, *28*, 10088.

[22] Y. Cai, Y. Li, L. Wang, R.-J. Xie, *Adv. Opt. Mater.* **2019**, *7*, 1901075.

[23] Y. Wei, H. Xiao, Z. Xie, S. Liang, S. Liang, X. Cai, S. Huang, A. A. Al Kheraif, H. S. Jang, Z. Cheng, J. Lin, *Adv. Opt. Mater.* **2018**, *6*, 1701343.

[24] D. H. Park, J. S. Han, W. Kim, H. S. Jang, *Dye. Pigment.* **2018**, *149*, 246.

[25] C. A. Angulo-Pachón, C. Gascó-Catalán, J. J. Ojeda-Flores, J. F. Miravet, *ChemPhysChem* **2016**, *17*, 2008.

[26] J. B. Hoffman, G. Zaiats, I. Wappes, P. V Kamat, *Chem. Mater.* **2017**, *29*, 9767.

[27] Y. De Smet, L. Deriemaeker, R. Finsy, *Langmuir* **1997**, *13*, 6884.

[28] F. Bertolotti, G. Nedelcu, A. Vivani, A. Cervellino, N. Masciocchi, A. Guagliardi, M. V Kovalenko, *ACS Nano* **2019**, *13*, 14294.

[29] P. Cottingham, R. L. Brutchey, *Chem. Commun.* **2016**, *52*, 5246.

[30] M. C. Brennan, M. Kuno, S. Rouvimov, *Inorg. Chem.* **2019**, *58*, 1555.

[31] P. Cottingham, R. L. Brutchey, *Chem. Mater.* **2018**, *30*, 6711.

[32] J. Pan, L. N. Quan, Y. Zhao, W. Peng, B. Murali, S. P. Sarmah, M. Yuan, L. Sinatra, N. M. Alyami, J. Liu, E. Yassitepe, Z. Yang, O. Voznyy, R. Comin, M. N. Hedhili, O. F. Mohammed, Z. H. Lu, D. H. Kim, E. H. Sargent, O. M. Bakr, *Adv. Mater.* **2016**, *28*, 8718.

[33] L. C. Cass, M. Malicki, E. A. Weiss, *Anal. Chem.* **2013**, *85*, 6974.

[34] A. Swarnkar, A. R. Marshall, E. M. Sanehira, B. D. Chernomordik, D. T. Moore, J. A. Christians, T. Chakrabarti, J. M. Luther, *Science (80-.).* **2016**, *354*, 92 LP.

[35] V. K. Ravi, R. A. Scheidt, A. Nag, M. Kuno, P. V Kamat, *ACS Energy Lett.* **2018**, *3*, 1049.

Marta Vallés-Pelarda, Andrés F. Gualdrón-Reyes, Carles Felip-León, César A. Angulo-Pachón, Said Agouram, Vicente Muñoz-Sanjosé, Juan F. Miravet*, Francisco Galindo*, Iván Mora-Seró*

High optical performance of cyan-emissive $CsPbBr_3$ perovskite quantum dots embedded in molecular organogels

ToC figure

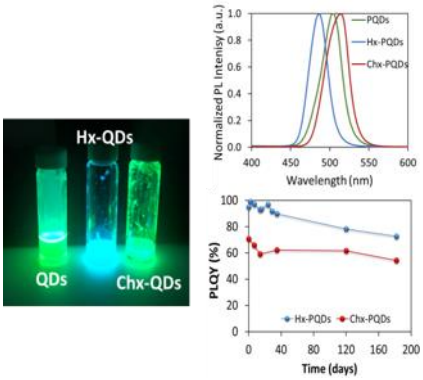

$CsPbBr_3$ perovskite quantum dots are embedded in two different organogels, Hx and Chx. Both short-chain capping ligands improve the photophysical properties of PQDs, being more significative by using the hexyl-radical aminoacid derivative. In this case, near-unity PLQY with blue emission and long-term stability is achieved, considering this post-synthetic treatment attractive for enhancing the quality of blue-emissive PQDs.

Supporting Information

High optical performance of cyan-emissive $CsPbBr_3$ perovskite quantum dots embedded in molecular organogels

Marta Vallés-Pelarda, Andrés F. Gualdrón-Reyes, Carles Felip-León, César A. Angulo-Pachón, Said Agouram, Vicente Muñoz-Sanjosé, Juan F. Miravet, Francisco Galindo*, Iván Mora-Seró**

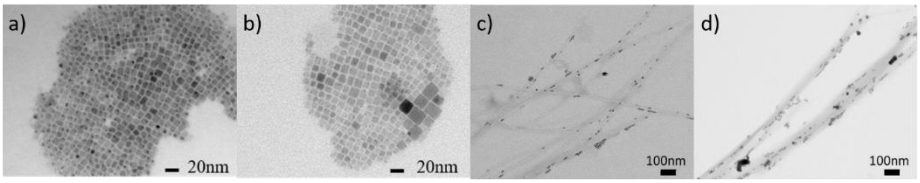

Figure S1. TEM images of PQDs solution a) as prepared and b) heated. c) and d) TEM images of Hx-PQDs and Chx-PQDs, respectively.

Table S1. Characterization of Hx-PQDs samples prepared at different temperatures.

Conditions	λ (nm)	PLQY (%)
PQD solution	516	49
200ºC	466	75
220ºC	471	77
240ºC	471	71

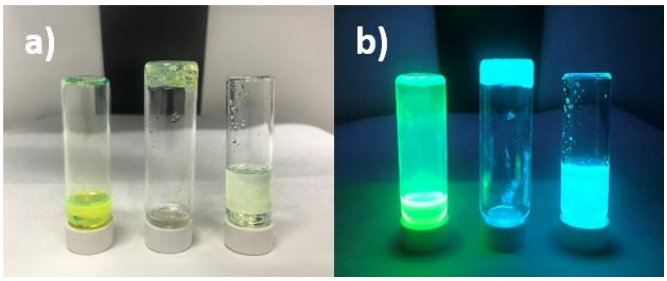

Figure S2. Picture of $CsPbBr_3$ PQDs solution (left), Hx-PQDs (gel, middle) and Hx-PQDs (low concentration, right) under a) ambient light and b) UV lamp.

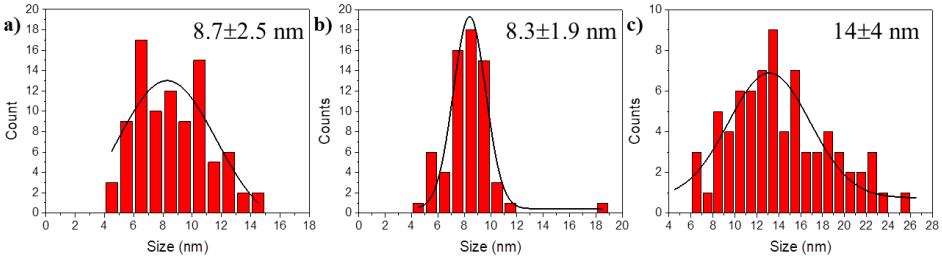

Figure S3. a), b) and c) Size distribution histograms of $CsPbBr_3$ PQDs solution, PQDs embedded in Hx and Chx, respectively.

Table S2. Energy Dispersive X-Ray analysis. Atomic %

	Cs (%)	Pb(%)	Br(%)
$CsPbBr_3$ PQDs	36.3±2.3	27±3	37±5
Hx + $CsPbBr_3$ PQDs	32.6±1.1	25.7±2.4	41.7±1.8
Chx + $CsPbBr_3$ PQDs	30±3	23.6±0.7	47±3

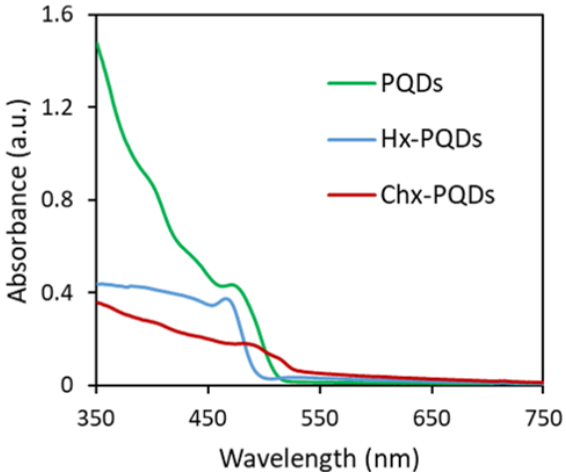

Figure S4. Absorption spectra of the PQDs, Hx-PQDs and Chx-PQDs.

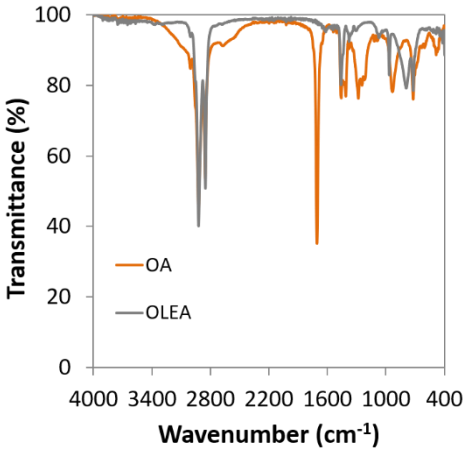

Figure S5. FTIR spectra of oleic acid and oleylamine capping ligands used for conventional $CsPbBr_3$ PQDs synthesis.

Table S3. Determination of radiative and non-radiative recombination decay rate constants, k_r and k_{nr}, respectively by fitting the time-resolved PL decays of $CsPbBr_3$ PQDs, Hx-PQDs and Chx-PQDs (Figure 4c) to a bi-exponential function: $y = y_0 + A_1 e^{-x/\tau 1} + A_2 e^{-x/\tau 2}$. The values of τ_{avg}, k_r and k_{nr} are obtained from their respective definitions: $\tau avg = (\Sigma Aj\tau j^2/\Sigma Aj\tau j)$,[1] $\tau_{avg} = 1/(k_r + k_{nr})$ and $k_r = (PLQY/\tau_{avg})$. PLQY values were used in the 0-1 range.

Samples	A_1 (%)	τ_1 (ns)	A_2 (%)	τ_2 (ns)	PLQY	τ_{avg} (ns)	k_r (10^8 s^{-1})	k_{nr} (10^7 s^{-1})	k_{nr}/k_r
$CsPbBr_3$ PQDs	58.5	2.3	41.5	9.2	0.650	5.2	1.26	6.77	0.54
Hx-PQDs	76.3	4.3	23.7	1.3	0.725	6.4	1.14	4.32	0.38
Chx-PQDs	60.7	2.2	39.3	9.1	0.544	5.0	1.10	9.21	0.84

References

[1] V. K. Ravi, R. A. Scheidt, A. Nag, M. Kuno, P. V Kamat, *ACS Energy Lett.* **2018**, *3*, 1049.

Chapter 4. Publication 2

4.1. Fullerene-Based Materials as Hole-Transporting/Electron Blocking Layers. Applications in Perovskite Solar Cells

S. F. Völker, M. Vallés-Pelarda, J. Pascual, S. Collavini, F. Ruipérez, E. Zuccatti, L. E. Hueso, R. Tena-Zaera, I. Mora-Seró, J. L. Delgado, Chem. Eur. J. 2018, 24, 8524. https://doi.org/10.1002/chem.201801069

My contribution to the work presented in this chapter has been:

- Preparation of all the devices with TiO_2 as ETM.
- Characterization of solar cells with TiO_2 as ETM: *J-V* curves, Impedance Spectroscopy, PL, SEM and TRPL measurements.

Published manuscript

Fullerene-Based Materials as Hole-Transporting/Electron Blocking Layers. Applications in Perovskite Solar Cells

Sebastian F. Völker,[a]+ Marta Vallés-Pelarda,[b]+ Jorge Pascual,[c] Silvia Collavini,[a] Fernando Ruiperez,[a] Elisabetta Zuccatti,[d] Luis Hueso,[d,e] Ramón Tena-Zaera,*[c] Iván Mora-Seró,*[b] and Juan Luis Delgado*[a,e]

Dedicated to Prof. Dr. Christoph Lambert on the occasion of his 50th birthday

[a] Dr. S. F. Völker, S. Collavini, Prof. J. L. Delgado
POLYMAT, University of the Basque Country UPV/EHU.
Avenida de Tolosa 72, 20018 Donostia-San Sebastián, Spain.
E-mail: juanluis.delgado@polymat.eu

[b] M. Vallés-Pelarda, Dr. I. Mora-Seró
Institute of Advanced Materials (INAM), University of Jaume I.
Av. de Vicent Sos Baynat, s/n 12006, Castelló de la Plana, Spain.
E-mail: sero@fca.uji.es

[c] J. Pascual, Dr. R. Tena-Zaera
Materials Division, IK4-CIDETEC
Parque Tecnológico de San Sebastián, Paseo Miramón, 196,
Donostia – San Sebastián 20009, Spain.
E-mail: rtena@cidetec.es

[d] E. Zuccatti, Prof. L. Hueso
CIC nanoGUNE Consolider, 20018 Donostia – San Sebastián, Spain

[e] Prof. L. Hueso, Prof. J. L. Delgado
Ikerbasque, Basque Foundation for Science, 48011 Bilbao, Spain.

+ Both authors have contributed equally to this work.

Supporting information for this article is given via a link at the end of the document.

Abstract: Here we report for the first time an efficient fullerene-based compound, **FU7**, able to act as Hole Transporting Material (HTM) and electron blocking contact. It has been applied on perovskite solar cells (PSCs), obtaining 0.81 times the efficiency of PSCs with the standard HTM, spiro-OMeTAD, with the additional advantage that this performance is reached without any additive introduced in the HTM layer. Moreover, as a proof of concept, we have described for the first time efficient PSCs where both selective contacts are fullerene derivatives, to obtain unprecedented "fullerene sandwich" PSCs.

Since the discovery of fullerene, this molecule and the myriad of its synthesized derivatives have played a key role in the development of organic electronics.[1] Fullerenes or fullerene monoadducts, such as the well-known [6,6]-phenyl C_{61} butyric acid methyl ester (PCBM), display a suitable LUMO level (–4.03 eV) [2a] to act as good electron-transporting material (ETM), for example in the ideal working principle scheme of organic or perovskite solar cells.[3] Moreover, their soft processing conditions (low temperature, solution-processed), thermal stability and ability to transport charge allow their integration in low cost optoelectronic devices. For all these reasons it is generally established that fullerenes are outstanding electron transporters and excellent hole blockers. However, the use of a suitable chemical design combined with the intrinsic chemical versatility of fullerenes can prove that this general assumption could be revisited as we show in this work. [60]fullerene hexakis adducts have been employed recently as scaffolds to prepare liquid crystalline materials, non-viral gene delivery systems and bioactive glycoclusters. [4] However, to the best of our knowledge, [60]fullerene hexakis adducts remain unexplored in the field of solar cells, being the present study the first successful incorporation of these materials on efficient PSCs.

The addition of six organic addends to the fullerene cage to afford [60]fullerene hexakis adducts induces dramatic changes in their LUMO energy level.[5] Indeed, [60]fullerene hexakis adducts present a very different LUMO energy value (up to one volt) compared with fullerene monoadducts. Considering all these points, in the present paper we have prepared a novel [60]fullerene hexakis adduct **FU7**, suitably

functionalized with twelve "*super-triarylamine*" fragments, in order to warrant the hole-transporting ability of this new material (Figure 1). **FU7** was obtained by 12-fold Cu-catalyzed alkine-azide "click" reaction between the pre-constructed C_{60} building block[4e] bearing 12 azide groups and "*super-triarylamine*" **TAA14** (Scheme S3). The chemical identity of **FU7** was unambiguously confirmed by several spectroscopic techniques (Methods section and Figures S1-S21).

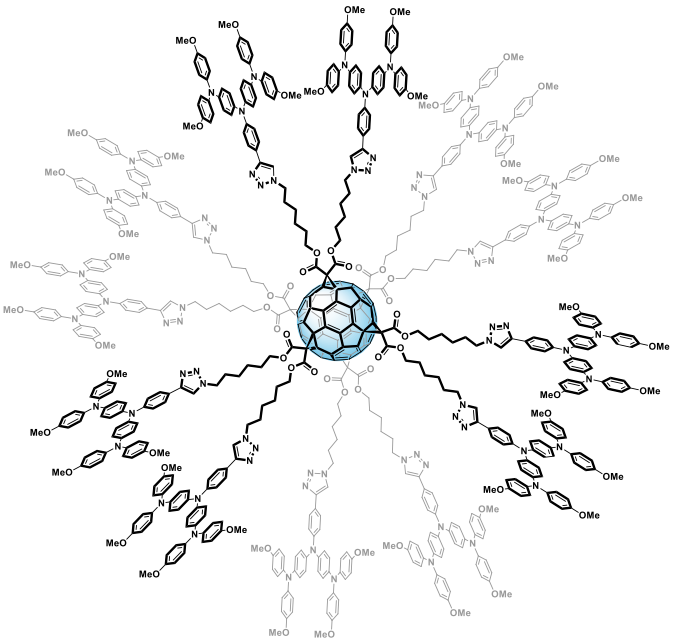

Figure 1. Chemical structure of novel [60]fullerene hexakis adduct **FU7**.

The electronic properties of **FU7** were investigated by means of cyclic voltammetry (Figure S22) and differential pulse voltammetry in methylene chloride (Figure S23), allowing to estimate a HOMO value of –5.04 eV and a LUMO value of –3.50 eV. This fact represents a significant reduction of electron affinity in respect to the well-established fullerene-based ETM LUMO level (e.g., –4.03 for PCBM, Figure S22). [2a] Density functional theory (DFT) calculations carried out with Gaussian 096[6] indicated that the HOMO is located on the super-triarylamine hole-transporting fragments and the LUMO is located on the fullerene cage (Figure S31). Furthermore, the study of

non-optimized OFET devices constituted of Si/SiO_2(150nm)/HMDS/Ti(5nm)/Au(35nm)/**FU7** allowed to confirm that **FU7** is a p-type semiconductor, which displays lower hole mobility than reference spiro-OMeTAD (Figure S32-S33). The LUMO level of **FU 7** (-3,5 eV), is comparable to other HTMs which have been described as efficient electron blocking materials.[2b-d]

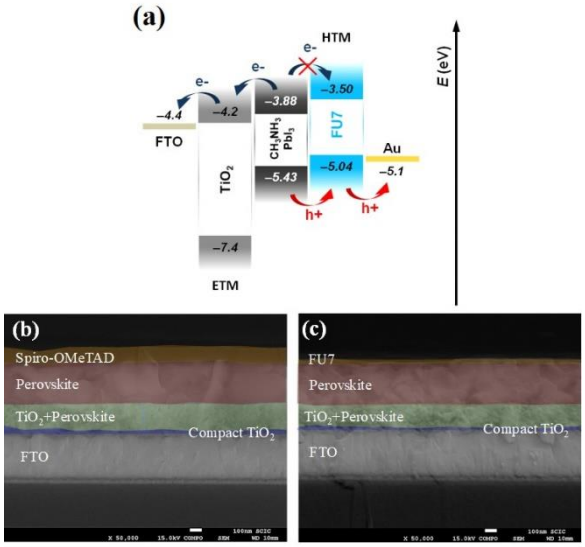

Figure 2. (a) Ideal working principle scheme of PSCs. (b) and (c) respectively cross section of PSC using spiro-OMeTAD and **FU7** as HTM, with compact TiO_2 as electron selective contact and mesoporous TiO_2 scaffold. Scale bar indicates 100 nm.

Thus, considering the ideal working principle scheme of PSCs (Figure 2a), the energy levels estimated by electrochemistry and DFT (Figures S22, S23 and S31), as well as p-type character of **FU7** confirmed by OFET measurements, this novel fullerene-based material is an ideal candidate to behave as an electron-blocking/hole-transporting material in PSCs.[7] It is important to remark that, with the addition of six organic "supertriarylamine" fragments, we are able to modulate the HOMO and LUMO of **FU7** in a single step. Thus, the LUMO of **FU7** (–3.50 eV) is almost 0,40 eV more positive than the LUMO of perovskite (Figure 2a), therefore this fullerene material is able to efficiently block electrons and suitable to behave as efficient hole-selective layer. Taking into account the ideal working principle of perovskite solar cells, illustrated on

Figure 2a, the LUMO value of PCBM (-4,02 eV) would not be suitable to block electrons, being this layer not selective to the transport of holes.

Fullerenes have been extensively proposed in the field of organic solar cells (OSCs),[8] and more recently in PSCs, showing excellent photovoltaic behavior and improving PSCs stability.[9] In particular, they have been mainly used as ETMs, [3a] but also as additives in the perovskite layer.[10,11] The use of fullerene and fullerene-based molecules in PSCs have helped reducing hysteresis,[12,13] contributed to efficiency enhancement[11] and increased long-term stability.[10,14] These benign effects have been reached by passivating the interfaces of PSCs and grain boundaries of perovskite and by acting as excellent hole-blocking ETL. In the case of **FU7**, due to the above-mentioned properties, a new role can be envisaged for the first time by a fullerene-based derivative.

To corroborate this hypothesis, PSCs were prepared using **FU7** as HTM and compared to standard reference (Ref) cells using spiro-OMeTAD (Figure 3a), which has been the first HTM employed in all-solid PSCs[15,16] and the current most extensively used HTM. PSCs have been prepared using glass, coated with fluorine-doped SnO_2 (FTO) as transparent conductive contact. A compact layer of TiO_2 deposited by spray pyrolysis, with ~50 nm thickness, has been used as electron selective contact, with a mesoporous layer, ~200 nm, deposited on top. After the $CH_3NH_3PbI_3$ perovskite deposition in air conditions[17] a capping layer of perovskites of ~300 nm was formed on top of mesoporous layer (Figure 2b and 2c). As HTM, both spiro-OMeTAD and **FU7** have been used. Ref cells present efficiencies in the average of the reported ones in the literature considering that $CH_3NH_3PbI_3$ is used as active layer (Table S2). The optimum conditions of concentration for the deposition of **FU7** dissolved in chlorobenzene have been evaluated (Table S1 and Figure S24), observing that the highest efficiencies were obtained with concentrations of 8-9 mg ml^{-1}. Such concentrations produce a layer of **FU7** with ~40 nm thickness (Figure 2c), sensibly smaller than the standard ~200 nm spiro-OMeTAD layer (Figure 2b). Higher concentrations produced thicker films, increasing the hole transport resistance at the HTM as it has been

analyzed by Impedance Spectroscopy (IS) (Figure S25).[18] A reduction of concentration produced too thin layers with pinholes.

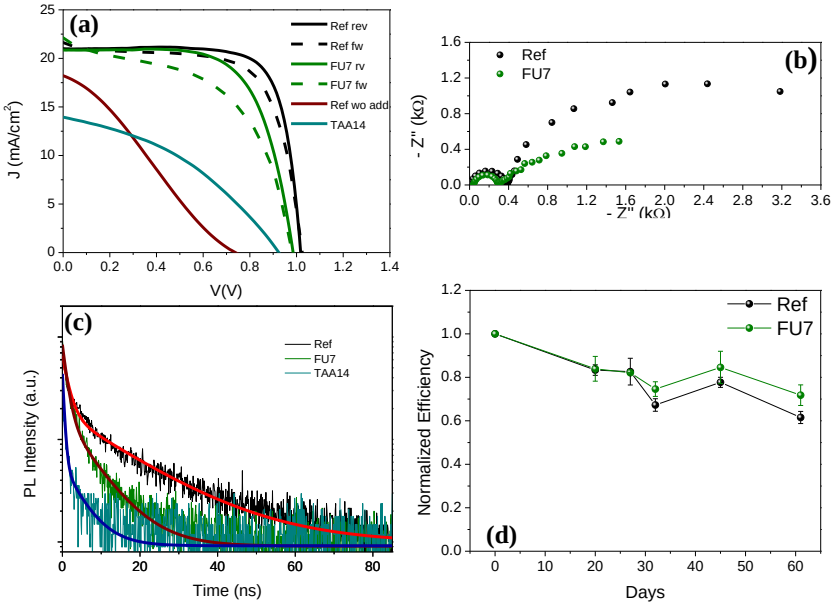

Figure 3. (a) Current-potential (J-V) curves without any preconditioning of champion reference (Ref) cell (using spiro-OMeTAD with additives as HTM) and a cell with **FU7** additive-free as HTM. Curves at forward (fw) and reverse (rv) scans are plotted. For comparison, fw scan of a solar cell prepared with spiro-OMeTAD but without any additive and a cell using the **TAA14** functional groups as HTM are included. (b) Nyquist plot of Ref and **FU7** cell under 1 sun illumination at 0.6 V DC forward applied bias. (c) The time-resolved photoluminescence (TRPL) response acquired using time-correlated single-photon counting (TCSPC) technique, 456 nm has been used as excitation wavelength and signal has been detected at 770 nm, maximum of the PL detected for the perovskite layer. The decays have been fitted with double exponential functions, which are plotted as solid lines. (d) Normalized efficiency obtained from the average of three cells at each condition (using spiro-OMeTAD and **FU7** as HTM), cells without any encapsulation were stored under dark in dry air atmosphere.

The maximum efficiency obtained for a PSC with the architecture plotted in Figure 1c has been 13.7% using a concentration of 9 mg ml^{-1} of **FU7** (Table S2). With this concentration, the perovskite layer is coated as a uniform and smooth layer with no pinholes covering the perovskite film (Figure S26). We have verified that the stabilized efficiencies are very close to the efficiencies obtained with the *J-V*

curve from the reverse scan (Figure S27). Champion device prepared with spiro-OMeTAD at the same conditions reports a photoconversion efficiency of 16.9%. *J-V* curves for champion cells prepared with **FU7** and spiro-OMeTAD are depicted in Figure 3a. It is important to highlight, that spiro-OMeTAD needs additives to work properly as HTM, concretely 4-tert-butylpyridine (TBP) and lithium bis(trifluoromethane) sulfonimidate (LiTFSI) have been used as additives, for spiro-OMeTAD preparation. Without these additives, the performance of the devices prepared with spiro-OMeTAD as HTM decreases dramatically (Figure 3a, Table S2). However, no additive was employed for the preparation of solar cells employing **FU7** as HTM. [19] The use of additives to increase the conductivity of HTM has some important drawbacks, being the reduction of long-term stability the most important one.[20,21] In this sense, a great effort has been carried out to develop additive-free HTMs. Despite this effort, no additive-free system has surpassed the performance obtained with reference cells with doped spiro-OMeTAD. The highest efficiency reported for an additive-free HTM has been obtained with a molecularly engineered star-shaped D–π–A molecule incorporating a rigid quinolizino acridine. [20] To this extent, the efficiency obtained with **FU7** is especially significant, since this derivative is the first fullerene-based material able to act as hole selective layer, with an average efficiency of 0.77±0.05 times (0.81 times for champion cells) the efficiency of reference cells, comparing more than 70 cells of each kind.

In order to understand the different performance of **FU7** in comparison to reference cell, electrical (impedance spectroscopy (IS)) and optical (Time resolved photoluminescence (TRPL)) characterization have been carried out. A representative Nyquist plot for both HTM is depicted in Figure 3b. It can be clearly appreciated that the low frequency arc is bigger for the reference sample. This arc is associated with the recombination resistance,[18,22,23] being inversely proportional to the recombination rate. Consequently, IS points to a higher recombination reducing the photovoltage in the cell containing **FU7** instead of spiro-OMeTAD, in good agreement with the experimental data (Figure 3a). This point is confirmed by TRPL measurements (Figure 3c). The pattern obtained with TRPL has been fitted using a biexponential decay

as it has been previously reported in the literature. [24-26] The value of the obtained characteristic times is depicted in Table S3. A faster decay of PL is observed when **FU7** is deposited on top of the perovskite layer. Two characteristic times τ_1 and τ_2 have been obtained from the fitting. The fastest one, τ_1, is associated with the charge carrier injection into HTM, whereas the slowest one, τ_2, is associated with recombination.[24-26] Deposition of **FU7** layer on top of perovskite reduces τ_1 significantly indicating an efficient hole transfer. However, recombination is also faster as it can be deduced by the decrease of τ_2. This analysis points to the direction that fullerene-based HTMs have to reduce interfacial recombination[27] in the future so as to improve the performance here reported.

Another important aspect that needs further analysis is the real work of fullerenes in the hole-transporting properties of **FU7**. From Figure S31 it can be clearly recognized that holes at HOMO are localized in the super-triarylamine (TAA) moieties covalently connected to the fullerene. The TAA fragment is by itself susceptible of being employed as HTM because it presents an efficient hole-scavenging effect as it has been characterized by the low τ_1 measured by TRPL (Figure 3c and Table S3). **TAA14** is the chemical precursor of **FU7** which does not contain fullerene on its chemical structure (Scheme S3) thus, devices with pinhole-free **TAA14** films (Figure S27) as HTM have been prepared. However, the performance obtained with **TAA14** is significantly lower than the observed with **FU7** as HTM (Table S2 and Figure 3a). Two different aspects could contribute to the higher performance of **FU7** in comparison with **TAA14**. On the one hand, a higher recombination for **TAA14** HTM, comparing τ_2 values in Table S3. On the other hand, the presence of fullerenes provides **FU7** with a perfect spherical shape (Figure 1), allowing a good connection of HOMO among molecules and a good separation of LUMO, centered on fullerene (Figure S31). In addition, spherical shape permits the deposition of more ordered layers. It has been observed that PCBM layers with higher structural order present a lower energy disorder and a higher Fermi level splitting, producing as a result devices with higher photovoltages.[9,28]This fact points out a key role developed by fullerene

in fullerene-based HTM producing charge separation, easy transport pathway and structural order.

Finally, the potential of additive-free fullerene-based HTM has been analyzed in order to enhance the PSC stability. The hydrophobic character of fullerenes has contributed to increase long-term stability of PSCs[10,14]. The average efficiency of samples without any encapsulation stored in dry air conditions and under dark is plotted in Figure 3d. Three cells of each type, with spiro-OMeTAD and **FU7** as HTMs, have been measured during two months and the results averaged in Figure 3d. During the first month the samples reduced in average their efficiency to 0.85 times the initial value for both reference and **FU7** samples. However, during the second month the efficiency of reference samples was reduced to 0.61 times the original value while the efficiency of **FU7** samples was reduced in a less significant amount to 0.72 times the initial value. This decrease in performance is due to a different evolution of the cell parameters photocurrent (J_{sc}), photovoltage (V_{oc}) and fill factor (FF) (Figure S29). V_{oc} was kept constant for reference cells during the two months of the experiment while for **FU7** samples photovoltage increased to 1.05 times the initial value and then kept constant (Figure S29a). The decrease in FF was higher for reference samples than for **FU7** cells (Figure S29b). Additionally, J_{sc} of **FU7** samples is reduced to 0.81 times the original value after ten days but this value did not further decrease during the rest of the experiment. However, the decrease in photocurrent registered for reference cells is more progressive, but attains the same level that the one of **FU7** cells after two months. This analysis indicates that, as fullerene-based ETMs, fullerene-based HTMs have also the potential of increasing PSC stability, especially if the initial decrease on J_{sc} can be controlled.

Moreover, as a proof-of-concept we have developed for the first time a PSC where both selective contacts are fullerene-based systems and the active layer itself also contains fullerenes (Figure 4a and Method section for further details about preparation). In this fullerene sandwich-perovskite device C_{60} and **FU7** were used as ETM and HTM, respectively. In addition, C_{60} has been used as additive in the perovskite layer processing to avoid C_{60} film degradation during the solar cell

fabrication.[29] This fullerene device, despite it needs further optimization, presents a significant efficiency close to 9%. The achieved value for J_{sc} (15.8 mA cm^{-2}) was comparable to the reference device with spiro-OMeTAD as HTM prepared in the same device series (Figure S30). However, FF (62.5%) and V_{oc} (0.92 V), although decent, were significantly lower than those from spiro-OMeTAD reference device. It is worth noting that not levelling-effect was detected for **FU7** film in FE-SEM micrographs of the device cross-section (Figure 4a). This finding differs from the efficient levelling-effect provided by spiro-OMeTAD layer.[29] As the glass/FTO/C_{60}/perovskite samples used in this study exhibited significant roughness, the HTL–levelling effect may be crucial for the solar cell performance anticipating wide room for improvement in the current non-intensively optimized **FU7** devices. However, the reached power conversion efficiency can be considered as a first proof of concept of "fullerene sandwich" perovskite solar cells. Most importantly, there is plenty of room for further optimization based on deposition processes more suitable for newly synthesized fullerene-based HTMs, with enhanced properties in respect to the novel **FU7**. In this regard, the rich chemical versatility of [60]fullerene hexakis adducts will allow the introduction of a great variety of hole transporting fragments, such as porphyrins, phthalocyanines or exTTF, which could improve and surpass the photovoltaic performance reported here for **FU7**.[30,31] In addition, a proper evaluation of oxidizing additives for **FU7** could help for the conductivity improvement with a positive effect in the performance.

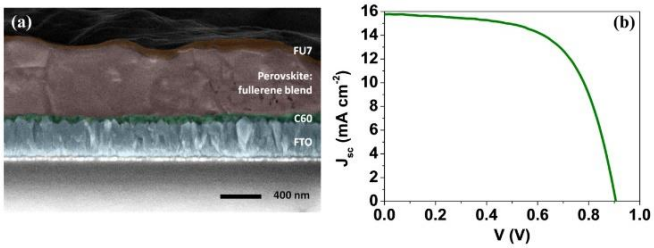

Figure 4. (a) Cross-section FE-SEM micrograph of a "fullerene sandwich" perovskite device with FTO/C_{60}/pvsk:C_{60}/**FU7**/Au architecture. Layers are colored for better discernment (FTO blue; C_{60} green; pvsk:C_{60} blend red; **FU7** brown). The local thickness of the fullerene layers depends on roughness of the layer on which they are deposited, being 10-40 nm for C_{60} and 10-50 nm for **FU7**. (b) *J-V* curve for champion solar device with "fullerene sandwich" architecture shown in (a), for comparison with reference cell see Figure S30.

In summary, we reported for the first time a HTM based on fullerenes. An appropriated chemical design has allowed tailoring the HOMO and LUMO levels of **FU7**, making it able to block electrons and act as hole selective contact. This molecule has been applied as HTM in PSCs without any additive. Significant efficiencies have been reported obtaining 0.77 in average (0.81 for champion devices) times the performance of the reference cell prepared with doped spiro-OMeTAD. In addition, cells prepared with **FU7** present higher stability than the reference cells. The presence of fullerenes play a structural key role in the HTM as it permits the formation of spherical molecules with charge separation, an easy transport pathway interconnection and an increase in the structural order of the film resulting on higher device performance. Finally, we have reported for the first time efficient "fullerene sandwich" PSCs where both selective contacts are fullerene-based systems and the active layer itself also contains fullerenes. Our results could have important implications in the development of a new branch in the family of fullerene derivatives, taking the advantage of the enormous knowledge already acquired in the synthesis of this kind of compounds but applying in a completely new field as HTL and electron blocking systems.

Acknowledgements

This work was partially supported by the MINECO of Spain (Grant Number CTQ2015-70921), Red Guipuzcoana de Ciencia, Tecnología e Innovación (MSFP) and European Research Council (ERC) via Consolidator Grant (724424 - No-LIMIT). J.P. and. S.C. acknowledge the Basque Government for a PhD research grant. J.P. and J.L.D. acknowledge Iberdrola Foundation for financial support. We thank Carles Felip and Francisco Galindo from University Jaume I (UJI) for their help with TRPL measurements. We also thank Ivet Kosta (CIDETEC) for the FESEM characterization of the "fullerene sandwich" perovskite solar cells. We acknowledge SCIC from UJI for help with XRD and SEM characterization.

Keywords: Fullerenes • HTMs • PSCs • Fullerene-Sandwich PSCs

[1] a) C.-Z. Li, H.-L. Yip, A. K. Y. Jen, *J. Mater. Chem.* **2012**, *22*, 4161–4177; b) B. C. Thompson and J. M. J. Frechet, *Angew. Chem. Int. Ed*. **2008**, *47*, 58–77; c) J.-F. Nierengarten, *New J. Chem*. **2004**, *28*, 1177-1191; d) J.-F. Nierengarten, *Sol. Energy Mater. Sol. Cells* **2004**, *83*, 187–199.

[2] a) The LUMO levels of PCBM and **FU7** were estimated by CV or DPV under the same experimental conditions, using the following equation which is discussed on the SI (Experimental methods) *E* (HOMO/LUMO) = –5.16 eV – $E_{(oxidation/reduction)}$; b) M. Cheng, C. Chen, X. Yang, J. Huang, F. Zhang, B. Xu and L. Sun, *Chem. Mater*., **2015**, *27*, 1808–1814; c) S. Kazim, F. J. Ramos, P. Gao, M. K. Nazeeruddin, M. Grätzel and S. Ahmad, *Energy Environ. Sci*., **2015**, *8*, 1816–1823; d) C. H. Teh, R. Daik, Eng L. Lim, C. C. Yap, M. A. Ibrahim, N. A. Ludin, K. Sopiana, M. A. M. Teridi, | *J. Mater. Chem. A*, **2016**, *4*, 15788–15822.

[3] a) S. F. Völker, S. Collavini, J. L. Delgado, *ChemSusChem* **2015**, *8*, 3012-3028; b) S. Kazim, M. K.Nazeeruddin, M. Grätzel, S. Ahmad, *Angew. Chem. Int. Ed.* **2014**, *53*, 2812–2824; c) S. Collavini, S. F. Völker, J. L. Delgado, *Angew. Chem. Int. Ed*. **2015**, *54*, 9757–9759; d) V. Dyakonov, J. L. Delgado, *Adv. Energy Mater*. **2017**, *7*, 1700252; S. Collavini, J. L. Delgado, *Adv. Energy Mater*. **2017**, *7*, 1601000.

[4] a) J.-F. Nierengarten, *Chem. Commun*. **2017**, *53*, 11855-11868; b) P. Fortgang, E. Maisonhaute, C. Amatore, B. Delavaux-Nicot, J. Iehl and J.-F. Nierengarten, *Angew. Chem., Int. Ed*. **2011**, *50*, 2364–2367; c) P. Compain, C. Decroocq, J. Iehl, M. Holler, D. Hazelard, T. Mena Barragán, C. Ortiz Mellet and J.-F. Nierengarten, *Angew. Chem. Int. Ed.* **2010**, 49, 5753–5756; d) A. Muñoz et al., *Nat. Chem.* **2016**, *8*, 50–57; e) J. Iehl, R. Pereira De Freitas, B. Delavaux-Nicot, J.-F. Nierengarten, *Chem Commun*. **2008**, 2450–2452.

[5] a) C. Boudon, J.-P. Gisselbrecht, M. Gross, L. Isaacs, H. L. Anderson, R. Faust, F. Diederich, *Helv. Chim. Acta 1995*, *78*, 1334–1344; b) L. Echegoyen, L. E Echegoyen, *Acc. Chem. Res.* **1998**, *31*, 593–601.

[6] M. J. Frisch et al., Gaussian 09, Revision A.1., Gaussian Inc., Wallingford CT, **2009**.

[7] W. S. Yang et al., *Science* **2017**, *356*, 1376-1379.

[8] J. L. Delgado, P.-A. Bouit, S. Filippone, M. A. Herranz, N. Martin, *Chem. Comm*. **2010**, *46*, 4853-4865.

[9] a) Y. Fang, C. Bi, D. Wang, J. Huang, *ACS Energy Letters* **2017**, *2*, 782-794; b) C. Cui, Y. Li, Y. Li, *Adv. Energy Mater*. **2017**, *7*, 1601251; c) T. Gatti, E. Menna, M. Meneghetti, M. Maggini, A. Petrozza, F. Lamberti, *Nano Energy* **2017**, *41*, 84–100.

[10] a) J. Pascual, I. Kosta, T. Tuyen Ngo, A. Chuvilin, G. Cabanero, H. J. Grande, E. M. Barea, I. Mora-Seró, J. L. Delgado, R. Tena-Zaera,

ChemSusChem **2016**, *9*, 2679-2685; b) S. Collavini, M. Saliba, W. R. Tress, P. J. Holzhey, S. F. Völker, K. Domanski, S. H. Turren-Cruz, A. Ummadisingu, S. M. Zakeeruddin, A. Hagfeldt, M. Grätzel, J. L. Delgado, *ChemSusChem* **2018**, doi:10.1002/cssc.201702265; c) R. Sandoval-Torrientes, J. Pascual, I. García-Benito, S. Collavini, I. Kosta, R. Tena-Zaera, N. Martín, J. L. Delgado, *ChemSusChem* **2017**, *10*, 2023.

[11] W. Wu, X. Yang, W. Chen, Y. Yue, M. Cai, F. Xie, E. Bi, A. Islam, L. Han, *Nat. Energy* **2016**, *1*, 16148.

[12] Y. Shao, Z. Xiao, C. Bi, Y. Yuan, J. Huang, *Nat. Commun.* **2014**, *5*, 5784.

[13] M. Valles-Pelarda, B. C. Hames, I. García-Benito, O. Almora, A. Molina-Ontoria, R. S. Sánchez, G. Garcia-Belmonte, N. Martín, I. Mora-Sero, *J. Chem. Phys. Lett.* **2016**, *7*, 4622-4628.

[14] Y. Bai, Q. Dong, Y. Shao, Y. Deng, Q. Wang, L. Shen, D. Wang, W. Wei, J. Huang, *Nat. Commun.* **2016**, *7*, 12806.

[15] H.-S. Kim et al., *Sci. Rep.* **2012**, *2*, 591.

[16] M. M. Lee, J. Teuscher, T. Miyasaka, T. N. Murakami, H. J. Snaith, *Science* **2012**, *338*, 643-647.

[17] C. Aranda, C. Cristobal, L. Shooshtari, C. Li, S. Huettner, A. Guerrero, *Sustainable Energy Fuels* **2017**, *1*, 540-547.

[18] E. J. Juarez-Perez, M. Wuβler, F. Fabregat-Santiago, K. Lakus-Wollny, E. Mankel, T. Mayer, W. Jaegermann, I. Mora-Sero, *J. Chem. Phys. Lett.* **2014**, *5*, 680-685.

[19] The addition to **FU7** films of the same additives employed for spiro-OMeTAD produced a dramatic decrease of performance (Figure S28).

[20] This system has attained in average an efficiency 0.92 times the value for the reference samples prepared with doped spiro-OMeTAD. But it is important to highlight that a higher performing mixed perovskite with methylammonium and formamidinium organic cations and iodine and bromide anions was employed. S. Paek et al., , *Adv. Mater.* **2017**, 1606555.

[21] C. Huang, W. Fu, C.-Z. Li, Z. Zhang, W. Qiu, M. Shi, P. Heremans, A. K. Y. Jen, H. Chen, *J. Am. Chem. Soc.* **2016**, *138*, 2528-2531.

[22] A. Dualeh, T. Moehl, N. Tétreault, J. Teuscher, P. Gao, M. K. Nazeeruddin, M. Grätzel, *ACS Nano* **2014**, *8*, 362-373.

[23] H.-S. Kim, J.-W. Lee, N. Yantara, P. P. Boix, S. A. Kulkarni, S. Mhaisalkar, M. Grätzel, N.-G. Park, *Nano Lett.* **2013**, *16*, 2412-2417.

[24] J. Jiménez-López, W. Cambarau, L. Cabau, E. Palomares, *Sci. Rep.* **2017**, *7*, 6101.

[25] G. Xing, N. Mathews, S. Sun, S. S. Lim, Y. M. Lam, M. Grätzel, S. Mhaisalkar, T. C. Sum, *Science* **2013**, *342*, 344-347.

[26] D.-Y. Son et al., *Nat. Energy* **2016**, *1*, 16081.

[27] A. Fakharuddin, L. Schmidt-Mende, G. Garcia-Belmonte, R. Jose, I. Mora-Seró, *Adv. Energy Mater.* **2017**, 1700623.

[28] Y. Shao, Y. Yuan, J. Huang, *Nat. Energy* **2016**, *1*, 15001.

[29] S. Collavini, I. Kosta, S. F. Völker, G. Cabanero, H. J. Grande, R. Tena-Zaera, J. L. Delgado, *ChemSusChem* **2016**, *9*, 1263-1270.

[30] D. M. Guldi, N. Martin, *Fullerenes: From Synthesis to Optoelectronic Properties. Vol. 4*, Springer Netherlands, Dordrecht, **2002**..

[31] F. Langa, J.-F. Nierengarten, *Fullerenes. Principles and Applications*, RSC, Cambridge, **2007**.

Entry for the Table of Contents (Please choose one layout)

Layout 1:

COMMUNICATION

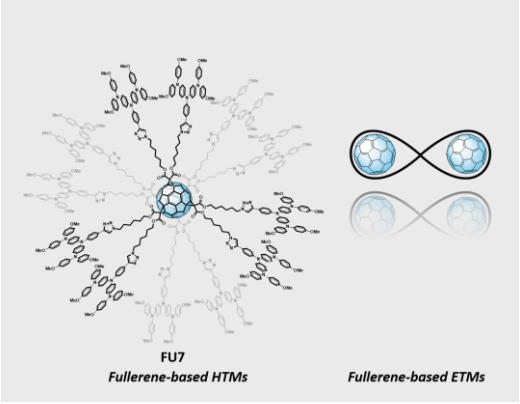

S. F. Völker, M. Vallés-Pelarda, J. Pascual, S. Collavini, F. Ruiperez, E. Zuccatti, L. Hueso, R. Tena-Zaera, I. Mora-Seró,* and J. L. Delgado**

Page No. – Page No.

Fullerene-Based Materials as Hole-Transporting/Electron Blocking Layers.

Applications in Perovskite Solar Cells

Supporting Information

Fullerene-based materials as hole-transporting layers. Applications in perovskite solar cells

Sebastian F. Völker,[a]+ Marta Vallés-Pelarda,[b]+ Jorge Pascual,[c] Silvia Collavini,[a] Fernando Ruiperez,[a] Elisabetta Zuccatti,[d] Luis Hueso,[d,e] Ramón Tena-Zaera,*[c] Iván Mora-Seró,*[b] and Juan Luis Delgado*[a,e]

[a] Dr. S. F. Völker, S. Collavini, Prof. J. L. Delgado
POLYMAT, University of the Basque Country UPV/EHU.
Avenida de Tolosa 72, 20018 Donostia-San Sebastián, Spain.
E-mail: juanluis.delgado@polymat.eu

[b] M. Vallés-Pelarda, Dr. I. Mora-Seró
Institute of Advanced Materials (INAM), University of Jaume I.
Av. de Vicent Sos Baynat, s/n 12006, Castelló de la Plana, Spain.
E-mail: sero@fca.uji.es

[c] J. Pascual, Dr. R. Tena-Zaera
Materials Division, IK4-CIDETEC
Parque Tecnológico de San Sebastián, Paseo Miramón, 196,
Donostia – San Sebastián 20009, Spain.
E-mail: rtena@cidetec.es

[d] E. Zuccatti, Prof. L. Hueso
CIC nanoGUNE Consolider, 20018 Donostia – San Sebastián, Spain

[e] Prof. L. Hueso, Prof. J. L. Delgado
Ikerbasque, Basque Foundation for Science, 48011 Bilbao, Spain.

+ Both authors have contributed equally to this work.

Experimental Methods

Synthesis and materials. Chemicals were purchased from commercial suppliers and used without further purification. Reactions under nitrogen or argon atmosphere were performed in flame-dried glass ware with dry solvents. For flash chromatography silica gel (40–60 μm) from Acros was used. **TAA2** was synthesised according to literature procedure.[1]

Material characterization. NMR spectra were recorded on either a Bruker Avance 300 (^{1}H: 300.2 MHz, ^{13}C: 75.5 MHz) or 500 (^{1}H: 500.1 MHz, ^{13}C: 125.8 MHz) at room temperature. The chemical shift (δ) is quoted in ppm relative to the internal standard tetramethylsilane (TMS). The coupling constant *J* is given in Hertz (Hz). Proton spin multiplicities and C-atom depictions are: s = singlet, d = doublet, t = triplet, q = quartet, m = multiplet; prim = primary, sec = secondary, tert = tertiary, quart = quaternary.

Mass spectra were recorded on either a Bruker-AUTOFLEX SPEED in San Sebastián or on a Bruker-ULTRAFLEX III (MALDI-TOF) in the facilities of the Universidad Autónoma de Madrid.

Infrared spectra were recorded either from the pure sample or from toluene solution on a Bruker ALPHA ATR-IR spectrometer.

UV-Vis spectra were recorded with a PerkinElmer Lambda 950 UV/Vis/NIR spectrometer. Experiments were carried out in 1 cm quartz cuvettes and neat solvent was used as reference.

Fluorescence and excitation spectra were recorded with a PerkinElmer LS 55 fluorescence spectrometer. Experiments were carried out in 1 cm quartz cuvettes.

Electrochemical experiments were performed with a Princeton Applied Research Parstat 2273 in a custom made glass cell using a three electrode setup with a platinum working electrode (Ø = 0.5 mm), a

platinum wire counter electrode (Ø = 0.5 mm), and a $Ag/AgNO_3$ wire pseudoreference electrode in DCM with tetrabutylammonium hexafluorophosphate (TBAHFP) as supporting electrolyte (c = 0.1–0.2 M). Cyclic voltammograms and differential pulse voltammograms were recorded at a scan rate of 250 mV s^{-1} and 50 mV s^{-1}, respectively, and referenced *vs* the ferrocene/ferrocenium (Fc/Fc^+) redox couple. To avoid an overlap of the high oxidation potential of **FU7** and ferrocene we used decamethylferrocene/decamethylferrocenium as reference, which in an additional experiment was found to have an oxidation potential of –555 mV *vs* ferrocene/ferrocenium (Fc/Fc^+). HOMO and LUMO energy levels were obtained from the half-wave potentials of the cyclic voltammetry or the peak potentials of the osteryoung square-wave voltammetry measurements. The potential of Fc/Fc^+ in TBAHFP/DCM is 0.46 eV *vs* the saturated calomel electrode SCE,[2] whose potential is 0.244 V *vs* the normal hydrogen electrode (NHE).[3] This has an absolute potential of 4.46 eV *vs* vacuum, which leads to the applied equation: E(HOMO/LUMO)= –5.16 eV – E(oxidation/reduction).[4]

Chemicals Involved in Solar Cell preparation. Titanium diisopropoxidebis(acetylacetonate), anhydrous dimethylformamide (DMF), anhydrous chlorobenzene, lithium bis(trifluoromethylsulfonyl)imide (Li-TFSI), and 4-*tert*-butylpiridine (TBP) were purchased from Sigma-Aldrich. Methylammonium iodide (MAI) and lead iodide (PbI_2) were purchased from TCI and TiO_2 30NR-D paste was purchased from Dyesol. All the materials were used as received.

Solar Cell preparation using TiO_2 as electron selective contact. Fluorine doped tin oxide (FTO) coated glass substrates (Pilkington TEC15, ~ 15 Ω sq^{-1}) were etched with zinc powder and HCl (2M),cleaned with soap (Hellmanex), rinsed with Milli-Q water, sonicated for 10 min in a solution of ethanol, rinsed with acetone and dried with compressed air. Just before depositing the compact layer, they were treated with UV/ozone for 15 min. TiO_2 compact layer was deposited onto the substrates by spray pyrolysis at 450 °C, using titanium diisopropoxidebis(acetylacetonate) diluted in ethanol (1:9,

v/v). Mesoporous TiO_2 layer was deposited by spin coating at 2000 rpm during 10 s using TiO_2 paste diluted in ethanol (1:5, weight ratio). After drying at 100°C 10 min, they were heated at 500°C for 30 min and cooled down to room temperature. The perovskite solution was prepared by dissolving PbI_2 (1.35 M) and MAI (1.35M) in 1 mL DMF and 80-95 µL DMSO depending on the humidity.[5] The perovskite layer was deposited by spin-coating at 4000 rpm 50 s adding an antisolvent, diethyl ether, at approximately 9 s. After the deposition, the substrates were heated at 100°C during 3 min in a hot plate. The HTMs were deposited by spin coating at 4000 rpm for 30 s, the spiro-OMeTAD was added while spinning. The spiro-OMeTAD solution was prepared dissolving 72.3 mg of spiro-OMeTAD in 1 mL of chlorobenzene, adding 28.8 µL of TBP and 17.5 µL of a stock solution of 520 mg mL^{-1} of Li-TFSI in acetonitrile. The **FU7** and the functional group were dissolved in chlorobenzene at different concentrations and sonicated for 30 min before the deposition. It was deposited by spin coating at 4000 rpm for 30 s. Finally, 60 nm of gold were deposited by thermal evaporation at 10^{-6} mbar. All the samples were prepared in air conditions.

Solar Cell preparation using C_{60} as electron selective contact. The [60]fullerene films were deposited by spin-coating in an argon-filled glovebox. A two step protocol with a first step of 1500 rpm for 60 s and a second step of 2700 rpm for 60 s was followed. The perovskite solution was prepared by dissolving 7.71 mmol of MAI and 2.57 mmol of $PbCl_2$ (molar ratio 3:1) in 3 mL of DMF and stirring overnight. Prior to deposition, the perovskite solution was saturated with [60]fullerene. The resulting solution was spin coated on the substrates following a two-step protocol, which consisted of a first step of 500 rpm for 5 s followed by a second step of 2000 rpm for 45 s. Subsequently, the samples were annealed at 100ºC for 2 h to ensure complete perovskite formation. On top of the perovskite layer, the spiro-OMeTAD hole-selective contact was deposited from a solution that contained spiro-OMeTAD (108.4 mg) in chlorobenzene (953.43 µL), LiTFSI solution in MeCN (17.17 µL, 520 mg ml^{-1}), and *tert*-butylpyridine (29.4 µL). **FU7** was deposited using the same procedure than for samples on TiO_2 substrate. The HTM was deposited by spin coating the solution at 3000

rpm for 30 s. The samples were left in a desiccator overnight. Finally, an array of round Au back contacts (~0.07 cm^2) was deposited by thermal evaporation at more than 5 x 10^{-6} torr with a NANO38 (Kurt J. Lesker) apparatus with a shadow mask.

Device characterization. The current−voltage curves were measured in Abet Technologies Sun 2000Class A solar simulator (AM1.5G, 100 mW cm^{-2}) with a Keithley 2612 Source Meter. The measurements were performed at 50 mV s^{-1} with a dwell time of ~ 0.25 s using a mask with an area of 0.107 cm^2. PL measurements were carried out in a HORIBA FL-1000 Fluorimeter. The time resolved photoluminescence (TRPL) response was acquired using time-correlated single-photon counting (TCSPC) (IBH-5000-U, HORIBA) using a LED (464 nm) as excitation light source. IPCE measurements were performed with a QEPVSI-b Oriel measurement system. SEM characterization was performed using a field emission scanning electron microscope (FEG-SEM) JEOL 7001F. Impedance Spectroscopy measurements were performed using a Metrohm Autolab PGSTAT30 potentiostat.

Synthesis

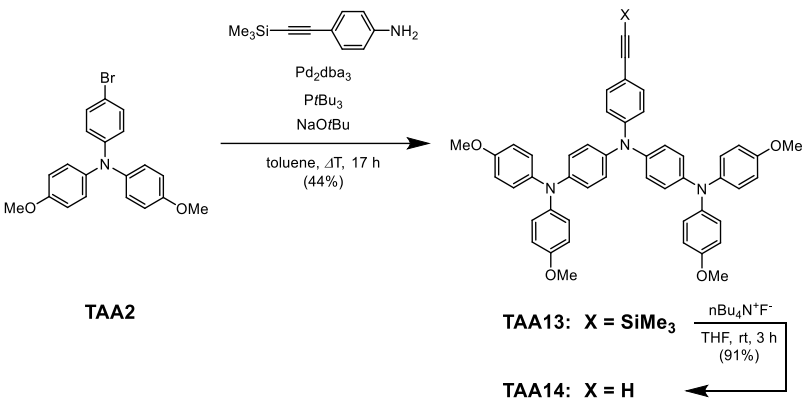

Scheme S1. Synthesis of the super-triarylamine ligand **TAA14**.

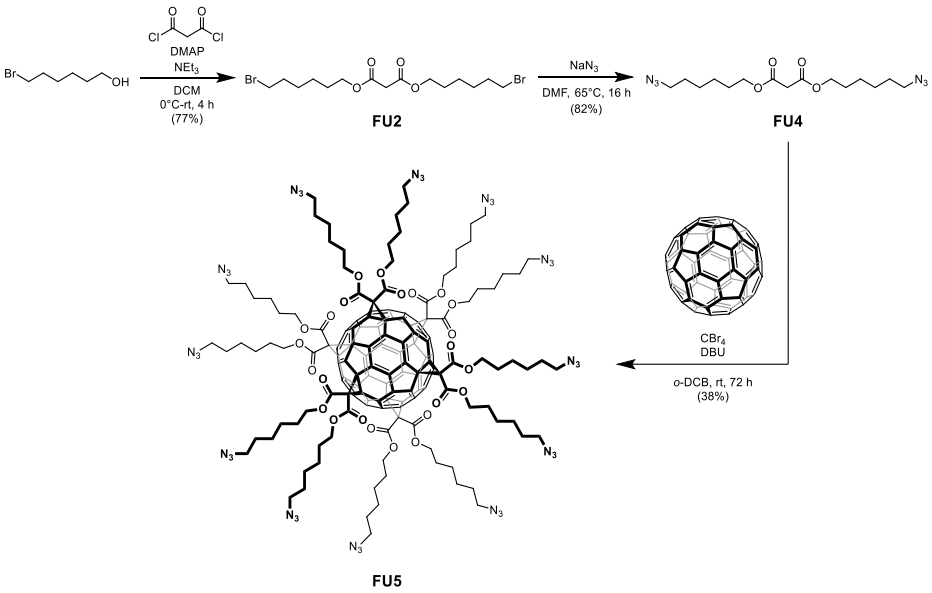

Scheme S2. Synthesis of functionalized fullerene core **FU5**.

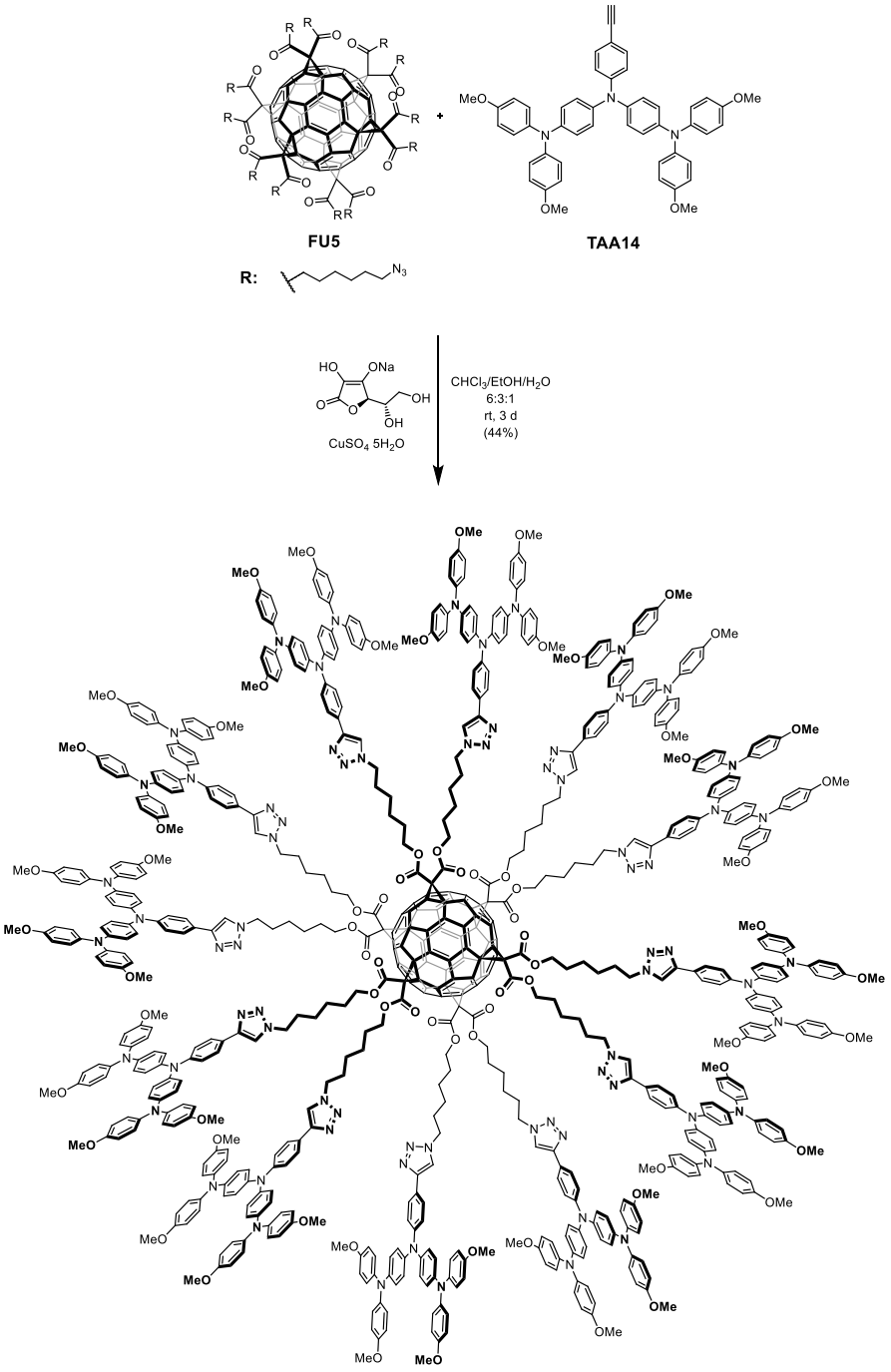

Scheme S3. Synthesis of target compound **FU7**.

*Synthesis of **TAA13***

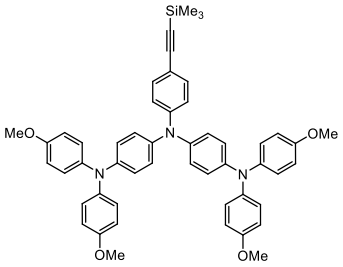

TAA2 (2.03 g, 5.28 mmol), 4-((trimethylsilyl)ethynyl)aniline (500 mg, 2.64 mmol), and NaO*t*Bu (990 mg, 10.3 mmol) were dissolved in dry toluene (14 ml) under Ar atmosphere and the mixture was degassed in a stream of Ar for 10 min. Pd_2dba_3 (193 mg, 211 μmol) and P*t*Bu_3 (1 M in toluene, 211 μl) were added and the mixture was refluxed for 1 d. The solvent was removed under reduced pressure and the residue was purified by column chromatography (eluent:DCM/hexane 2:1). The product was obtained as a yellow solid (491 mg, 617 μmol, 23%). **^{1}H-NMR** (300.2 MHz, d^6-acetone): δ[ppm] = 7.27–7.19 (AA', 2 H), 7.10–7.02 (AA', 8 H), 7.02–6.94 (AA', 4 H), 6.94–6.76 (14 H), 3.77 (s, 12 H, OCH_3), 0.20 (s, 9 H, SiCH_3). **^{13}C-NMR** (75.5 MHz, d^6-acetone): δ [ppm] = 157.0 (quart), 149.9 (quart), 146.4 (quart), 141.7 (quart), 140.4 (quart), 133.5 (tert), 127.5 (tert), 127.3 (tert), 122.3 (tert), 119.7 (tert), 115.6 (tert), 114.5 (quart), 106.9 (quart), 92.5 (quart), 55.7 (prim), 0.2 (prim).

*Synthesis of **TAA14***

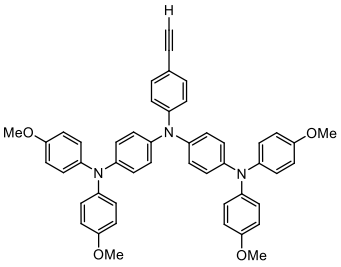

TAA13 (420 mg, 528 μmol) was dissolved in THF (15 ml) and TBAF (1 M in THF, 739 μl, 739 μmol) was added. After stirring the mixture at rt for 75 min the solvent was removed under reduced pressure. The residue was dissolved in DCM (30 ml) and H_2O (30 ml), the phases were separated, the aqueous phase was extracted with DCM (2 x 30 ml), the combined organic phases were washed with H_2O (30 ml), dried over Na_2SO_4, and the solvent was removed under reduced pressure to give the product as yellow powder (338 mg, 467 μmol, 91%). **^{1}H-NMR** (500.1 MHz, C_6D_6): δ [ppm] = 7.40–7.30 (AA', 2 H), 7.13–7.04 (AA', 8 H), 7.04–6.94 (10 H), 6.77–6.67 (BB', 8 H), 3.34 (s, 12 H, OCH_3), 2.77 (s, 1 H, C≡CH). **^{13}C-NMR** (125.8 MHz, C_6D_6): δ [ppm] = 156.6 (quart), 149.5 (quart), 145.8

(quart), 141.8 (quart), 140.8 (quart), 133.5 (tert), 126.9 (tert), 126.7 (tert), 122.7 (tert), 120.5 (tert), 115.4 (tert), 114.4 (quart), 84.7 (tert), 76.3 (quart), 55.2 (prim).

*Synthesis of **FU2***

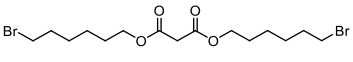

6-Bromohexanol (2.34 g, 12.9 mmol), *N*,*N*'-dimethylaminopyridine (35 mg, 284 μmol), and NEt_3 (2 ml) were dissolved in DCM (70 ml) at 0°C under Ar atmosphere. A solution of malonyl chloride (1.00 g, 7.09 mmol) in DCM (5 ml) was added within 1 min and the mixture was stirred at 0°C for 1 h and warmed to rt over night. The mixture was washed with HCl (1 M in H_2O, 2 x 25 ml) and brine (2 x 25 ml) and the organic fraction was dried over Na_2SO_4. The solvent was removed under reduced pressure and the residue purified by column chromatography (eluent: hexane/DCM 1:4). The product was obtained as yellowish oil (2.15 g, 4.99 mmol, 77%). **^{1}H-NMR** (300.2 MHz, $CDCl_3$): δ [ppm] = 4.15 (t, ^3J = 6.6 Hz, 4 H, CH_2), 3.41 (t, ^3J = 6.7 Hz, 4 H, CH_2), 3.37 (s, 2 H, CH_2), 1.93–1.82 (m, 4 H, CH_2), 1.73–1.62 (m, 4 H, CH_2), 1.54–1.33 (8 H, CH_2). **^{13}C-NMR** (75.5 MHz, $CDCl_3$): δ [ppm] = 166.8 (quart), 65.5 (sec), 41.8 (sec), 33.8 (sec), 32.7 (sec), 28.4 (sec), 27.9 (sec), 25.2 (sec).

Compound previously reported: J. Iehl, R. Pereira De Freitas, B. Delavaux-Nicot, J.-F. Nierengarten, *Chem Commun.* **2008**, 2450–2452.

*Synthesis of **FU4***

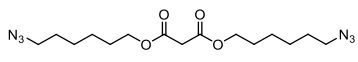

NaN_3 (907 mg, 14.0 mmol) and **FU2** (1.00 g, 2.33 mmol) were dissolved in DMF (8 ml) under Ar atmosphere and stirred at 65°C for 18 h. Upon cooling to rt the mixture was diluted with Et_2O (20 ml) and washed with water (40 ml) and brine (40 ml). The aqueous phase was extracted with Et_2O (20 ml) and the combined organic phases were dried over Na_2SO_4. The solvent was removed under reduced pressure and the residue purified by column chromatography (DCM). The product was obtained as yellow oil (675 mg, 1.91 mmol, 82%). **^{1}H-NMR** (300.2 MHz, $CDCl_3$): δ [ppm] = 4.15 (t, ^3J = 6.7 Hz, 4 H, CH_2), 3.37 (s, 2 H, CH_2),

3.27 (t, ^3J = 6.8 Hz, 4 H, CH_2), 1.74–1.57 (8 H, CH_2), 1.47–1.34 (8 H, CH_2). **^{13}C-NMR** (75.5 MHz, $CDCl_3$): δ [ppm] = 166.7 (quart), 65.5 (sec), 51.8 (sec), 41.7 (sec), 28.8 (sec), 28.5 (sec), 26.4 (sec), 25.5 (sec).

Compound previously reported: J. Iehl, R. Pereira De Freitas, B. Delavaux-Nicot, J.-F. Nierengarten, *Chem Commun.* **2008**, 2450–2452.

*Synthesis of **FU5***

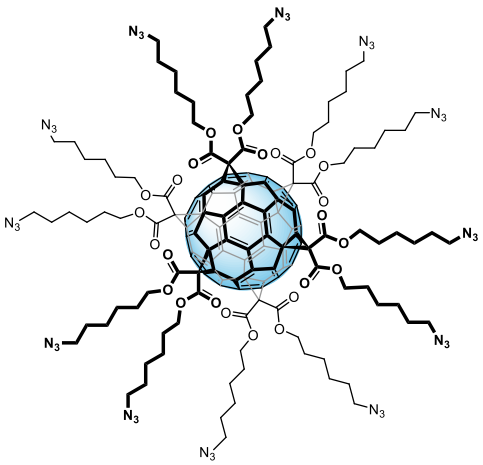

C_{60} (80 mg, 111 μmol), **FU4** (392 mg, 1.11 mmol), and CBr_4 (3.67 g, 11.1 mmol) were dissolved in *o*-DCB (33 ml) under Ar atmosphere and the mixture was stirred at rt for 5 min. Subsequently, DBU (337 mg, 2.21 mmol) was added and the mixture was stirred at rt for 3 d. The solvent was removed under reduced pressure and the residue was purified by column chromatography (eluent: PE/DCM 1:9 → DCM → DCM/EA 100:1 → 70:1) to yield a red glassy-like film. The product was stored as toluene solution in the fridge because isolated it decomposes in the solid state (140 mg, 49 μmol, 45%). **^{1}H-NMR** (300.2 MHz, $CDCl_3$): δ [ppm] = 4.25 (t, ^3J = 6.5 Hz, 24 H, CH_2), 3.25 (t, ^3J = 7.1 Hz, 24 H, CH_2), 1.85–1.15 (96 H, CH_2). **^{13}C-NMR** (75.5 MHz, $CDCl_3$): δ [ppm] = 163.8 (quart), 145.8 (quart), 141.2 (quart), 69.2 (quart), 66.8 (sec), 51.4 (sec), 45.6 (quart), 28.8 (sec), 28.4 (sec), 26.4 (sec), 25.5 (sec). **IR** (in toluene): $\tilde{\nu}$ [cm^{-1}] = 3025, 2920, 2868, 2096 (N_3), 1743, 1603, 1494, 1460, 1380, 1240, 1081, 1030, 727, 693, 463.

Compound previously reported: J. Iehl, R. Pereira De Freitas, B. Delavaux-Nicot, J.-F. Nierengarten, *Chem Commun.* **2008**, 2450–2452.

*Synthesis of **FU7***

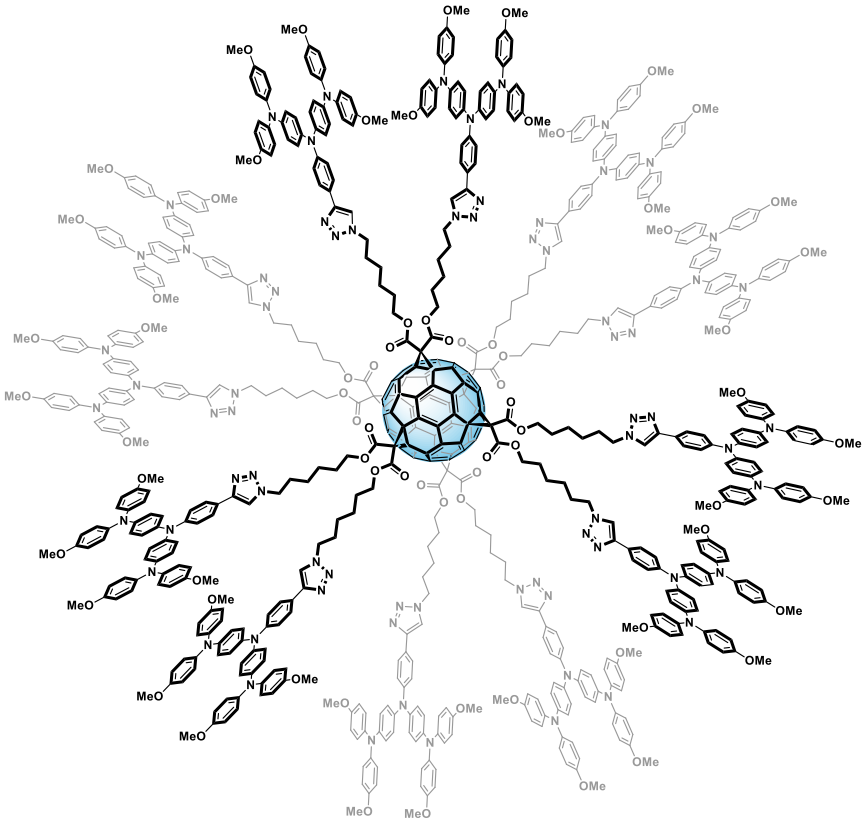

To a solution of **TAA14** (259 mg, 358 μmol) in $CHCl_3$ (6 ml) was added a solution of **FU5** (70 mg, 25 μmol) in $CHCl_3$ (6 ml) under Ar atmosphere. EtOH (6 ml), H_2O (2 ml), $CuSO_4 \cdot 5H_2O$ (15.4 mg, 62 μmol), and sodium ascorbate (36.7 mg, 185 μmol) were added and the mixture was stirred under the exclusion of light at rt for 3 d. DCM (10 ml) and H_2O (10 ml) were added, the phases separated, and the aqueous phase extracted with DCM (2 x 10 ml). The combined organic phases were washed with H_2O (10 ml) and brine (10 ml), dried over Na_2SO_4, and the solvent was removed under reduced pressure. The residue was purified by column chromatography (eluent: DCM/NEt_3 200:1 → DCM → DCM/MeOH 200:1 → 100:1 → 70:1) to give a brown solid. The solid was suspended in acetone (25 ml), stirred for 5 min at rt, and filtered. Subsequently, the solid was precipitated from DCM to pentane three times to give the product as beige powder (126 mg, 21 μmol, 44%). **^{1}H-NMR** (300.2 MHz, C_6D_6): δ [ppm] =

8.04–7.84 (24 H), 7.48 (12 H), 7.36–7.24 (24 H), 7.16–6.95 (192 H), 6.81–6.60 (96 H), 4.33–3.75 (48 H), 3.33 (s, 144 H), 1.76–1.41 (24 H), 1.37–1.15 (24 H), 1.15–0.84 (48 H). **^{13}C-NMR** (125.8 MHz, C_6D_6): δ [ppm] = 163.9 (quart), 156.3 (quart), 148.7 (quart), 147.9 (quart), 146.5 (quart), 145.1 (quart), 142.4 (quart), 141.8 (quart), 141.4 (quart), 127.1 (tert), 126.5 (tert), 126.4 (tert), 124.7 (quart), 122.9 (tert), 122.2 (tert), 119.2 (tert), 115.2 (tert), 70.4 (quart), 67.2 (sec), 55.1 (prim), 50.1 (sec), 47.3 (quart), 30.4 (sec), 28.4 (sec), 26.2 (sec), 25.6 (sec). **IR** (neat): $\tilde{\nu}$ [cm^{-1}] = 2933, 2833, 1741, 1610, 1493, 1234, 1030, 823, 718, 575, 538.

NMR spectra

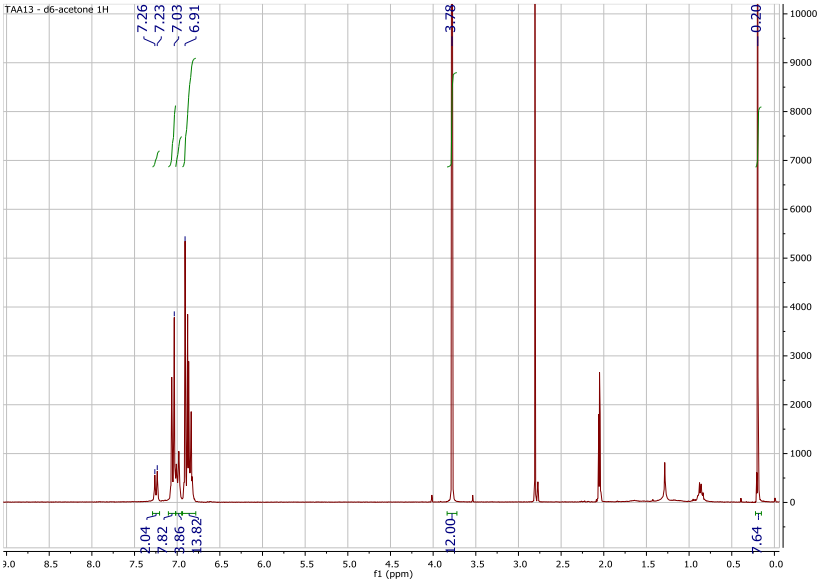

Figure S4. ^{1}H NMR spectrum of **TAA13** in d^6-acetone.

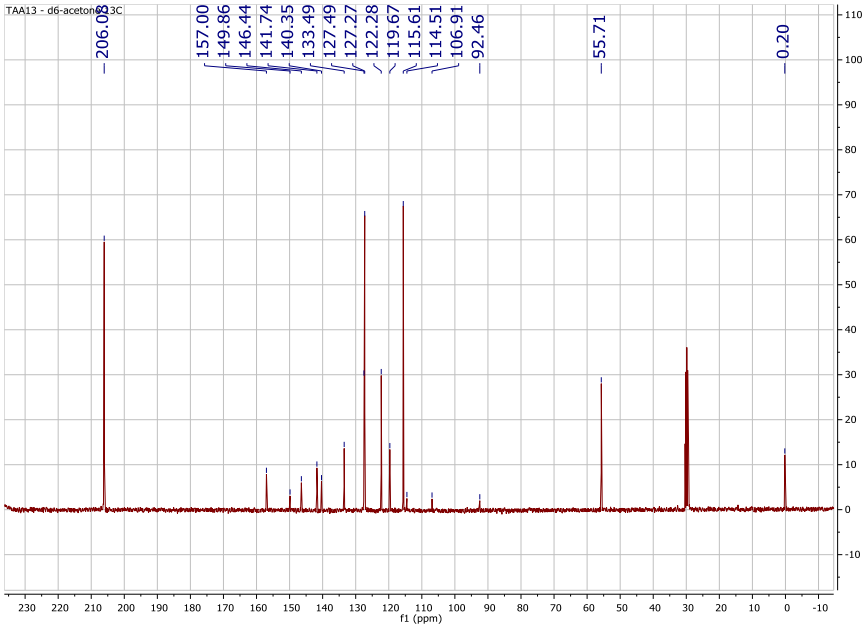

Figure S5. ^{13}C NMR spectrum of **TAA13** in d^6-acetone.

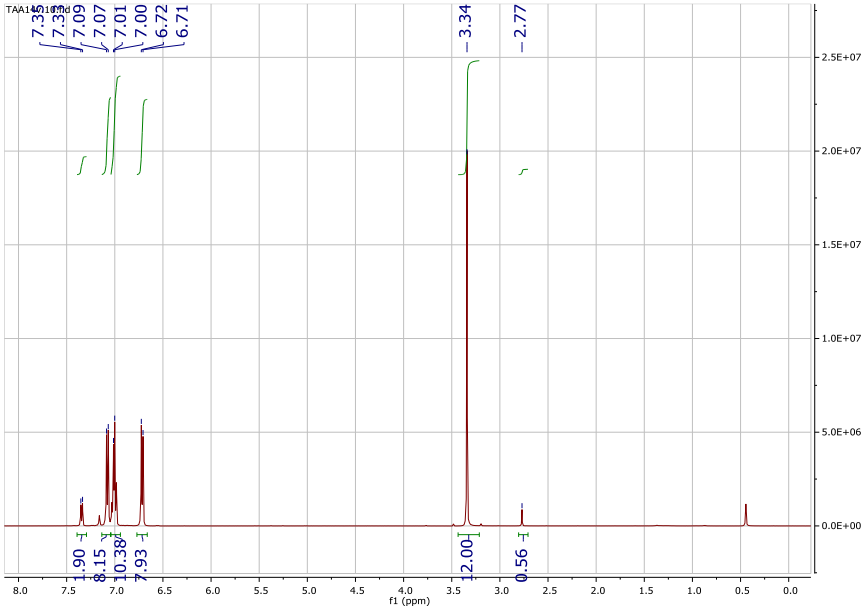

Figure S6. ^{1}H NMR spectrum of **TAA14** in C_6D_6.

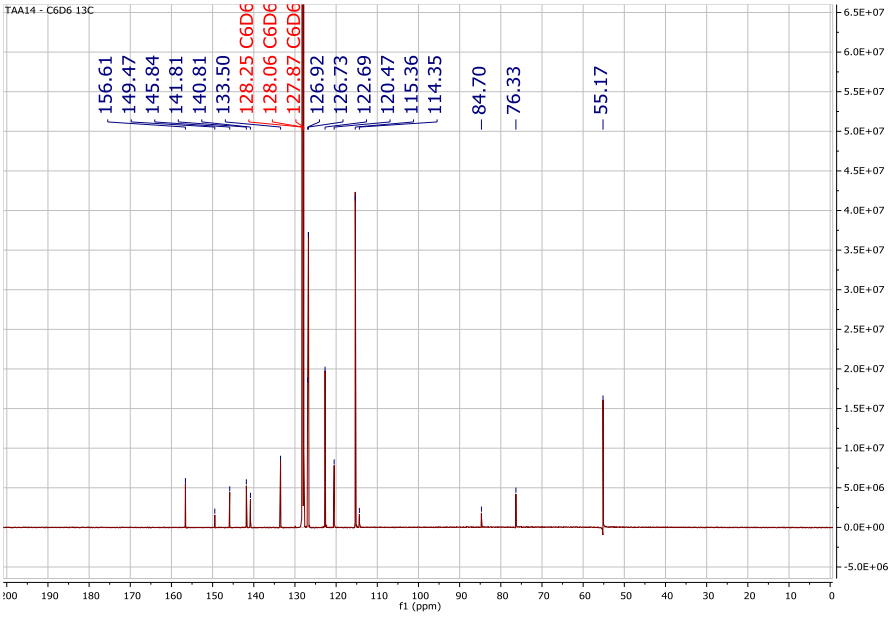

Figure S7. ^{13}C NMR spectrum of **TAA14** in C_6D_6.

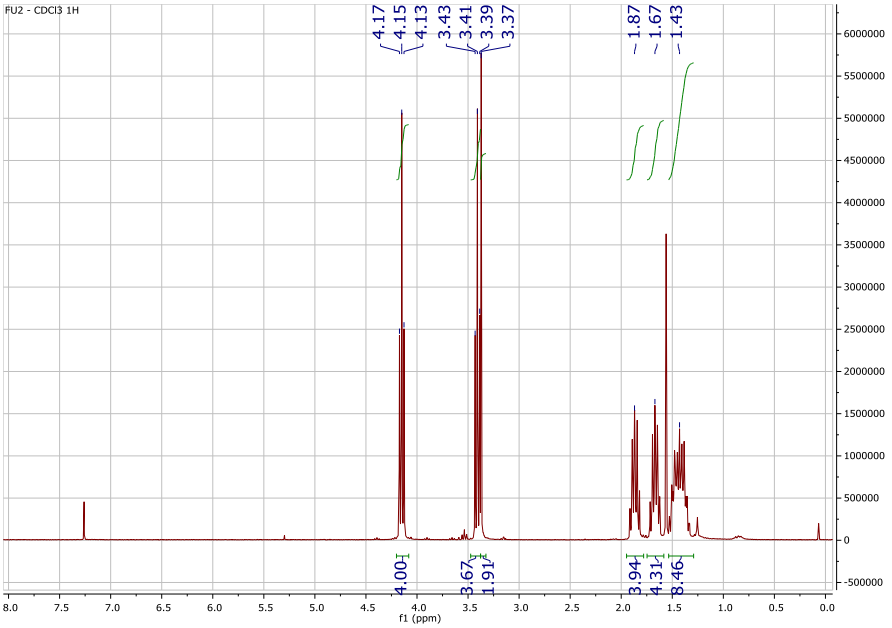

Figure S8. ^{1}H NMR spectrum of **FU2** in $CDCl_3$.

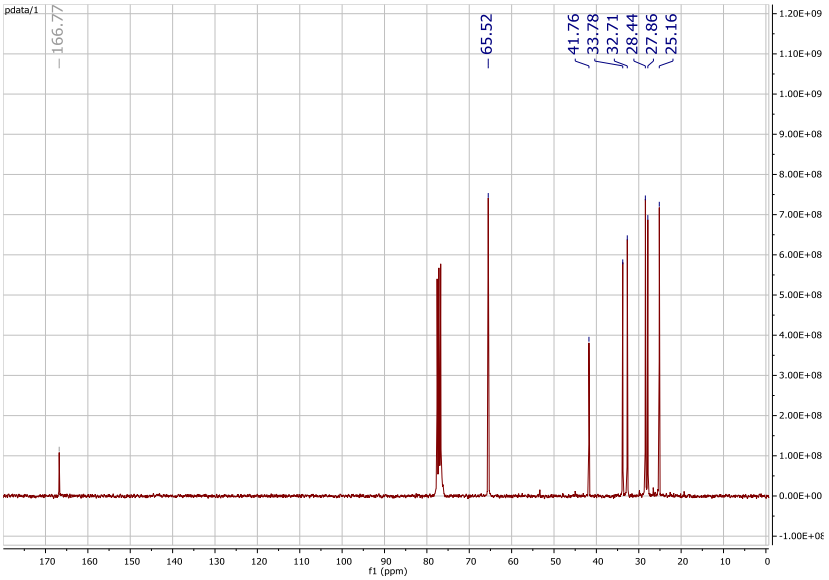

Figure S9. ^{13}C NMR spectrum of **FU2** in $CDCl_3$.

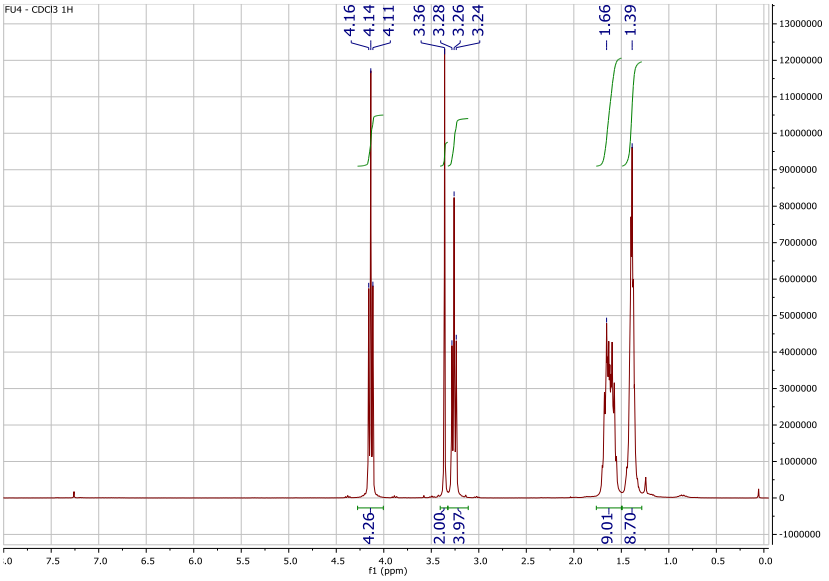

Figure S10. ^{1}H NMR spectrum of **FU4** in $CDCl_3$.

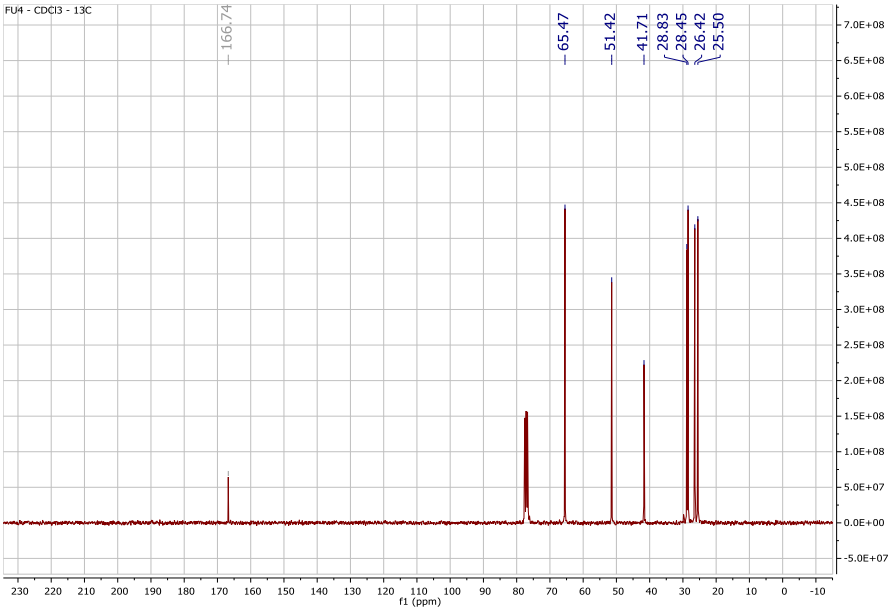

Figure S11. ^{13}C NMR spectrum of **FU4** in $CDCl_3$.

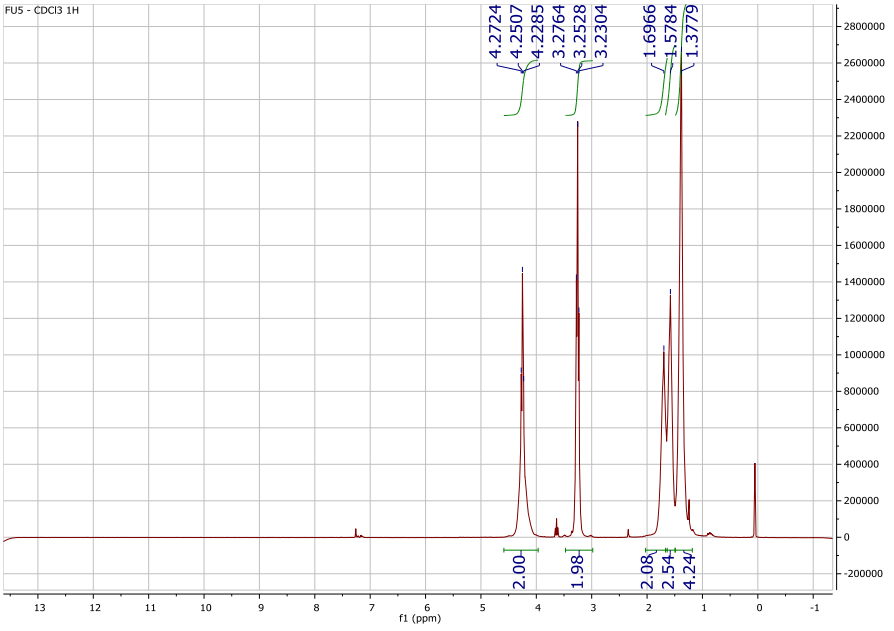

Figure S12. ^{1}H NMR spectrum of **FU5** in $CDCl_3$.

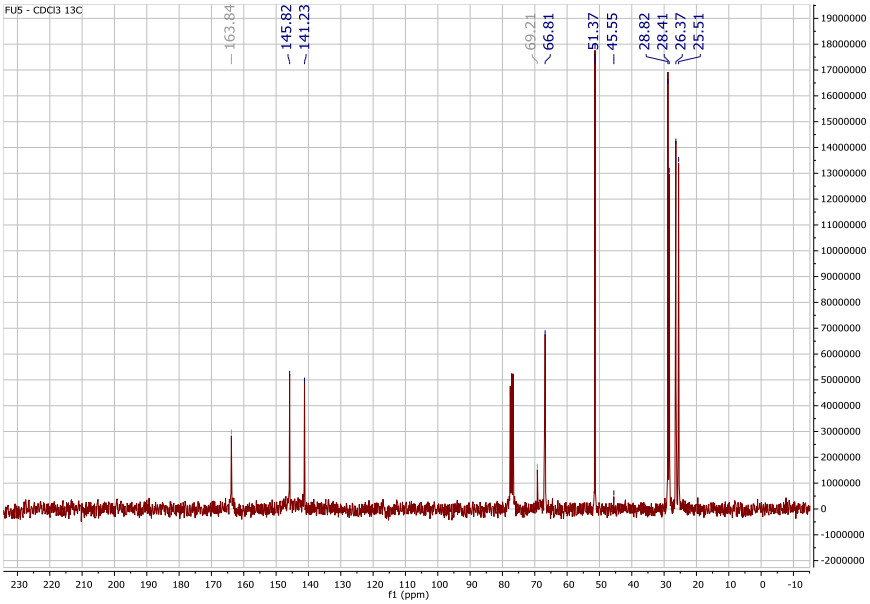

Figure S13. ^{13}C NMR spectrum of **FU5** in $CDCl_3$.

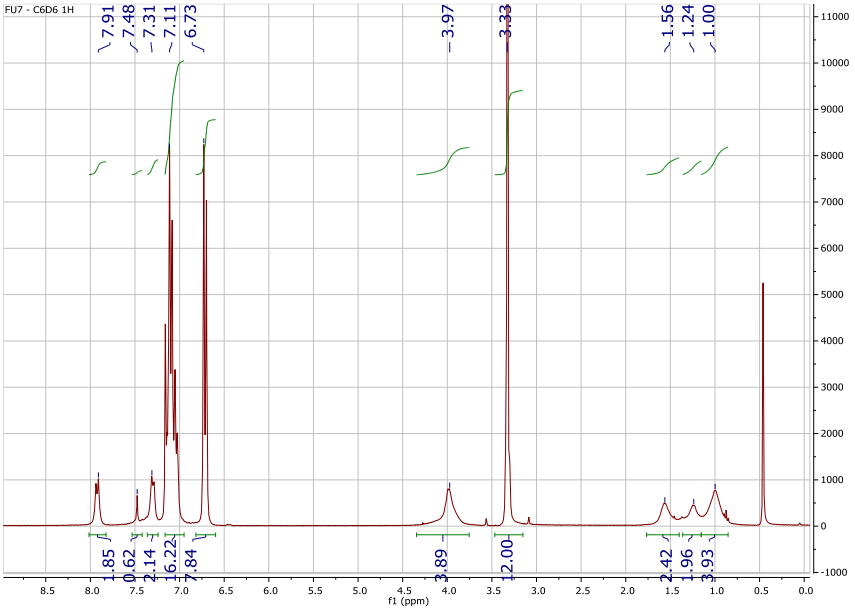

Figure S14. ^{1}H NMR spectrum of **FU7** in C_6D_6.

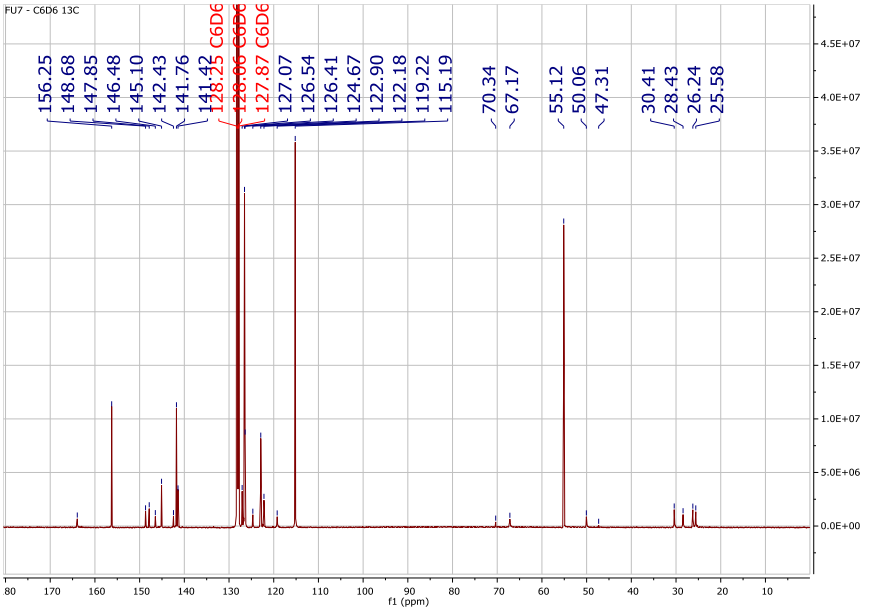

Figure S15. ^{13}C NMR spectrum of **FU7** in C_6D_6.

Mass spectrometry

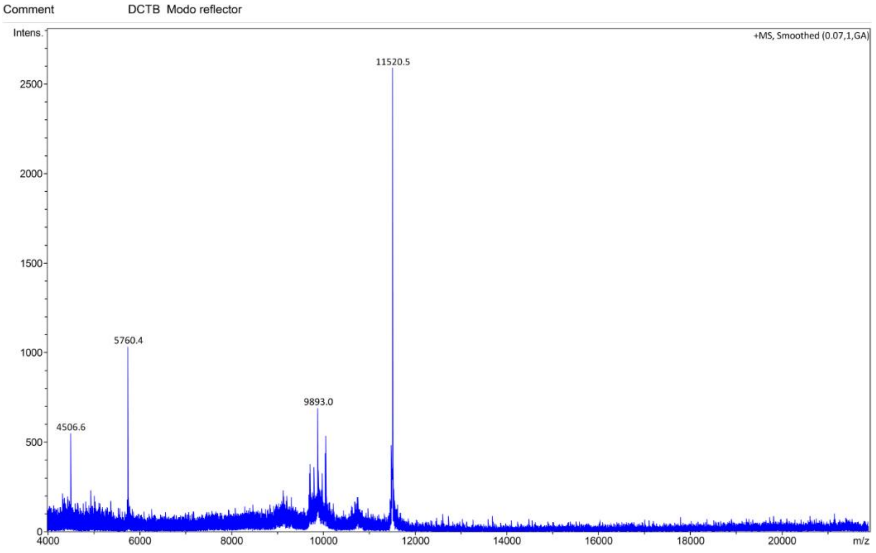

Figure S16. Complete MALDI-TOF spectrum of **FU7**.

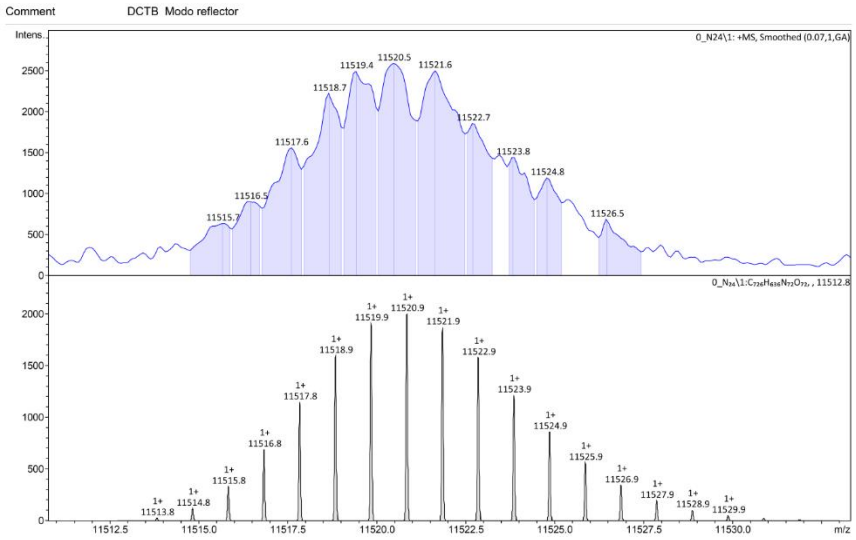

Figure S17. Amplification of the compound signal in the MALDI-TOF spectra of **FU7**.

IR spectroscopy

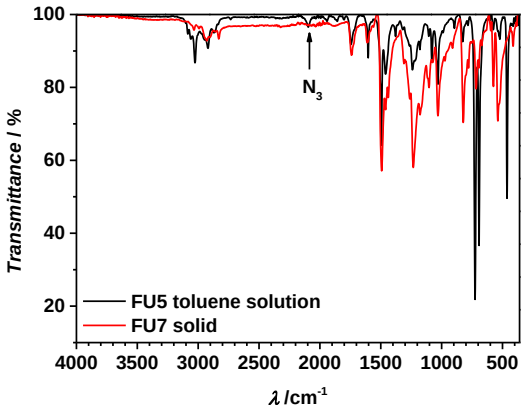

Figure S18. IR spectra of **FU5** (black, in toluene solution) and **FU7** (red, neat).

UV/Vis Absorption and Fluorescence Spectroscopy

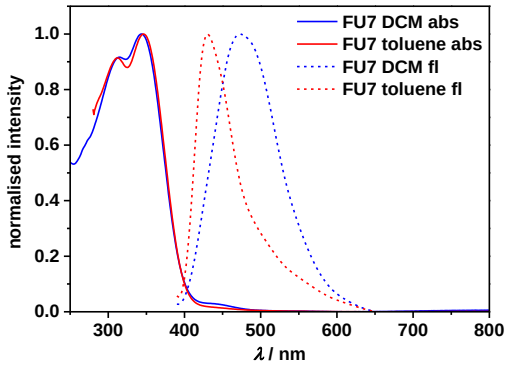

Figure S19. Absorption (solid lines) and fluorescence (dashed lines) spectra of **FU7** in DCM (blue) and toluene (red).

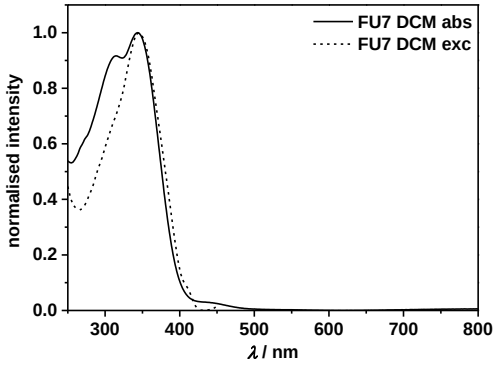

Figure S20. Absorption (solid line) and excitation (dashed line) spectra of **FU7** in DCM.

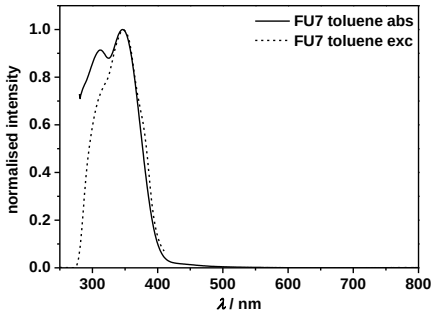

Figure S21. Absorption (solid line) and excitation (dashed line) spectra of **FU7** in toluene.

Cyclic Voltammetry

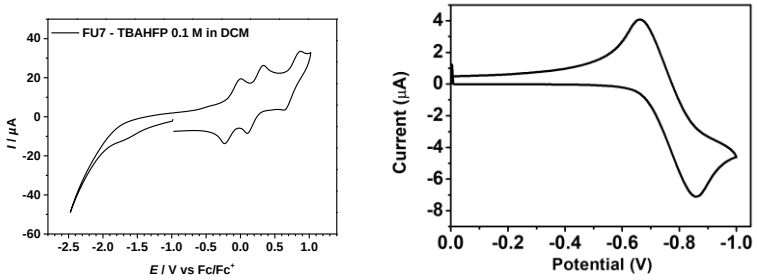

Figure S22. Cyclic voltammogram of **FU7** (left) and **PCBM** (right) in DCM/TBAHFP (0.1 M) at a scan rate of 250 mV s^{-1}.

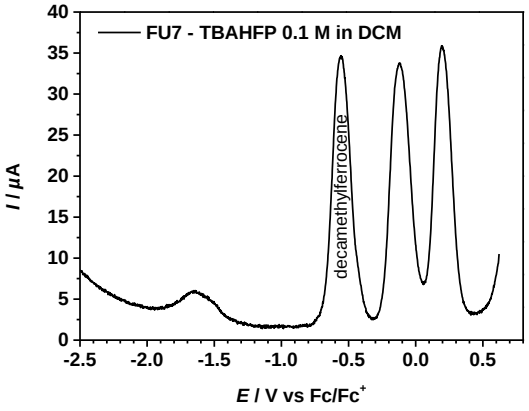

Figure S23. Differential pulse voltammogram of **FU7** in DCM/TBAHFP (0.1 M) at a scan rate of 50 mV s^{-1}.

Table S1. Solar Cell performance of PSCs prepared with **FU7** HTM. Different concentration in chlorobenzene. Power conversion efficiencies (η) have been obtained from the J-V curves (both forward and reverse scans are considered). The photocurrent, J_{sc}, photovoltage, V_{oc} and fill factor, FF of the champion cells obtained at each conditions are indicated. J-V curves are plotted in Fig. S24.

FU7	**Scan**	J_{sc} **(mA/cm2)**	V_{oc} **(mV)**	**FF(%)**	**η(%)**
5 mg/mL	reverse	17.8	954	63	10.7
	forward	19.3	958	51	9.3
7 mg/mL	reverse	19.5	985	65	12.4
	forward	20.2	988	60	11.9
8 mg/mL	reverse	20.4	976	68	13.6
	forward	21.4	970	54	11.3
9 mg/mL	reverse	20.8	985	67	13.7
	forward	22.1	980	53	11.4
10 mg/mL	reverse	21.1	943	64	12.7
	forward	21.5	953	56	11.4
30 mg/mL	reverse	16.0	881	29	4.1
50 mg/mL	reverse	9.3	822	22	1.7

Table S2. Solar Cell performance of PSCs prepared with spiro-OMeTAD, **FU7** and TAA14 as HTM. Average results for champion cells at such conditions are plotted. Cells with spiro-OMeTAD were prepared with additives (Ref) and without additives (Spiro no add). For **FU7**, cells prepared with 8-9 mg/ml concentration have been averaged. Champion cell with **FU7** has been obtained with 9 mg/ml concentration in chlorobenzene. Power conversion efficiencies (η) have been subtracted from the *J-V* curves (both forward and reverse scans are considered). We have verified that the stabilized efficiencies are very close to the efficiencies obtained with the *J-V* curve from the reverse scan (Figure S26). The photocurrent, J_{sc}, photovoltage, V_{oc} and fill factor, FF of the champion cells obtained at each conditions are indicated.

Sample		J_{sc} (mA/cm^2)	V_{oc} (mV)	FF (%)	η (%)
Ref	reverse	20.8±0.5	1040±10	74±5	16.0±1.2
	forward	20.7±0.5	1044±11	71±5	15.3±1.0
	reverse	21.7	1042	75	16.9
	forward	21.6	1052	68	15.4
TAA14	reverse	14.3±1.3	866±105	48±6	6.0±1.4
	forward	14.3±1.2	866±92	39±4	4.8±1.0
	reverse	15.8	925	52	7.6
	forward	15.6	917	42	6.1
FU7	reverse	20.6±0.7	948±26	64±3	12.5±0.8
	forward	21.5±0.6	950±26	52±2	10.5±0.6
	reverse	20.8	985	67	13.7
	forward	22.0	980	53	11.4
FU7+add	reverse	13.1±1.4	802±114	67±12	7.2±2.2
	forward	13.7±1.9	850±41	60±3	7.1±1.4
	reverse	15.1	909	71	9.7
	forward	16.8	900	57	8.6
Spiro no add	reverse	14.9±2.7	737±181	20±4	2.3±0.9

Table S3. TRPL lifetimes obtained fitting the data in Figure 2c to a biexponential decay. Perovskite layer was deposited on glass and **FU7** and **TAA14** deposited on top of the perovskite layer.

Sample	τ_1 (ns)	τ_2 (ns)
Perovskite	2.8	20.7
Perovskite+FU7	1.2	7.4
Perovskite+TAA14	0.5	5.0

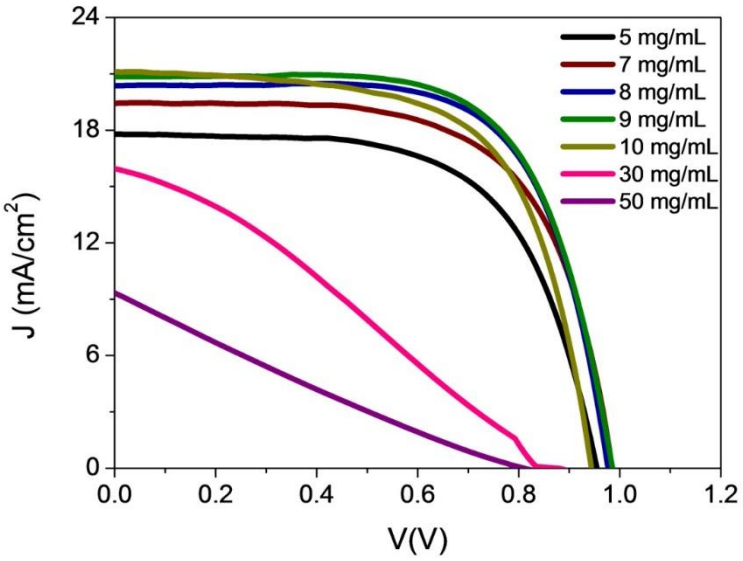

Figure S24. Current potential curves without any preconditioning of champion cells prepared with FU7 additive free as HTM. For the deposition of FU7 different concentrations in chlorobenzene have been used as indicated in the lend. Solar cell parameters are indicated in Table S1. For sake of clarity just forward is plotted.

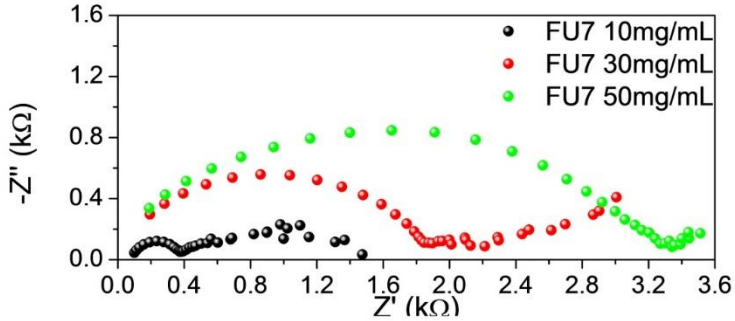

Figure S25. Nyquist plot of PSCs using **FU7** as HTM under 1 sun illumination at 0.4 V DC forward applied bias. Different concentrations have been used for the deposition of the **FU7** film. It can be appreciated a clear increase of the size of the high frequency arc. The high frequency arc is affected by the charge transport at the electron selecting layers, increasing when the transport resistance at the selecting contacts increases.[6, 7] Increase of transport resistance at the selective contacts affects deleteriously cell performance.

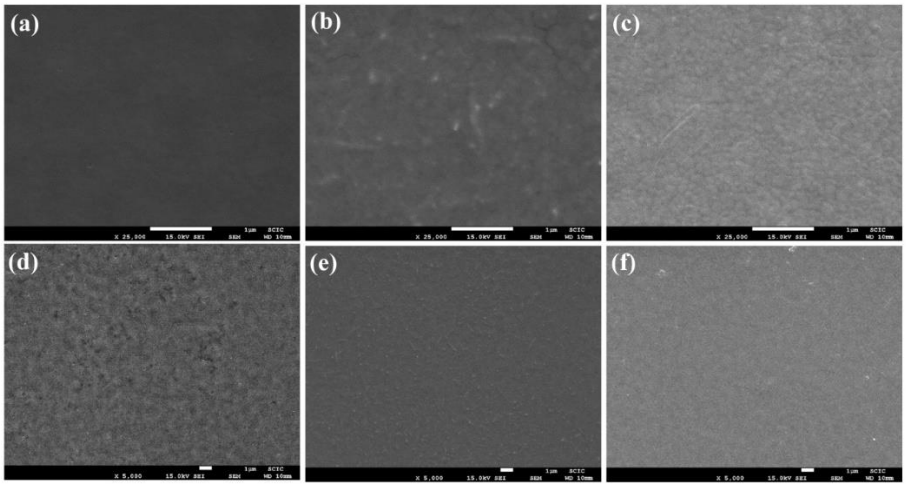

Figure S26. Top view of HTM film deposited on top of perovskite layer using **a**, Spiro-OMeTAD; **b**, FU7 and **c**, TAA. **d**, **e**, and **f** are as **a**, **b**, and **c** respectively but at higher magnification . Scale bar indicates 1 μm.

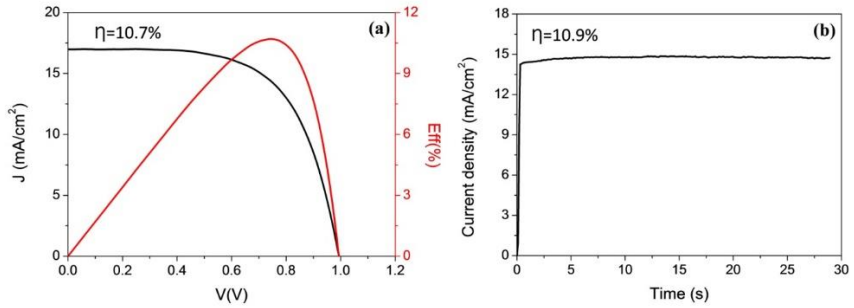

Figure S27. a, reverse scan of cell prepared with **FU7** as HTM an efficiency of 10.7 has been obtained from this curve. The voltage at maximum power, V_{MP}, has been obtained at 0.742 V. **b**, An stabilized efficiency of 10.9% very close, even a little bit higher, to the determined using the reserve scan of the J-V has been determined measuring the stabilized current at V_{MP}.

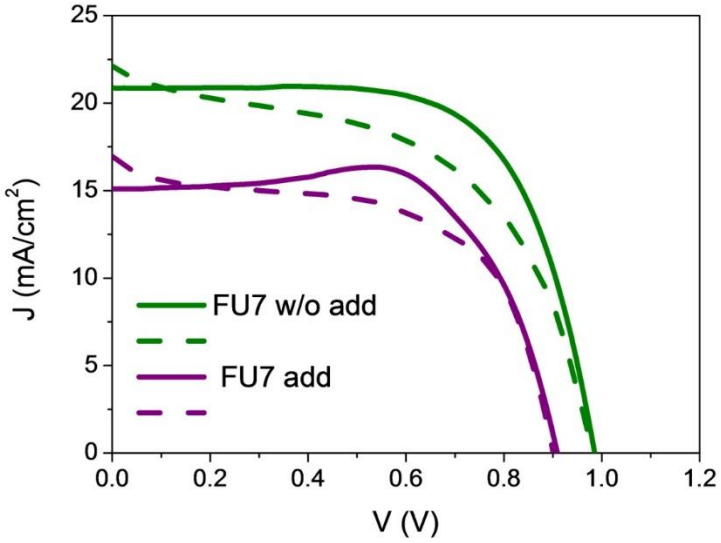

Figure S28. Current potential curves for devices using **FU7** as HTM with and without (w/o) additives (add). Reverse scan is plotted with solid lines while forward scan with dashed lines. The additives employed have been the same ones and with the same concentration that the used with the Spiro-OMeTAD, adding 28.8 μL of TBP and 17.5 μL of a stock solution of 520 mg mL^{-1} of Li-TFSI in 1 ml of chlorobenzene solution with **FU7**.

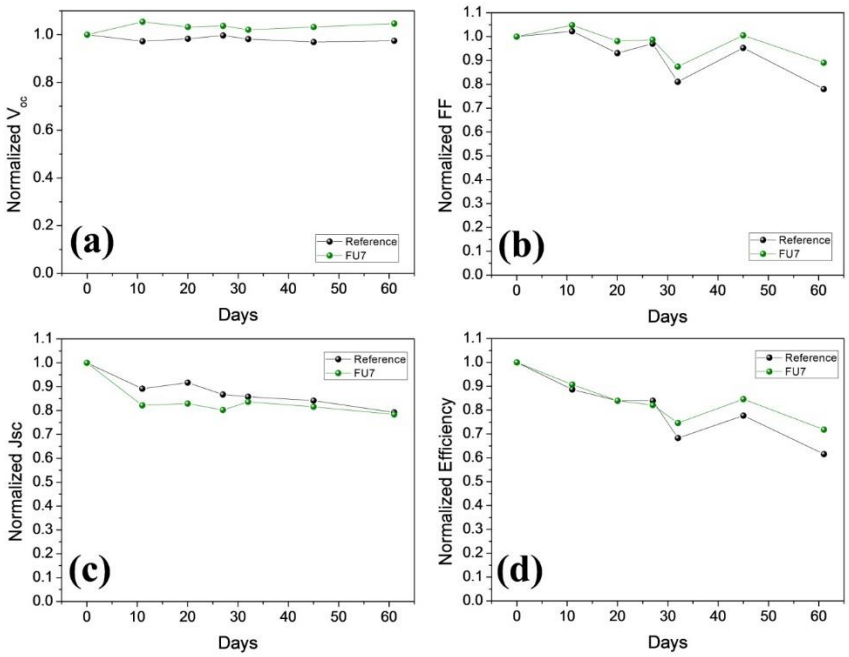

Figure S29. Normalized solar cell obtained from the average of three cells at each condition using as spiro-OMeTAD (reference) and **FU7** as HTM. Solar cells were prepared without any encapsulation and were stored under dark in dry air atmosphere. **a**, photovoltage (V_{oc}); b, fill factor (FF); **c**, photocurrent (J_{sc}), and **d**, efficiency (as in Fig. 2d).

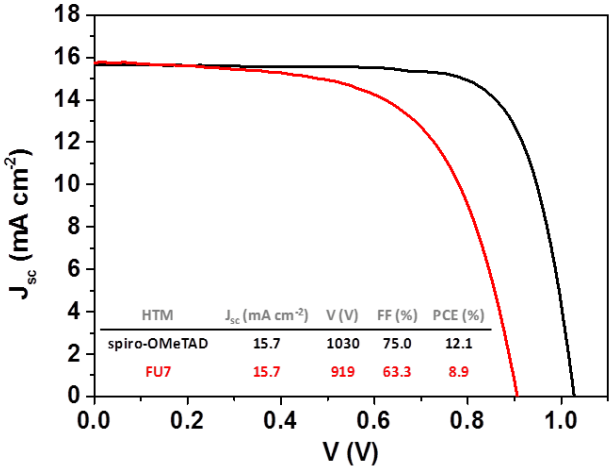

Figure S30. *J-V* curves for solar devices with architecture glass/FTO/C_{60}/$MAPbI_3$:C_{60}/HTM/Au.

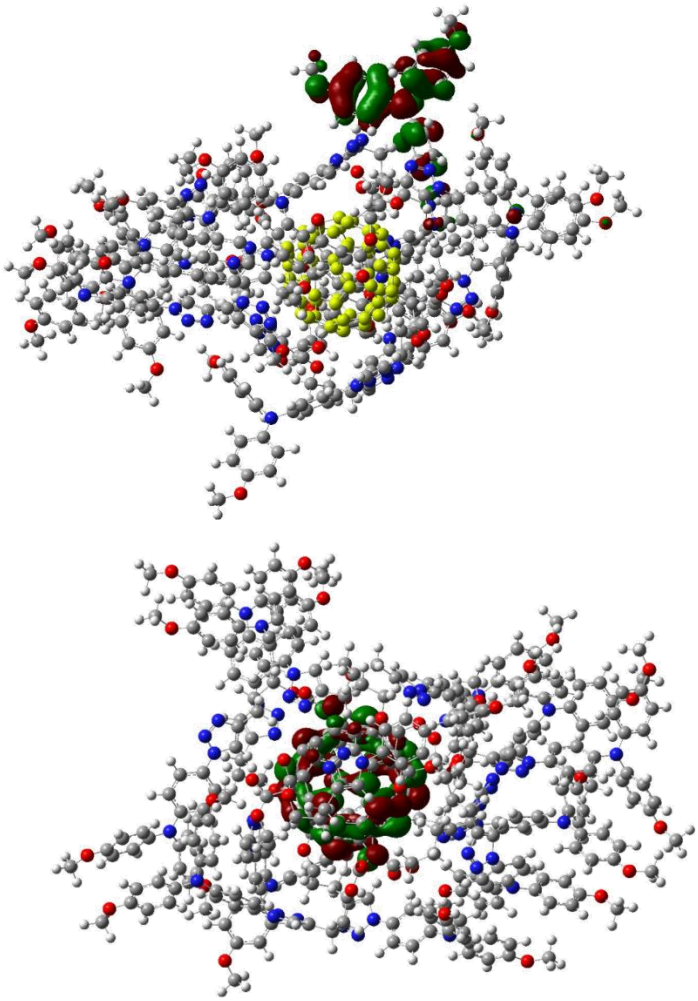

Figure S31. HOMO and LUMO estimated by DFT with the Gaussian 09 suite of programs. Structure optimization was performed in gas phase using the B3LYP functional, and the 3-21G basis set. Note that the HOMO orbital is located in one of the super-triarylamine moieties instead of being delocalized in all the super-triarylamines. This is a consequence of the lack of symmetry in the molecule, which breaks the expected degeneracy of the HOMO in a set of molecular orbitals, very close in energy, corresponding to each super-triarylamine branch. In practice, each of them could be the HOMO, but we have selected this particular one for the sake of clarity in the figure.

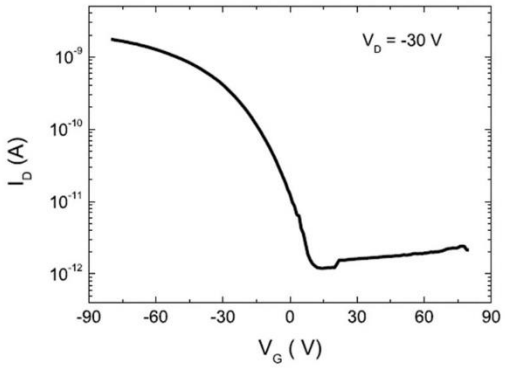

Figure S32. Representative transfer curve of a bottom-gate, bottom-contact field-effect transistor with a **FU7** channel. From the behaviour of the drain current versus the gate voltage, the p-type semiconducting behaviour of the molecular layer can be directly extracted.

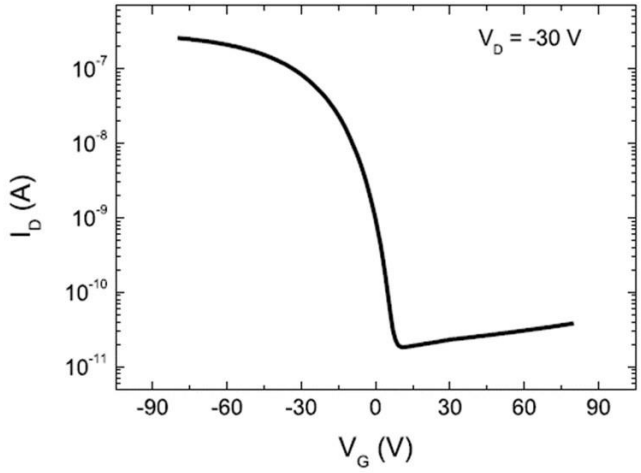

Figure S33. Representative transfer curve of a bottom-gate, bottom-contact field-effect transistor with a Spiro-MeOTAD channel. From the behaviour of the drain current versus the gate voltage, the p-type semiconducting behaviour of the molecular layer can be directly extracted.

Field-effect transistors (non optimized) were fabricated in a bottom-gate, bottom-contact configuration. We used a highly n-doped Silicon wafer with a 150 nm-thick SiO_2 thermally grown insulating layer on top which serves as a gate dielectric. Interdigitated electrodes with a width to length ratio of 1000 were produced by standard optical lithography and lift-off; the contact material was a bilayer of Ti (5nm)/Au (35 nm) which was grown by electron-beam deposition in ultra-high vacuum. Prior to the molecular deposition, the wafers were primed with hexamethyldisilazane (HMDS) for reducing the charge trapping at the molecular/dielectric interface. The molecular layers were spin-coated from solutions in chlorobenzene at a maximum speed of 4000 rpm for 30 seconds. The solutions were produced at nominal concentrations of 72,3 mg/ml for the Spiro-MeOTAD and 9 mg/ml for the **FU7** case. The samples were then transferred to a high-vacuum probe station and the electrical characteristics were measured at room temperature using a programmable semiconductor analyser provided with preamplifiers.

References:

1. C. Lambert, J. Schelter, T. Fiebig, D. Mank and A. Trifonov, *J. Am. Chem. Soc.*, 2005, **127**, 10600-10610.
2. N. G. Connelly and W. E. Geiger, *Chem. Rev.*, 1996, **96**, 877-910.
3. V. V. Pavlishchuk and A. W. Addison, *Inorganica Chimica Acta*, 2000, **298**, 97-102.
4. D. Tsiplakides, D. Archonta and C. G. Vayenas, *Topics in Catalysis*, 2007, **44**, 469-479.
5. C. Aranda, C. Cristobal, L. Shooshtari, C. Li, S. Huettner and A. Guerrero, *Sustainable Energy & Fuels*, 2017, **1**, 540-547.
6. E. J. Juarez-Perez, M. Wuβler, F. Fabregat-Santiago, K. Lakus-Wollny, E. Mankel, T. Mayer, W. Jaegermann and I. Mora-Sero, *J. Chem. Phys. Lett.*, 2014, **5**, 680-685.
7. A. Guerrero, G. Garcia-Belmonte, I. Mora-Sero, J. Bisquert, Y. S. Kang, T. J. Jacobsson, J.-P. Correa-Baena and A. Hagfeldt, *J. Chem. Phys. C*, 2016, **120**, 8023-8032.

Chapter 5. Publication 3

5.1. Flash infrared annealing as a cost-effective and low environmental impact processing method for planar perovskite solar cells

Sánchez, S., Vallés-Pelarda, M., Alberola-Borràs, J. A., Vidal, R., Jerónimo-Rendón, J. J., Saliba, M., Boix, P. P. & Mora-Seró, I. (2019). Flash infrared annealing as a cost-effective and low environmental impact processing method for planar perovskite solar cells. Materials Today, 31, 39-46. https://doi.org/10.1016/j.mattod.2019.04.021

My contribution to the work presented in this chapter has been:

- Preparation of part of the devices by AS method and help with the samples prepared by FIRA method.
- Characterization of the prepared solar cells: J-V curves.
- Characterization of the all devices by Impedance Spectroscopy.

Published manuscript

Flash Infrared Annealing as a Cost-effective and Low Environmental Impact Processing Method for Planar Perovskite Solar Cells

Sandy Sánchez,[1,2†] Marta Vallés-Pelarda,[3†] Jaume-Adrià Alberola-Borràs,[3,4] Rosario Vidal,[4] José J. Jerónimo-Rendón,[1] Michael Saliba,[1*] Pablo P. Boix,[5*] and Iván Mora-Seró[3*]

[1] Adolphe Merkle Institute University of Fribourg Chemin des Verdiers 4, CH-1700 Fribourg, Switzerland.

[2] Laboratory of Photomolecular Science (LSPM) École Polytechnique Fédérale de Lausanne (EPFL), 1015 Lausanne, Switzerland.

[3] Institute of Advanced Materials (INAM), University Jaume I, Avenida de Vicent Sos Baynat, s/n, 12071 Castelló de la Plana, Spain

[4] Department of Mechanical Engineering and Construction, GID, Universitat Jaume I, Av. Sos Baynat s/n, 12071 Castelló de la Plana, Spain

[5] Instituto de Ciencia Molecular (ICMol), Universitat de València, Catedrático José Beltrán, 2, 46980 Paterna, Spain

† Same contribution.

* Corresponding author: miliba@gmail.com, pablo.p.boix@uv.es, sero@uji.es

Data Availability: Data will be available on request.

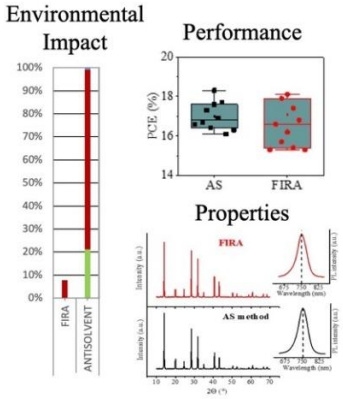

Abstract

For successful commercialization of perovskite solar cells, straightforward solutions in terms of environmental impact and economic feasibility are still required. Flash Infrared Annealing (FIRA) is a rapid method to fabricate perovskite solar cells with efficiencies > 18% on simple, planar architectures which allows a film synthesis in only 1.2 seconds, faster than the previous report based in a meso architecture and all of them without the usage of antisolvent. In this work, through a comparative study with the common lab-scale method, the so-called antisolvent (AS), the main photovoltaic parameters and working mechanisms obtained from impedance spectroscopy (IS) measurements show similar devices features as for FIRA. However, from the life cycle assessment (LCA) comparison study, the FIRA method has only 8% of the environmental impact and 2% of the fabrication cost of the perovskite active layer with respect to the AS for the perovskite film synthesis. These results denote that FIRA is a low-impact, cost-effective fabrication approach which can be directly adapted to perovskite planar configuration that is compatible with industrial up-scaling.

Introduction

Perovskite solar cells (PSCs) have made impressive improvements in one decade with lab-scale efficiencies of 23.7%,[1, 2] comparable to other well-established solar cells materials. Consequently, the commercialization of PSCs is now a high-priority topic involving many research groups and companies worldwide.[3-5] This includes industrial up-scaling which is a complex task, especially for such a recent technology that still faces challenges in terms of long term stability, large-area deposition methods, reproducibility, low cost and low environmental impact. Thus, a commercially successful fabrication technique should avoid treatments that are incompatible with large area fabrication processes. In addition, considerations on the environmental impact associated to the fabrication steps, as well as their energy consumption and materials employed, are key to achieve a viable industrial fabrication process.[6-9]

In this work we show that recently reported Flash Infrared Annealing (FIRA) is an easily scalable crystallization method for perovskite thin films without the need of a mesoporous, high-temperature scaffold. Through FIRA and using the planar architecture we are able to reduce the synthesis time of the perovskite film until 1.2 s, which represent 29% less respect to the synthesis time needed for the mesoporous TiO_2 electrode (1.7 seconds), as previously reported by first time.[10] The lower synthesis time of the perovskite film is significant in terms of cost reduction of the manufacturing process. To date, the most efficient lab-scale PSCs fabrication procedure is the antisolvent (AS) method[11] where an antisolvent, typically

chlorobenzene, is added suddenly to a perovskite precursor, typically dissolved in DMF or DMSO, inducing a supersaturation that triggers the perovskite nucleation process. Frequently a relatively long annealing process of up to 1 h is required for the final crystallization. This method is challenging to up-scale.[12] In addition, AS is difficult to implement for large areas and requires an extra solvent and a long thermal annealing step affecting not just the cost but the environmental impact.[13] In contrast, FIRA uses a short IR flash in the range of seconds allowing for the fast nucleation and crystal growth of the perovskite film from the precursor solution. It is compatible with large area deposition techniques such as slot dye or roll-to-roll processing. Consequently, FIRA is proposed as a feasible low cost and rapid thermal process for the production of perovskite thin films and corresponding devices.[10, 14]

Rapid thermal annealing is commonly used for semiconductors, e.g. silicon solar cells,[8, 15, 16] to grow pure crystal phases without losing material quality, e.g. pure monocrystalline silicon. Large open-circuit voltage, V_{oc}, improvements were achieved by the removal of defects and dopant activation.[15] Silicon solar cells with efficiencies of 17.1 % were reported with rapid thermal processing in conjunction with surface passivation.[17] Similarly, the degradation of multicrystalline silicon solar cells can be reduced by 80% using a 10 second annealing treatment at 200 °C with a high intensity irradiation of 44.8 kW m^{-1}.[16] In PSCs, rapid thermal process synthesis provides a cost-effective route to improve key structural properties in perovskite films.[18-21]

For an exhaustive determination of environmental impacts, a life cycle assessment (LCA) methodology is commonly employed. In recent years, a significant number of LCA studies are performed in order to analyze PSCs for sustainable commercialization. Most of the studies are focused on the configuration of PSCs produced in the laboratories.[13, 22-26] In general, these results criticize PSCs' lead content as a significant risk for the environment. However, the energy consumption emerges as the most demanding disadvantage during production and consequently is one of the most important thresholds to optimize the up-scaling process.

Here, we analyze the potential of FIRA related to industrially-friendly process for PSCs. We compare the PSCs performance of FIRA and AS analyzing the cost of production and the environmental impact by LCA of both methods. We propose an extrapolation of the FIRA process to fabricate triple cation perovskite (methylammonium (MA)- formamidinium (FA)-Cs) films reporting for the first time a planar architecture. Planar PSCs are more attractive for industrial implementation than devices with mesoporous architecture as they present lower cost and environmental impacts.[22] Despite the multication perovskite increasing the cost compared to simpler, single-cation perovskites,[13] the higher stability reported for multication perovskites can compensate the cost increase.[27-32]

We show that FIRA results in compact perovskite films on FTO/TiO_2 simplifying the system complexity in view of potential industrial viability. These devices achieve a highly reproducible

power conversion efficiency (PCE) of more than 18%, comparable to devices fabricated by AS. Optoelectrical characterization of films and devices by impedance spectroscopy unveils identical patters governing AS and FIRA solar cells, which suggests similar working principles. This was achieved with a modified FIRA setup that can quickly heat up the perovskite solution as compared to previous works with mesoporous architecture.[10, 14] In the specific design developed for planar samples, the IR emitter can increase the temperature in the chamber up to 1000°C in a few seconds and the cooling integrated system dissipates the heat quickly, thus enabling control on the crystallization kinetics of the thin film without thermal degradation. On the way of PSCs to commercialization, there are few examples of LCA studies, where the perovskite was deposited by processes suitable for industrial scale.[33, 34] As far as we know this is the first work reporting the LCA of high-temperature short-time annealing for PSCs preparation reporting a significant advantage with respect to commonly used lab techniques with an enormous potential for up-scaling.

1. Mixed cation perovskite thin-film analysis

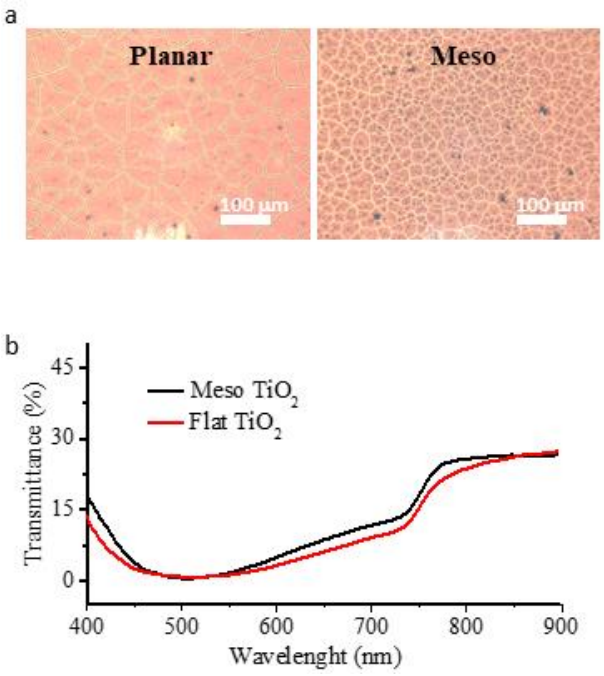

Figure 1. Perovskite films fabricated by FIRA on top of planar and meso architectures: a) Optical microscope images taken in transmittance mode and, b) the respective transmittance spectra.

Planar configuration has significant advantages from the up-scaling point of view in terms of low cost and low environmental impact when compared to architectures with a mesoporous TiO_2 layer.[22] Here, we show that the FIRA method can grow a planar smooth and compact perovskite layer. The optical microscope images shown in Figure 1a unveil larger crystal domains for the planar compared to the mesoporous architecture. The rapid crystal growth across the substrate can avoid that the solution dewets on the planar substrate. Figure 1b shows the transmittance spectra for the two samples depicted in Figure 1a, where the planar configuration has lower

transmittance than the meso case. This may be due to the greater effective optical absorption or the smaller light scattering of the perovskite film grown on a flat electrode. The characteristic FIRA grain domain has typically a large microstructure composed by highly oriented single grain-particles, as previously reported,[10] see SEM pictures in Figure 2a. This microstructure is formed through nucleation centers surrounded by ordered rings of single grains of 5 to 30 µm (as shown in Figure S1 for planar electrodes). This thin film microstructure can play an important role in the final device performance.[35, 36]

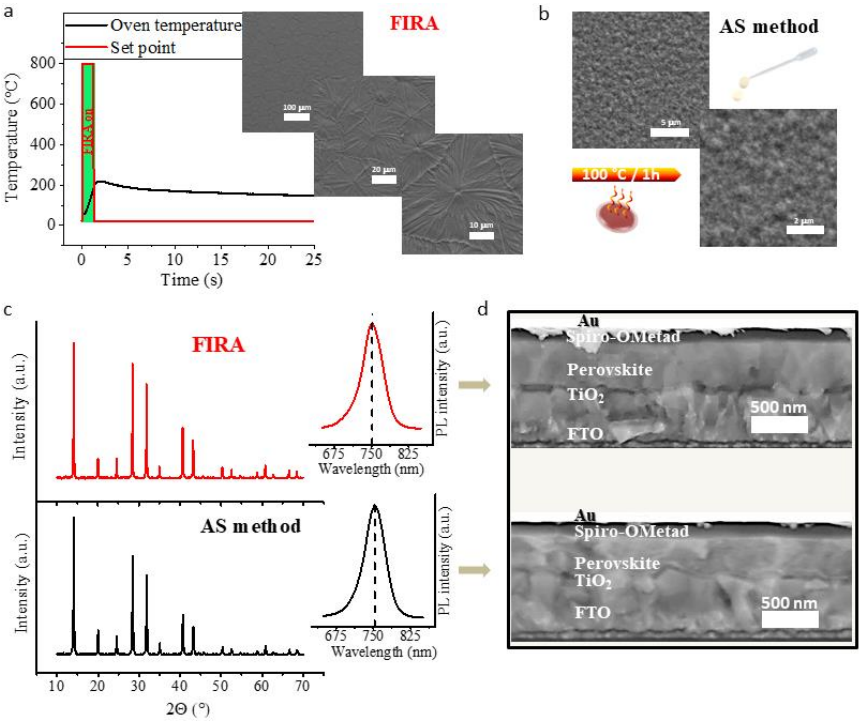

Figure 2. a) Temperature profile of FIRA annealed films with respective SEM top view. b) SEM top view image of the antisolvent annealed films and a schematic inserted to illustrate the AS method.

c) XRD pattern (left) and photoluminescence spectra (right) of the FIRA and AS perovskite films. d) Cross sectional images of the devices with FIRA and AS perovskite films.

To assess planar FIRA perovskite films, we compare them to state-of-the-art AS perovskite films. Figure 2**a** and **b** shows SEM top view images for FIRA and AS. Indeed, FIRA films have large domains of 40 μm. From Figure 2b**,** we observe that the AS films have a typical grain size of 200 nm.[37-39] In addition, Figure 2a shows the temperature profile for the FIRA annealed film for the first 1.2 seconds, the temperature collected corresponds to the chamber (not directly to the film surface). Within this time, FIRA produces the crystallization of perovskite film, see Figure 2c. The sample is kept in the chamber for 20 seconds to completely remove remaining solvents, reducing significantly the annealing time for AS that requires up to an hour, see Figure 2b. Despite the morphological differences, FIRA and AS perovskite films present similar structural and optical characteristics in terms of XRD and PL characterization, see Figure 2c. The diffraction pattern shows highly crystalline films with the tetragonal phase at room temperature which correspond to the mixed cations compounds with large amount of FA (83%), which is stabilized by the addition of smaller cations such as MABr (17%) and CsI (5%), as previously reported.[27, 40] The PL emission spectra correspond to the band gap of the MAFACsPbIBr compound of about 1.6 eV and show in this case similar intensities and peak width.[41-44] Figure 2d shows a cross sectional image of the manufactured devices comparing FIRA and AS. Both cases show the formation of pinhole-free and compact films.

2. PV performance and electronic characteristic of the devices

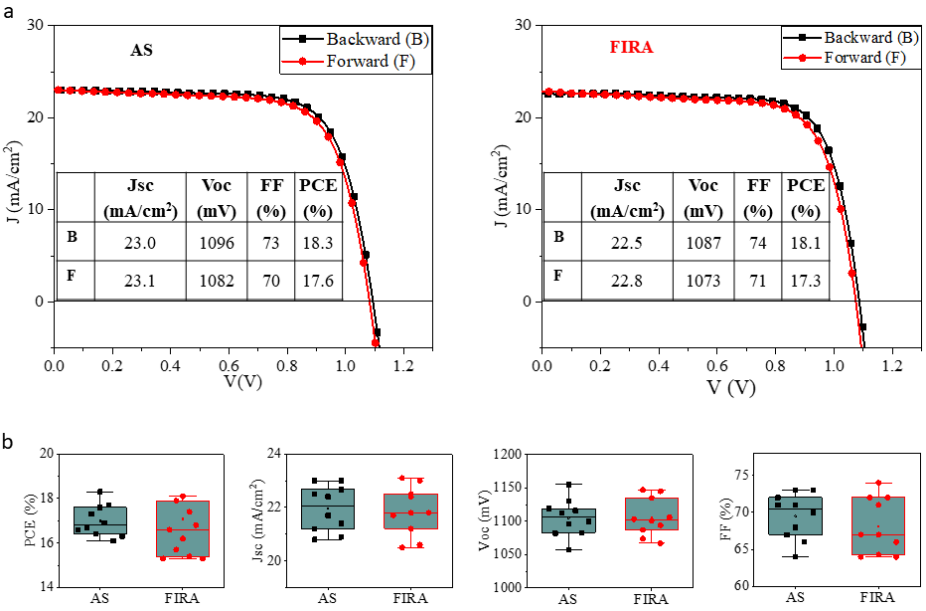

Figure 3. a) Forward and backward JV scan of the champion devices made by FIRA and AS. The scan rate was 10mV/s with an aperture area of 0.09 cm^2. b) Statistic of the PV parameters for 10 devices made by FIRA and AS.

The regular architecture stack was used with FTO/TiO_2/MAFACsPbIBr/Spiro-OMetad/Au layers, as shown the SEM cross-sectional image of Figure 2d. The JV characteristic of the champion devices, Figure 3a, shows similar PV parameters for both studied methods, achieving a PCE of more than 18%. The forward scan displays little hysteresis,[45-47] and has PCEs >17%. The high performance of these PSCs may also contribute to a decreased hysteresis.[48] In addition, samples prepared by FIRA and AS exhibit similar long-term stability, see Figure S2. It is also worth to highlight

that FIRA samples with higher area of 1.4 cm^2, preserve the photocurrent and the photovoltage, see Figure S3. Their efficiency is just reduced a 14% respect the performance of the low area devices, compare high area devices in Figure S3 with low area devices in Figure 3. The main limitation of the efficiency high area devices, see Figure S3, is due to the decrease in FF, which can be attributed to the increase in series resistance in the larger area device. Further device engineering will reduce this upscaling limitation. Figure 3b compares FIRA and AS devices presenting statistics of the main PV parameters. Here the standard deviation demonstrates a good reproducibility for both methods. Note that the data points are more spaced for FIRA than AS, as the median values are a bit lower in the FIRA case. FIRA samples, however, present slightly higher FF dispersion as compared to samples fabricated by the antisolvent method. This dispersion cannot be attributed to series resistance differences, as similar values of ~10 $\Omega \cdot cm^2$, considering the experimental error, were obtained by impedance spectroscopy. We attribute the higher dispersion of FIRA samples to the synthesis in ambient conditions instead of the glovebox fabrication, as in the antisolvent samples. We point out that all the FIRA processing was carried out in a standard fume hood, with relative humidity of ~30-40%. Thus, the film formation can be improved even further by standardizing the atmospheric conditions.[46]

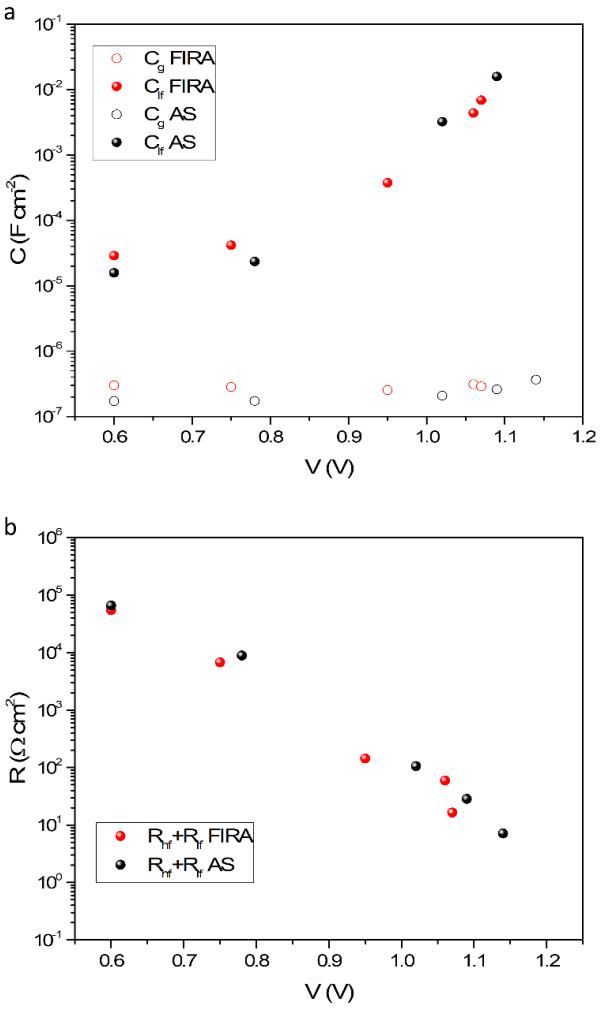

Figure 4. a) Capacitive and b) resistive parameters of FIRA and AS based perovskite solar cells measured under different light intensities at open circuit. The parameters are extracted from the fitting to the equivalent circuit discussed in the supporting information.

Further insights on the device working mechanisms can be obtained by means of impedance spectroscopy. The devices were measured under different light intensities at V_{oc} in order to evaluate charge recombination and charge storage behavior. The obtained Nyquist plot, with two distinguishable features at high and low frequency, were adjusted to a simplified equivalent circuit, (Figure S4) as previously reported.[49, 50] Although an in-depth model for PSCs is still under development, the results enable interesting observations regarding the operation mechanisms. On the first place, the high frequency capacitance, which is associated to the perovskite geometric capacitance (C_g),[49] shows similar values for both FIRA and AS devices, see Figure 4a. These values are in good agreement with previous reports indicating a dielectric constant of ε_r ~35 regardless of the fabrication method. Similar low frequency capacitance (C_{lf}),[51] with different interpretations in the literature but mostly pointing to an origin linked with ionic motion,[52-55] suggests that both analyzed methods result in similar features in terms of ionic effect, see Figure 4a. This observation is particularly interesting for the studied cases, as the grain size of the samples present clear differences. As a result of the similar charge distribution of the perovskites, the recombination behavior of the analyzed samples does not present significant disparities. In particular, an estimation of the charge recombination process can be extracted from the series addition of the resistances in both high and low frequency features,[50, 56] displayed in Figure 4b. The individual resistive components (R_{hf} for the high frequency feature and R_{lf} for the low frequency feature) are displayed in the supporting information, Figure S5. These results

highlight the fact that PSCs can present high performance with different apparent morphologies (i.e. high efficiency has been reported for PSCs based on evaporation with small grain size[57]). Consequently, morphology can have an effect in the final optoelectrical properties of the perovskite films, yet it is not the main factor determining the final photovoltaic performance of the device

3. Life cycle assessment of the perovskite film synthesis methods

Finally, we have conducted an LCA to determine the potentiality of both processes for up-scalability. We have considered that both devices can preserve the same efficiencies on larger substrates, although this will be more difficult for AS samples.[12] Further considerations about the assumptions and methodology adopted for LCA can be found in the Materials and Methods section. Different impact categories have been analyzed for both kind of samples, see Table 1 where abbreviations and units are also included. One of the most significant impact categories to measure the environmental performance of a solar energy collector device is the carbon footprint, as one of the main benefits from solar energy stemming is a reduced greenhouse effect. Photochemical oxidation and acidification are also selected to have a broad panoply.

Energy is a fundamental aspect of perovskite modules as it is their only valuable output. Knowing the necessary production energy is a good practice to calculate how viable their production is. The cumulative energy demand method V1.09 (CED)[58] obtains the total cradle-to-gate energy invested in the production of the perovskite

module. Externalities need to be included as well for a holistic assessment. Thus, the potential toxicity of the production and emission of chlorobenzene and nitrogen was performed with USEtox V1.04 method,[59] including the impact categories Human toxicity (cancer), Human toxicity (non-cancer) and Freshwater ecotoxicity, see Table 1. CML, CED and USEtox methods are incorporated within the SimaPro® 8.0.3.14 software.[60]

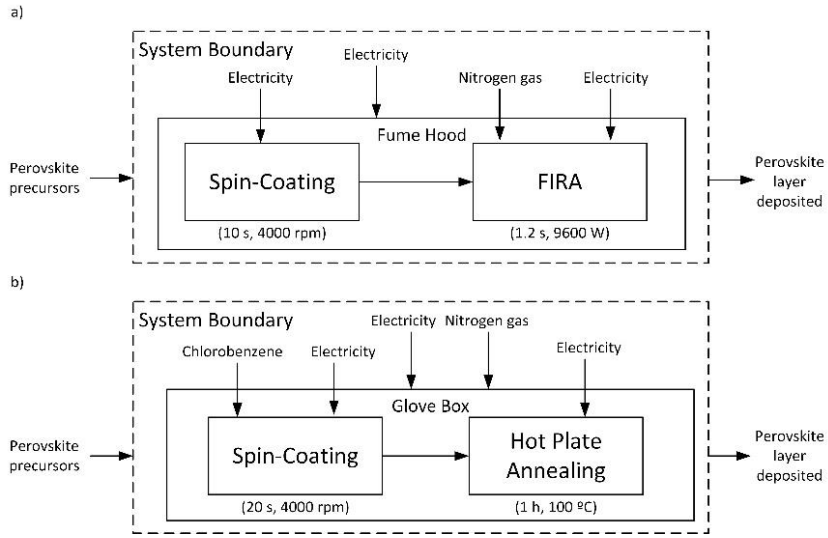

Figure 5. System boundaries for the perovskite layer deposition considering only the process that are different. a) FIRA method. b) Antisolvent method.

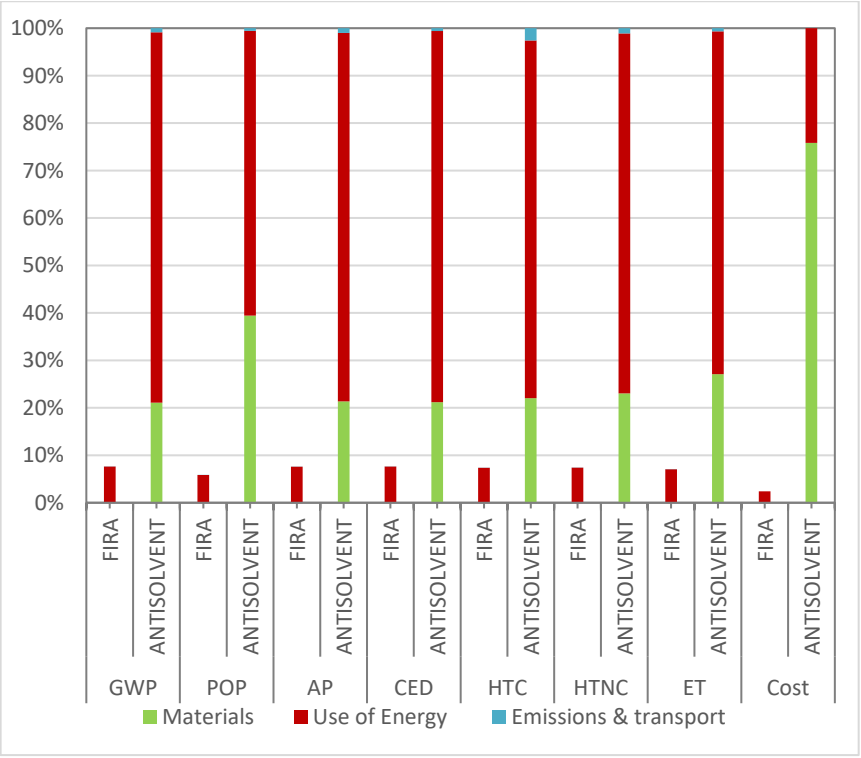

Figure 6. Relative costs and environmental impacts of the different process of the FIRA and antisolvent methods for perovskite layer deposition. Abbreviation of each impact category are explained in Table 1.

Table 1. List of impact categories, their abbreviations, units and methodologies in which they are included

Category	Abbreviation	Unit	Methodology
Climate change	GWP	kg CO_2 eq	CML baseline V3.02[61]
Photochemical oxidation	POP	kg C_2H_4 eq	
Acidification	AP	kg SO_2 eq	
Cumulative energy demand	CED	MJ	Cumulative energy demand V1.09[58]
Human toxicity, cancer effects	HTC	CTUh	Usetox V1.04[59]
Human toxicity, non-cancer effects	HTNC	CTUh	
Freshwater ecotoxicity	ET	CTUe	

The environmental impacts and the cost are relativized with respect to the corresponding highest value for the two methods, FIRA and AS, using the same functional unit (1kWh). In this way, the results are independent of the solar cell lifetime. Life cycle inventories for 1 kWh are summarized in Table S1. AS method presents the highest environmental impacts in each of the categories considered and also the highest cost, for the system boundaries of Figure 5, hence the value of 100 % is assigned in Figure 6 and the values for the FIRA method are relative to the values of the AS method. Absolute values can be found in Table S2. Environmental impacts are disaggregated in the impacts produced by materials acquisition, energy consumption during the processing and emissions and transport. Costs are broken-down in materials and energy.

The environmental impacts of the AS method are mainly incurred by the energy consumption during the annealing, an often-disregarded

factor. The substitution of the long AS annealing by the fast FIRA process implies significantly lower electricity consumption and also the elimination of chlorobenzene consumption that also have adverse contributions. The environmental impacts of the FIRA method are less than 8% compared to AS in all analyzed categories in Figure 4. Annealing was also identified to have one of the highest environmental impacts in the LCA of a pre-industrial process based on a carbon stack architecture.[34] Moreover the advantages of FIRA method in comparison with AS are not just in terms of impact but in terms of cost. The materials prices have a significate influence (76%) in the cost of the antisolvent method. The reduction in nitrogen consumption, the absence of chlorobenzene and the lower energy consumption in the FIRA method means that the cost with this methodology is only 2% of the AS method.

4. Conclusions

We show that it is possible to fabricate planar perovskite solar cells using FIRA, that is compatible with up-scaling compared to the commonly used mesoporous configuration. Considering the PV performance and the impedance spectroscopy analysis, it can be concluded that the FIRA method can produce PSCs with similar efficiency than the commonly reported antisolvent methods. FIRA and AS present different morphology but similar optoelectronic performance in terms of PL and impedance spectroscopy, a fact that points to similar working principles in both devices. Finally, FIRA does not need an additional solvent, and the amount of energy is significantly reduced due to the much shorter annealing time of seconds instead of up to an hour. As a result, a systematic life cycle

assessment has allowed us to determine that the cost and environmental impacts are decreased one order of magnitude comparing FIRA with AS. With the assumptions of the present work, the impacts caused by different processes reveal that FIRA exhibits only 8% of the impact of AS samples, for all the impacts categories analyzed, while the cost is just 2%. This work highlights the potential of FIRA for up-scaling towards eventual commercialization.

Materials and methods

Device manufacturing

Photovoltaic devices were fabricated on FTO coated glass (Pilkington NSG TEC™). The substrates were cleaned with Hellmanex soap, followed by 30 min sonication in a Hellmanex 2% water solution, 15 min sonication in IPA, and 5 min of oxygen plasma etching. Then, 30 nm thick TiO_2 compact layers were deposited onto the FTO by spray pyrolysis at 450 °C from a precursor solution of titanium diisopropoxide bis (acetylacetonate) in anhydrous ethanol and acetylacetone. After spraying, the FTO substrates were left at 450 °C for 5 min before cooling to room temperature. Then, a mesoporous TiO_2 layer was deposited by spin-coating for 10 s at 4000 rpm with a ramp of 2000 rpm s^{-1}, using a 30-nm particle size TiO_2 paste (Dyesol 30 NR-D) diluted in ethanol to achieve 150-200 nm thick mesoporous layers. After spin-coating, the FTO substrates were dried at 100 °C for 10 min, and the films were annealed on a programmable hotplate (2000 W, Harry Gestigkeit GmbH) to crystallize TiO_2 at 450 °C for 30 min under dry air flow.

The hybrid perovskite precursor solutions were deposited from a precursor solution containing CH_5N_2I (1 M), PbI_2 (1.1 M), CH_3NH_3Br (0.2 M) and $PbBr_2$ (0.2 M) in anhydrous DMF: DMSO 2:1 (v:v). Note that this composition contains a lead excess as reported elsewhere[27]. Then CsI, dissolved as a 1.5 M stock solution in DMSO, was added to the mixed perovskite precursor to achieve the desired triple cation composition.

For antisolvent method the perovskite films were deposited as previously reported[47, 62]. The perovskite solution was spin-coated in two steps at 1000 and 6000 rpm for 10 and 20 s, respectively. During the second step, 100 µL of chlorobenzene was poured onto the spinning substrate, 5 s before the end of the program. The substrates were then annealed at 100 °C for 1 h in a nitrogen-filled glovebox. After perovskite annealing, the substrates were cooled down within a few minutes.

The films made by FIRA method include the spin-coating of the perovskite solution in a single step at 4000 rpm for 10 s. The substrates were then IR irradiated for 1.2 s in the FIRA oven and were kept there for 20 additional seconds before removal and cooling within several minutes. FIRA processing was carried out in a standard fume hood. Immediately after cooling the perovskite films, a spiro-OMeTAD (Merck) solution (70×10^{-3} M in chlorobenzene) was deposited by spin-coating at 4000 rpm for 20 s. Spiro-OMeTAD was doped with Li-TFSI (Sigma Aldrich), tris(2-(1H-pyrazol-1-yl)-4-*tert*-butylpyridine)-cobalt(III) tris(bis(trifluoromethylsulfonyl)imide) (FK209, Dynamo), and 4-

tert-butylpyridine (TBP, Sigma-Aldrich). The molar ratios of the additives to spiro-OMeTAD were: 0.5, 0.03, and 3.3 for Li-TFSI, FK209, and TBP, respectively.

Material and Device Characterization

Scanning electron microscopy and energy dispersive x-ray spectroscopy were carried out on a Tescan MIRA 3 LMH with a field emission source operated at an acceleration voltage of 10 kV using an octane-pro EDS detector. Powder X-ray diffraction was performed in transmission geometry with Cu target (λ = 1.5401Å) using an STOE STADI P diffractometer. Optical transmission measurements were performed using a Zeiss Axio-Scope A1 Pol using a Zeiss EC Epiplan-Apochromat 20× objective and a xenon light source (Ocean Optics HPX-2000). For spectroscopic measurements, an optical fibre (QP230-2-XSR, 230 µm core) collected the light reflected from the sample. The spectra were recorded by a spectrometer (Ocean Optics Maya2000 Pro), and a standard white diffuser was used as reference. Photoluminescence spectra were obtained with Fluorolog 322 (Horiba Jobin Ybon Ltd) with the range of wavelength from 620 nm to 850 nm by exciting at 460 nm. The samples were mounted at 60° and the emission recorded at 90° from the incident beam path.

The temperature in the FIRA chamber was measured using a K-type thermocouple and the surface temperature of the FTO was measured by a wire J-type thermocouple, both connected to an Analog Devices *AD595* amplifier interfaced with Labview software. Impedance

Spectroscopy measurements were performed using a PGSTAT-30 Autolab potentiostat and a Xe lamp.[63] The light intensity was controlled using different neutral density filters.

Life Cycle Assessment

A comparative life cycle assessment (LCA) is performed focused on the deposition layer of perovskite for both antisolvent and FIRA methods. 1 kWh of energy is assumed to be produced by each one of these two methods. This kWh of electricity was simulated to be produced assuming the current power conversion efficiency values and the fill factors of each device,[10] the Direct Normal Irradiance in Fribourg (1275 $kW \cdot m^{-2} \cdot year^{-1}$)[64] and considering 400 h of work.[65] The size of the substrate is 5 x 5 cm.

The system boundaries for the comparative LCA are shown in Figure 5, where just the processes that are different AS are considered. Therefore, the common processes for the FIRA and the AS methods are not considered. Energy and nitrogen consumption in the FIRA process are experimentally measured. Energy consumption for spin-coating and hot plate annealing were obtained in a previous study.[13] Nitrogen gas and electricity consumption in the glove box are obtained from its technical specifications, considering the maximum nitrogen leak rate (PureLab HE 2GB). Electricity consumption in the fume hood is for a standard exhaust blower (1/3 hp). The same amount of perovskite precursors for the two methods is estimated and they are not included in the LCA. The detailed inventory is included in the Supplementary material. Materials and electricity are

modelled with the Ecoinvent 3.3 database using processes for Europe.

Costs for the two methods considered are obtained from their life cycle inventories for the system boundaries of Figure 5. Electricity price of 0.112 €/kWh is the EU-28 weighted average price using national data for the quantity of consumption by non-household consumers.[66] The materials prices are obtained from the suppliers and include transport costs.

Acknowledgements

S.S., J.J.J., and M.S. acknowledge the Adolphe Merkle and the Swiss National Science Foundation (Program NRP70 No. 153990). M.V.-P. and I.M.-S. acknowledge the support of the European Research Council (ERC) via Consolidator Grant (724424 - No-LIMIT). M.V.-P. also acknowledges Universitat Jaume I for the support through FPI Fellowship Program (PREDOC/2017/40).

References

1. D. Yang, R. Yang, K. Wang, C. Wu, X. Zhu, J. Feng, X. Ren, G. Fang, S. Priya and S. Liu, *Nature Communications*, 2018, **9**, 3239.
2. N. J. Jeon, H. Na, E. H. Jung, T.-Y. Yang, Y. G. Lee, G. Kim, H.-W. Shin, S. Il Seok, J. Lee and J. Seo, *Nature Energy*, 2018, **3**, 682-689.
3. W. Chen, Y. Wu, Y. Yue, J. Liu, W. Zhang, X. Yang, H. Chen, E. Bi, I. Ashraful, M. Grätzel and L. Han, *Science*, 2015, **350**, 944-948.
4. K. Hwang, Y.-S. Jung, Y.-J. Heo, F. H. Scholes, S. E. Watkins, J. Subbiah, D. J. Jones, D.-Y. Kim and D. Vak, *Advanced Materials*, 2015, **27**, 1241-1247.
5. Y.-S. Jung, K. Hwang, Y.-J. Heo, J.-E. Kim, D. Vak and D.-Y. Kim, *Advanced Optical Materials*, 2018, **6**, 1701182.
6. A. G. Aberle, *Thin Solid Films*, 2009, **517**, 4706-4710.
7. M. Hörteis and S. W. Glunz, *Progress in Photovoltaics: Research and Applications*, 2008, **16**, 555-560.
8. N. Kazuo, A. Michio and W. Naozo, *Japanese Journal of Applied Physics*, 1980, **19**, L563.
9. A. Rohatgi, Z. Chen, P. Doshi, T. Pham and D. Ruby, *Applied Physics Letters*, 1994, **65**, 2087-2089.
10. S. Sanchez, X. Hua, N. Phung, U. Steiner and A. Abate, *Advanced Energy Materials*, 2018, **8**, 1702915-n/a.
11. N. J. Jeon, J. H. Noh, Y. C. Kim, W. S. Yang, S. Ryu and S. I. Seok, *Nat Mater*, 2014, **13**, 897-903.
12. Y. Jiang, M. R. Leyden, L. Qiu, S. Wang, L. K. Ono, Z. Wu, E. J. Juarez-Perez and Y. Qi, *Advanced Functional Materials*, 2018, **28**, 1703835.
13. J.-A. Alberola-Borràs, R. Vidal and I. Mora-Seró, *Sustainable Energy & Fuels*, 2018, **2**, 1600-1609.
14. S. Sanchez, N. Christoph, B. Grobety, N. Phung, U. Steiner, M. Saliba and A. Abate, *Advanced Energy Materials*, 2018, **8**, 1802060.
15. M. L. Terry, A. Straub, D. Inns, D. Song and A. G. Aberle, *Applied Physics Letters*, 2005, **86**, 172108.
16. D. N. R. Payne, C. E. Chan, B. J. Hallam, B. Hoex, M. D. Abbott, S. R. Wenham and D. M. Bagnall, *Solar Energy Materials and Solar Cells*, 2016, **158, Part 1**, 102-106.
17. P. Doshi, A. Rohatgi, M. Ropp, Z. Chen, D. Ruby and D. L. Meier, 1994.

18. J. Xu, Z. Hu, X. Jia, L. Huang, X. Huang, L. Wang, P. Wang, H. Zhang, J. Zhang, J. Zhang and Y. Zhu, *Organic Electronics*, 2016, **34**, 84-90.
19. J. Troughton, C. Charbonneau, M. J. Carnie, M. L. Davies, D. A. Worsley and T. M. Watson, *Journal of Materials Chemistry A*, 2015, **3**, 9123-9127.
20. J. Troughton, M. J. Carnie, M. L. Davies, C. Charbonneau, E. H. Jewell, D. A. Worsley and T. M. Watson, *Journal of Materials Chemistry A*, 2016, **4**, 3471-3476.
21. J. Ye, H. Zheng, L. Zhu, X. Zhang, L. Jiang, W. Chen, G. Liu, X. Pan and S. Dai, *Solar Energy Materials and Solar Cells*, 2017, **160**, 60-66.
22. J.-A. Alberola-Borràs, R. Vidal, E. J. Juárez-Pérez, E. Mas-Marzá, A. Guerrero and I. Mora-Seró, *Solar Energy Materials and Solar Cells*, 2017, DOI: https://doi.org/10.1016/j.solmat.2017.11.008.
23. L. Serrano-Lujan, N. Espinosa, T. T. Larsen-Olsen, J. Abad, A. Urbina and F. C. Krebs, *Advanced Energy Materials*, 2015, **5**, 1501119-n/a.
24. N. Espinosa, L. Serrano-Luján, A. Urbina and F. C. Krebs, *Solar Energy Materials and Solar Cells*, 2015, **137**, 303-310.
25. J. Gong, S. B. Darling and F. You, *Energy & Environmental Science*, 2015, **8**, 1953-1968.
26. J. Zhang, X. Gao, Y. Deng, B. Li and C. Yuan, *ChemSusChem*, 2015, **8**, 3882-3891.
27. M. Saliba, T. Matsui, J.-Y. Seo, K. Domanski, J.-P. Correa-Baena, M. K. Nazeeruddin, S. M. Zakeeruddin, W. Tress, A. Abate, A. Hagfeldt and M. Gratzel, *Energy & Environmental Science*, 2016, **9**, 1989-1997.
28. S. Kim, S. Bae, S.-W. Lee, K. Cho, K. D. Lee, H. Kim, S. Park, G. Kwon, S.-W. Ahn, H.-M. Lee, Y. Kang, H.-S. Lee and D. Kim, *Scientific Reports*, 2017, **7**, 1200.
29. C. Quarti, E. Mosconi, J. M. Ball, V. D'Innocenzo, C. Tao, S. Pathak, H. J. Snaith, A. Petrozza and F. De Angelis, *Energy & Environmental Science*, 2016, **9**, 155-163.
30. G. Abdelmageed, C. Mackeen, K. Hellier, L. Jewell, L. Seymour, M. Tingwald, F. Bridges, J. Z. Zhang and S. Carter, *Solar Energy Materials and Solar Cells*, 2018, **174**, 566-571.
31. T. A. Berhe, W.-N. Su, C.-H. Chen, C.-J. Pan, J.-H. Cheng, H.-M. Chen, M.-C. Tsai, L.-Y. Chen, A. A. Dubale and B.-J. Hwang, *Energy & Environmental Science*, 2016, **9**, 323-356.

32. A. Calloni, A. Abate, G. Bussetti, G. Berti, R. Yivlialin, F. Ciccacci and L. Duò, *The Journal of Physical Chemistry C*, 2015, **119**, 21329-21335.
33. I. Celik, Z. Song, A. J. Cimaroli, Y. Yan, M. J. Heben and D. Apul, *Solar Energy Materials and Solar Cells*, 2016, **156**, 157-169.
34. J.-A. Alberola-Borràs, J. A. Baker, F. De Rossi, R. Vidal, D. Beynon, K. E. A. Hooper, T. M. Watson and I. Mora-Seró, *iScience*, 2018, **9**, 542-551.
35. W. A. Dunlap-Shohl, Y. Zhou, N. P. Padture and D. B. Mitzi, *Chemical Reviews*, 2019, **119**, 3193-3295.
36. Y. Zhou, O. S. Game, S. Pang and N. P. Padture, *The Journal of Physical Chemistry Letters*, 2015, **6**, 4827-4839.
37. G. Niu, W. Li, J. Li, X. Liang and L. Wang, *RSC Advances*, 2017, **7**, 17473-17479.
38. A. R. Pascoe, Q. Gu, M. U. Rothmann, W. Li, Y. Zhang, A. D. Scully, X. Lin, L. Spiccia, U. Bach and Y.-B. Cheng, *Science China Materials*, 2017, **60**, 617-628.
39. X. Zhou, Y. Zhang, W. Kong, M. Hu, L. Zhang, C. Liu, X. Li, C. Pan, G. Yu, C. Cheng and B. Xu, *Journal of Materials Chemistry A*, 2018, **6**, 3012-3021.
40. D. P. McMeekin, G. Sadoughi, W. Rehman, G. E. Eperon, M. Saliba, M. T. Hörantner, A. Haghighirad, N. Sakai, L. Korte, B. Rech, M. B. Johnston, L. M. Herz and H. J. Snaith, *Science*, 2016, **351**, 151-155.
41. N. J. Jeon, J. H. Noh, W. S. Yang, Y. C. Kim, S. Ryu, J. Seo and S. I. Seok, *Nature*, 2015, **517**, 476-480.
42. D. Bi, W. Tress, M. I. Dar, P. Gao, J. Luo, C. Renevier, K. Schenk, A. Abate, F. Giordano, J.-P. Correa Baena, J.-D. Decoppet, S. M. Zakeeruddin, M. K. Nazeeruddin, M. Grätzel and A. Hagfeldt, *Science Advances*, 2016, **2**.
43. S. Draguta, O. Sharia, S. J. Yoon, M. C. Brennan, Y. V. Morozov, J. S. Manser, P. V. Kamat, W. F. Schneider and M. Kuno, *Nature Communications*, 2017, **8**, 200.
44. N. Pellet, P. Gao, G. Gregori, T. Y. Yang, M. K. Nazeeruddin, J. Maier and M. Grätzel, *Angewandte Chemie International Edition*, 2014, **53**, 3151-3157.
45. E. L. Unger, E. T. Hoke, C. D. Bailie, W. H. Nguyen, A. R. Bowring, T. Heumüller, M. G. Christoforo and M. D. McGehee, *Energy & Environmental Science*, 2014, **7**, 3690-3698.
46. B. Chen, M. Yang, S. Priya and K. Zhu, *J. Chem. Phys. Lett.*, 2016, **7**, 905-917.

47. H. J. Snaith, A. Abate, J. M. Ball, G. E. Eperon, T. Leijtens, N. K. Noel, S. D. Stranks, J. T.-W. Wang, K. Wojciechowski and W. Zhang, *The Journal of Physical Chemistry Letters*, 2014, **5**, 1511-1515.
48. M. T. Neukom, S. Züfle, E. Knapp, M. Makha, R. Hany and B. Ruhstaller, *Solar Energy Materials and Solar Cells*, 2017, **169**, 159-166.
49. A. Guerrero, G. Garcia-Belmonte, I. Mora-Sero, J. Bisquert, Y. S. Kang, T. J. Jacobsson, J.-P. Correa-Baena and A. Hagfeldt, *The Journal of Physical Chemistry C*, 2016, **120**, 8023-8032.
50. I. Zarazua, G. Han, P. P. Boix, S. Mhaisalkar, F. Fabregat-Santiago, I. Mora-Seró, J. Bisquert and G. Garcia-Belmonte, *The Journal of Physical Chemistry Letters*, 2016, **7**, 5105-5113.
51. E. J. Juarez-Perez, R. S. Sanchez, L. Badia, G. Garcia-Belmonte, Y. S. Kang, I. Mora-Sero and J. Bisquert, *The Journal of Physical Chemistry Letters*, 2014, **5**, 2390-2394.
52. D. A. Jacobs, H. Shen, F. Pfeffer, J. Peng, T. P. White, F. J. Beck and K. R. Catchpole, *Journal of Applied Physics*, 2018, **124**, 225702.
53. D. Moia, I. Gelmetti, P. Calado, W. Fisher, M. Stringer, O. Game, Y. Hu, P. Docampo, D. Lidzey, E. Palomares, J. Nelson and P. R. F. Barnes, *arXiv*, 2018, 1805.06446v06442.
54. I. Zarazua, J. Bisquert and G. Garcia-Belmonte, *The Journal of Physical Chemistry Letters*, 2016, **7**, 525-528.
55. M. Bag, L. A. Renna, R. Y. Adhikari, S. Karak, F. Liu, P. M. Lahti, T. P. Russell, M. T. Tuominen and D. Venkataraman, *Journal of the American Chemical Society*, 2015, **137**, 13130-13137.
56. Z. Zolfaghari, E. Hassanabadi, D. Pitarch-Tena, S. J. Yoon, Z. Shariatinia, J. van de Lagemaat, J. M. Luther and I. Mora-Seró, *ACS Energy Letters*, 2019, **4**, 251-258.
57. D. Pérez-del-Rey, P. P. Boix, M. Sessolo, A. Hadipour and H. J. Bolink, *The Journal of Physical Chemistry Letters*, 2018, **9**, 1041-1046.
58. R. Frischknecht, N. Jungbluth, H.-J. Althaus, G. Doka, R. Dones, T. Heck, S. Hellweg, R. Hischier, T. Nemecek, G. Rebitzer and M. Spielmann, *The International Journal of Life Cycle Assessment*, 2005, **10**, 3-9.
59. R. K. Rosenbaum, T. M. Bachmann, L. S. Gold, M. A. J. Huijbregts, O. Jolliet, R. Juraske, A. Koehler, H. F. Larsen, M. MacLeod, M. Margni, T. E. McKone, J. Payet, M. Schuhmacher, D. van de Meent and M. Z. Hauschild, *The International Journal of Life Cycle Assessment*, 2008, **13**, 532.

60. Pré Sustainability (2016). SimaPro.
61. O. Jolliet, M. Margni, R. Charles, S. Humbert, J. Payet, G. Rebitzer and R. Rosenbaum, *The International Journal of Life Cycle Assessment*, 2003, **8**, 324.
62. J. M. Ball, M. M. Lee, A. Hey and H. J. Snaith, *Energy & Environmental Science*, 2013, **6**, 1739-1743.
63. D. Pitarch-Tena, T. T. Ngo, M. Vallés-Pelarda, T. Pauporté and I. Mora-Seró, *ACS Energy Letters*, 2018, **3**, 1044-1048.
64. The World Bank Group (2016). Global Solar Atlas. Available at: https://globalsolaratlas.info/ [Accessed November 21, 2018].
65. B. McKenna, J. R. Troughton, T. M. Watson and R. C. Evans, *RSC Advances*, 2017, **7**, 32942-32951.
66. Eurostat (2018). Electricity price statistics - Statistics Explained. Eur. Comm. Available at: https://ec.europa.eu/eurostat/statistics-explained/index.php/Electricity_price_statistics#Electricity_prices_for_non-household_consumers [Accessed November 23, 2018].

SUPPORTING INFORMATION

Flash Infrared Annealing as a Cost-effective and Low Environmental Impact Processing Method for Planar Perovskite Solar Cells

Sandy Sánchez,[1,2†] Marta Vallés-Pelarda,[3†] Jaume-Adrià Alberola-Borràs,[3,4] Rosario Vidal,[4] José J. Jerónimo-Rendón,[1] Michael Saliba,[1*] Pablo P. Boix,[5*] and Iván Mora-Seró[3*]

[1] Adolphe Merkle Institute University of Fribourg Chemin des Verdiers 4, CH-1700 Fribourg, Switzerland.

[2] Laboratory of Photomolecular Science (LSPM) École Polytechnique Fédérale de Lausanne (EPFL), 1015 Lausanne, Switzerland.

[3] Institute of Advanced Materials (INAM), University Jaume I, Avenida de Vicent Sos Baynat, s/n, 12071 Castelló de la Plana, Spain

[4] Department of Mechanical Engineering and Construction, GID, Universitat Jaume I, Av. Sos Baynat s/n, 12071 Castelló de la Plana, Spain

[5] Instituto de Ciencia Molecular (ICMol), Universitat de València, Catedrático José Beltrán, 2, 46980 Paterna, Spain

† Same contribution.

* Corresponding author: miliba@gmail.com, pablo.p.boix@uv.es, sero@uji.es

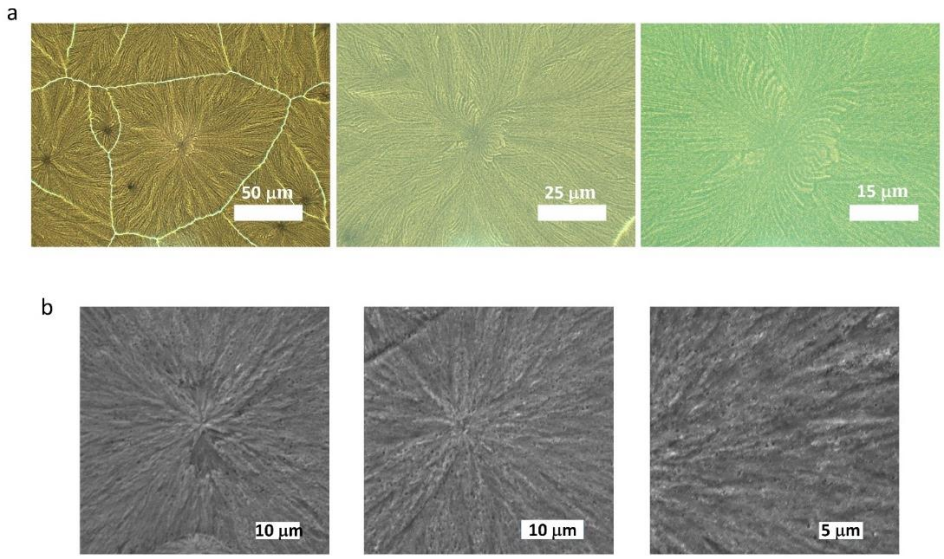

Figure S1. a) Zoom–in of optical microscope images, b) SEM top-view images, for FIRA annealed perovskite films on top of planar electrodes.

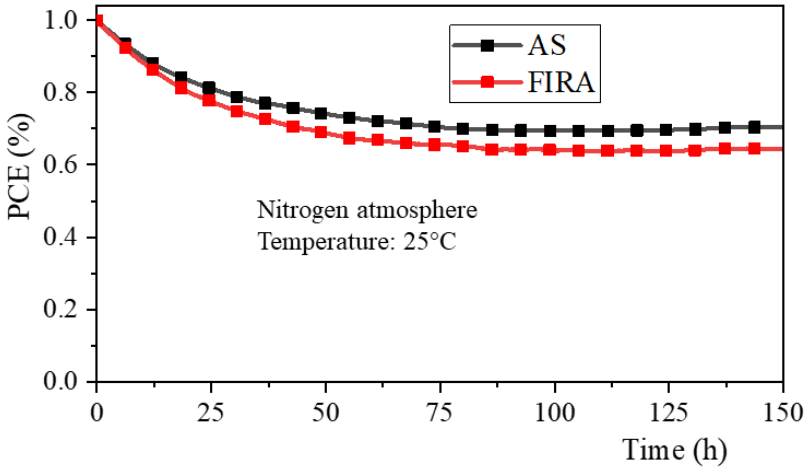

Figure S2. Stability measurement for FIRA and AS samples during 150 h at continuous 1.5 AM illumination at open circuit conditions in nitrogen atmosphere.

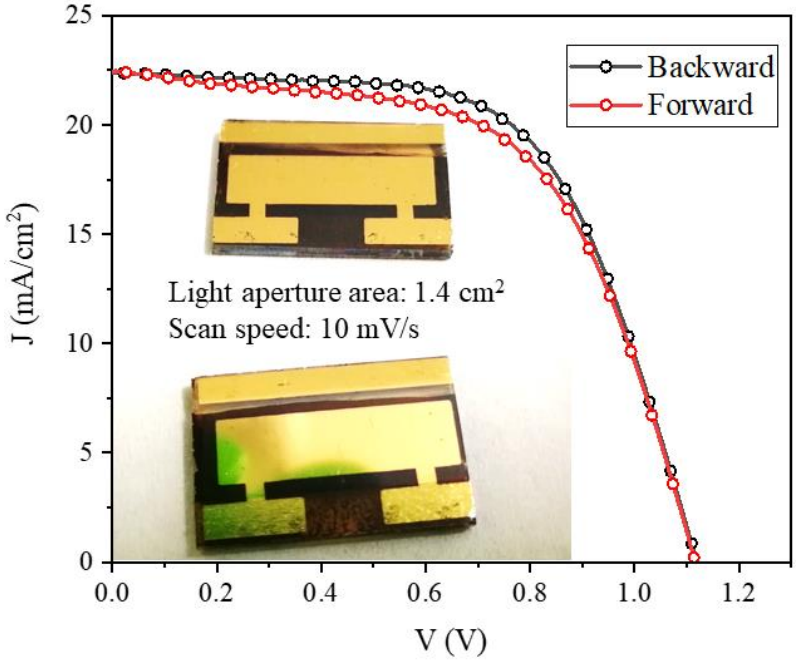

	Jsc (mA/cm²)	Voc (mV)	FF (%)	PCE (%)
Backward	22.4	1119	62	15.4
Forward	22.5	1114	59	14.7

Figure S3. *JV* scan of a large area devices for aperture light mask of 1.4 cm^2 and photovoltaic parameters collected from the measurement.

a b

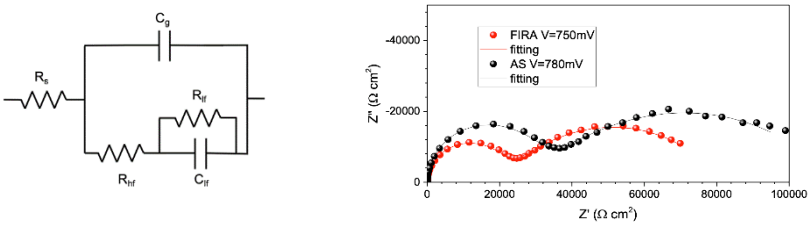

Figure S4. a) Equivalent circuit used for the fitting of impedance spectroscopy data. The capacitors have been modeled by constant phase elements with exponent between 0.8 and 1. b) Example of Nyquist plots obtained for AS and FIRA samples measured at V=Voc. The lines represent the fitting to the equivalent circuit.

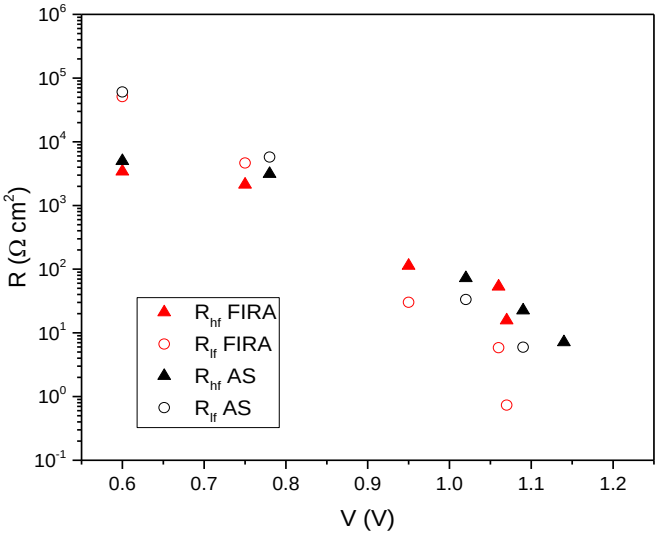

Figure S5. High and low frequency resistances obtained from the fitting of the of impedance spectroscopy data, using the equivalent circuit from Figure S2

Life cycle inventories for 1 kWh

Table S1. Life cycle inventories for 1 kWh for the deposition of the perovskite layer by FIRA and by the antisolvent process

Perovskite deposited by FIRA

Inputs/Outputs	Amount	Unit	Observations
Nitrogen	0.182	g	33.3cm^3/s for FIRA device.
Nitrogen transport	0.025	kgkm	
Fume hood	0.0221	MJ	Exhaust blower, 1/3 hp
Spin coating	0.1058	MJ	Power consumption for vacuum pump and 4000 rpm. 10 s. For 25 cm^2.
FIRA annealing	0.091	MJ	9600 W, 1.2 s, maximum of 150 cm^2
Emissions - Nitrogen (kg)	0.182	kg	

Perovskite deposited by the antisolvent process

Inputs/Outputs	Amount	Unit	Observations
Monochlorobenzene	5.37	g	100µl for each cell.
Nitrogen	0.166	kg	Leak rate of 0.05%volume/h. Nitrogen, liquid, at plant/RER.
Chlorobenzene and Nitrogen transport	0.025	tkm	
Hot plate Annealing (100 ºC 1 h)	1.99	MJ	Power consumption measured for an annealing 100ºC, 1 h and maximum for 400 cm^2.
Spin coating	0.215	MJ	Power consumption for vacuum pump and 4000 rpm. 20 s. For 25 cm^2.
Glove box	0.045	MJ	Pump vacuum of 17 m^3/h.
Emissions - Chlorobenzene	5.37	g	
Emissions - Nitrogen (kg)	0.166	kg	

Table S2. Environmental impacts for the deposition of the perovskite layer by FIRA and by the antisolvent process

	GWP	POP	AP	CED	HTC	HTNC	ET
FIRA	0.03	5.42 10^{-6}	1.36 10^{-4}	0.67	2.18 10^{-9}	8.01 10^{-9}	0.19
Antisolvent	0.38	9.25 10^{-5}	1.80 10^{-3}	8.75	2.96 10^{-8}	1.08 10^{-7}	2.75

Chapter 6. Discussion of the results

Throughout this thesis, several topics associated with perovskite-based photovoltaic and optoelectronic devices have been addressed. There are still some challenges to overcome for a future application of perovskites in commercialized devices. Three approaches have been analysed and studied.

In Chapter 3, perovskite quantum dots are studied to enhance and tune their optical properties. $CsPbBr_3$ QDs are embedded in molecular organogels and their optical properties are evaluated. One of the main properties to study is the photoluminescence and the PLQY. The first effect on the QDs is noticed in this measurement. QDs embedded in one organogelator, Hx, show a notable blueshift in the PL emission wavelength and an increase in the PLQY up to almost unity (Figure 6.1a and b). In addition, the absorption spectra are compared, which also confirm the blueshift of the QDs embedded in Hx organogelator.

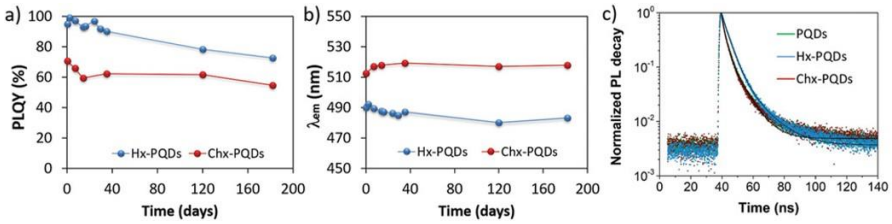

Figure 6.1. a) and b) Evolution of the PLQY and emission wavelength of Hx-PQDs (blue) and Chx-QDs (red). c) TRPL measurements of perovskite QDs (PQDs), Hx-QDs and Chx-QDs. Reproduced with permission from ref.[1] Copyright 2021 John Wiley & Sons, Inc.

Two possibilities are evaluated, an interaction of the perovskite QDs with the organogel acting as a ligand and a reduction in the size. The former can be related to a passivation of the surface and so, to an increase in the PLQY. The latter is well known to be related to a QD blueshift of their emission. In order to determine the origin of this effect two measurements are carried out, the particle size is examined with TEM and the ligands with FTIR. A slight difference in the average size of the QDs and the Hx-QDs is appreciated, which is probably due to the smaller length of the Hx compared to the ligands of the QDs. This reduction can contribute to this blueshift observed, however, this slight

difference does not completely explain the relatively large difference in the PL emission. SAED patterns and HRTEM confirm that the crystal structure of the QDs does not vary. From FTIR measurements (Figure 6.2), a reduction in the intensity of some bands of Hx with QDs is observed, this may indicate an interaction between the QDs and the organogelator. This is also confirmed by TRPL measurements, a longer lifetime is obtained for Hx-QDs and lower non-radiative recombination (Figure 6.1c).

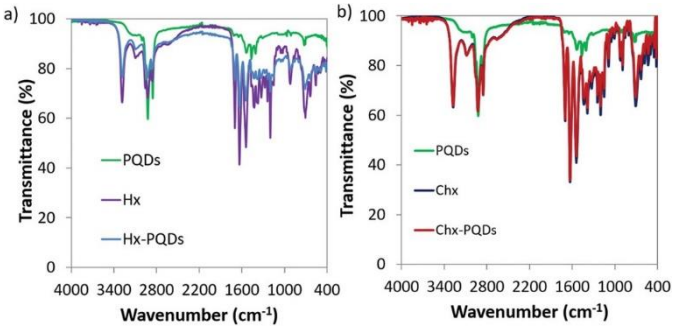

Figure 6.2. a) FTIR spectra of PQDs (green), Hx (purple) and Hx-PQDs (blue). b) FTIR spectra of PQDs (green), Chx (blue) and Chx-PQDs (red). Reproduced with permission from ref.[1] Copyright 2021 John Wiley & Sons, Inc.

The difference in the structure of the organogelators plays an important role, as all these results contrast the Chx-QDs ones. In this case, there is no significant difference between the QDs and Chx-QDs, with exception of an increase in the size. The properties of the organogelators differ in the arrangement when the gel is formed. The difference explains the distinct behaviour of both samples. The self-assembly is more efficient in the Chx, this implies that Chx molecules pack into fibres before interacting with QDs, unlike Hx molecules that can interact before forming the fibres.

Regarding the study of PSCs, two different approaches are evaluated. In Chapter 4, a new type of HTM is studied to replace spiro-OMeTAD, which is the most common material and one of the degradation causes in PSCs. First, the electronic properties of the FU7 are studied. The HOMO and LUMO levels of the new material, FU7, are determined by cyclic voltammetry and are appropriate for our PSCs configuration, as

hole selective contact. Interestingly, this is the first report of a fullerene-based system that can effectively block electrons. In order to evaluate its application in PSCs, devices with different concentrations of FU7 have been prepared. A characterization by SEM has been performed to determine the thickness of the layers as a function of the concentration. In the final devices, FU7 layer has a thickness of around 40nm, while spiro-OMeTAD layer has 200nm. Efficiencies are comparable to those with spiro-OMeTAD, being 13.7 % with FU7 and 16.9% with spiro-OMeTAD. The stability has also been studied for a period of 60 days, both types of samples were stored in dark and in ambient conditions. This study reveals that FU7 improves the stability of the device, probably due to the hydrophobic behaviour of the fullerenes (Figure 6.3d). To further evaluate the role of the fullerene in the performance, a moiety of the FU7 called TAA14 has also been tested as HTM, however, the performance is not as high as with FU7 as HTM. A comparison of the JV curves of all the different devices is shown in Figure 6.3a.

With these results, three advantages are presented. First, the concentration and, consequently, the thickness are lower than the employed for spiro-OMeTAD. Secondly, a similar efficiency is obtained without any additive. In respect of the use of additives, the effect of the same additives employed in spiro-OMeTAD has also been studied; however, the use of these specific additives is not beneficial for this HTM. And the last one, FU7 slightly increases the stability of PSCs.

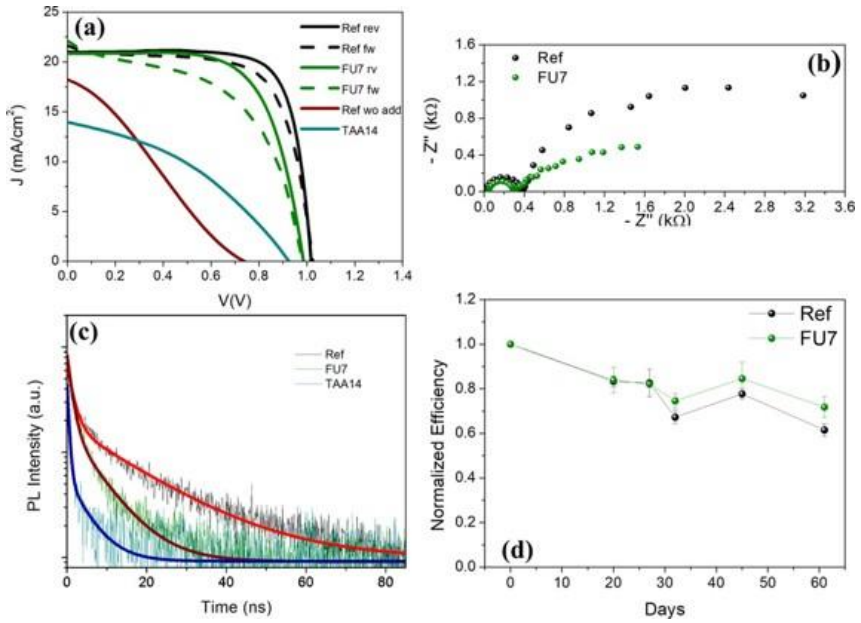

Figure 6.3. a) JV curves of the different devices prepared: reference with spiro-OMeTAD (Ref), reference with spiro-OMeTAD without additives (Ref wo add), with the new HTM (FU7) and with the functional group of the new HTM (TAA). b) Nyquist plot of reference device and FU7 device at 0.6V. c) TRPL measurements of reference sample, sample with FU7 and sample with TAA. d) Stability of the devices: reference and devices with FU7. Reproduced with permission from ref.[2] Copyright 2018 John Wiley & Sons, Inc.

From TRPL and IS measurements, a higher recombination rate is observed in FU7 samples (Figure 6.3b and c). This explains the lower photovoltage of these devices. Finally, the first fullerene-sandwich PSCs has been prepared and characterized without further optimization. The ETM employed is C_{60} and the efficiency obtained is around 9%.

And in Chapter 5, FIRA, a new method for preparing the perovskite film, is studied in planar PSCs. The photoluminescence and morphology are characterized and compared with films prepared by AS method. Although FIRA samples have larger domains, both films are pinhole-free and present similar emission and XRD patterns. We evaluate the influence of this different morphology in the solar cell performance and its working principles. Regarding the performance of PSCs prepared by both methodologies (Figure 6.4), they have comparable and reproducible parameters; FIRA champion SC has around 18% efficiency, more than 70% FF, 1.073-1.087 V and 22.5-

22.8 mA/cm^2, and antisolvent (AS) champion PSC has around 18% efficiency, more than 70% FF, 1.082-1.096 V and 23 mA/cm^2.

The values obtained for the capacitive and resistive parameters from IS measurements confirm that both types of PSCs have similar working principles. In addition, LCA, which analyses the impact of the perovskite deposition method on the environment and cost, reveals that FIRA method reduces both. This difference is mainly due to the energy consumption of the thermal annealing and the higher volume of solvent employed in the AS method.

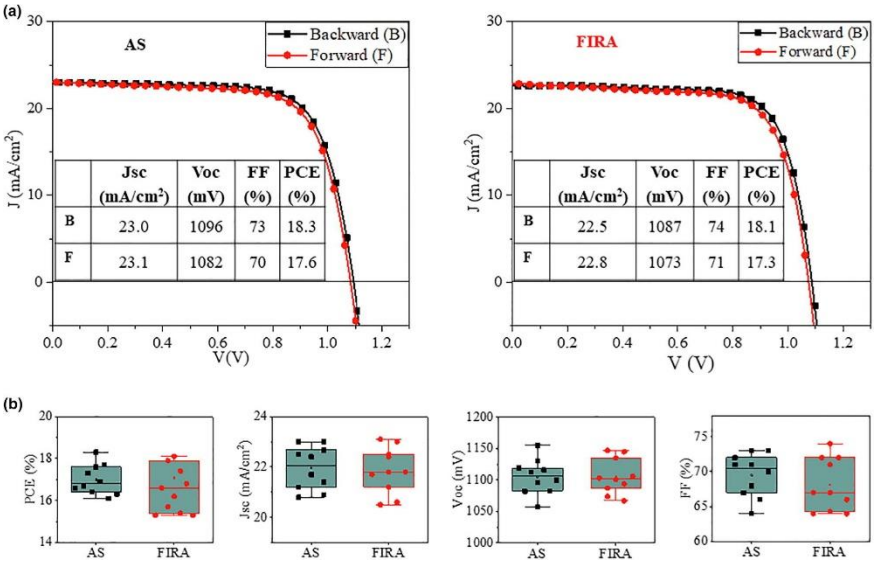

Figure 6.4. (a) JV curves of champion devices and (b) comparison of the photovoltaic parameters of the samples prepared by antisolvent method (AS) and prepared by FIRA method. Reproduced from ref.[3], Creative Commons license CC-BY-NC-ND http://creativecommons.org/licenses/by-nc-nd/4.0/.

References

[1] M. Vallés-Pelarda, A. F. Gualdrón-Reyes, C. Felip-León, C. A. Angulo-Pachón, S. Agouram, V. Muñoz-Sanjosé, J. F. Miravet, F. Galindo, I. Mora-Seró, *Adv. Opt. Mater.* **2021**, *n/a*, 2001786.

[2] S. F. Völker, M. Vallés-Pelarda, J. Pascual, S. Collavini, F. Ruipérez, E. Zuccatti, L. E. Hueso, R. Tena-Zaera, I. Mora-Seró, J. L. Delgado, *Chem. – A Eur. J.* **2018**, *24*, 8524.

[3] S. Sánchez, M. Vallés-Pelarda, J.-A. Alberola-Borràs, R. Vidal, J. J. Jerónimo-Rendón, M. Saliba, P. P. Boix, I. Mora-Seró, *Mater. Today* **2019**, *31*, 39.

Chapter 7. General conclusions

In this Chapter, general conclusions of the contributions here presented are exposed. In this thesis, diverse strategies have been applied to perovskite-based systems for improving different crucial aspects. The different works contribute to enhance the optoelectronic properties of PQDs, to eliminate the use of additives in the HTM for the fabrication of photovoltaic devices and, moreover, to study a methodology which can be incorporated in up-scaling procedures towards their future commercialization as solar cells.

A potential application of amino acid derivatives as postsynthetic treatment for PQDs has been presented. $CsPbBr_3$ PQDs are embedded in two different molecular organogelators, Hx and Chx. The slightly different structure of these organogelators has an effect on the PQDs emission, enabling the obtention of green or blue emission. Hx-PQDs gel shows a blue emission with high stability and high PLQY, almost unity. This shift to blueish emission enhancing PLQY is especially interesting as chloride-based halide perovskite, with band gap in the blue spectral region, presents lower PLQY than bromide and iodide counterparts. From the characterization of Hx-PQDs, we concluded that the increase in the PLQY and the blueshift indicate that the organogel is interacting with the PQDs surface. In the case of Chx-PQDs, this organogelator is more prone to self-associate, which may complicate the interaction. Here, a redshift is observed, but it is attributed to the size increase of the PQDs due to the heating step.

A novel HTM for PSCs in regular architectures has been reported. A fullerene derivative, FU7, successfully replaces the most employed HTM, spiro-OMeTAD. The fullerene has been chemically modified to obtain a new molecule with appropriate energy levels (HOMO and LUMO) to promote hole transport and block electrons. The most remarkable feature, beyond being a fullerene-based electron blocking material, is that it does not need the additives that spiro-OMeTAD requires, which are known for their role in the degradation of the PS. Moreover, SCs with FU7 show higher stability compared with those using spiro-OMeTAD. Regarding the performance, comparable

efficiencies are obtained with this new HTM, around 80% of the value of the reference SCs with spiro-OMeTAD.

Finally, an innovative methodology to prepare perovskite layers for planar PSCs has been studied. PSCs prepared with FIRA have similar efficiency and properties to those prepared with antisolvent methodology. SEM measurements reveal that their morphology is different, however, it does not affect the photoconversion efficiency, optoelectronic properties and working principles. The use of solvents and the annealing time are reduced, which are important features towards future up-scaling and commercialization, in addition to decrease significantly the environmental impacts.

This thesis highlights how the interaction of halide perovskites with other materials can tune the emission or photovoltaic properties of the system, becoming an enormously valuable tool not only to optimize devices, but to pave the way to advanced configurations and applications. In addition, halide perovskite fabrication methodologies have to be considered for fabrication of efficient devices in large areas, reducing environmental impact. In this sense, the Flash Infrared Annealing is a smart solution able to be applied in a friendly industrial environment with dramatically reduced environmental impacts.

The different works presented here serve as a basis for diverse research lines. Based on the molecules employed in the work with quantum dots, a design of new derivatives can be studied in order to contribute to a further enhancement of the properties and to ease their incorporation into optoelectronic devices. Moreover, the works focused on solar cells could be combined, preparing devices with the new hole transporting material and the deposition of the perovskite by the new method. Other future research could be the employment of this new method with flexible substrates, followed by analysis and characterization, both in film and devices.

Chapter 8. Conclusiones generales

En este capítulo se presentan las conclusiones de las contribuciones aportadas. En esta tesis, se han implementado diferentes estrategias a sistemas basados en perovskita para mejorar varios aspectos cruciales. Los diferentes trabajos contribuyen a mejorar las propiedades optoelectrónicas de puntos cuánticos de perovskita (PQDs), a eliminar el uso de aditivos en el material transportador de huecos (HTM) en dispositivos fotovoltaicos y, además, a estudiar una metodología que se pueda implementar en procesos a gran escala para la futura comercialización de celdas solares de perovskita.

Se ha desarrollado una aplicación de derivados de aminoácidos como tratamiento después de la síntesis. Se han incorporado $CsPbBr_3$ PQDs en dos organogelantes moleculares diferentes, Hx y Chx. La pequeña diferencia en la estructura de éstos tiene un efecto en la emisión, permitiendo obtener una emisión verde o azul. El gel Hx-PQDs tiene una emisión azul estable y un alto rendimiento cuántico de fotoluminiscencia (PLQY). Este desplazamiento hacia emisiones en el azul, mejorando el PLQY, es especialmente interesante debido a que las perovskitas que emiten en esa región, las perovskitas en las que el haluro es el cloruro, tienen menor PLQY que las que contienen bromo o yodo. De la caracterización de Hx-PQDs, se concluyó que el incremento en el PLQY y el desplazamiento hacia el azul se debe a la interacción de los organogelantes con la superficie de los PQDs. En el caso de Chx-PQDs, este organogelante es más propenso al autoensamblaje molecular, lo que dificulta la interacción. En este caso, se observa un desplazamiento hacia mayores longitudes de onda, pero se puede asociar al incremento del tamaño de los puntos cuánticos en el tratamiento con calor.

Se ha estudiado un nuevo HTM para celdas solares de perovskita. Es un derivado del fullereno, FU7, con el que se ha demostrado que puede reemplazar al HTM más utilizado, spiro-OMeTAD. El fullereno ha sido modificado químicamente para obtener este derivado con niveles de energía (HOMO y LUMO) apropiados para promover el transporte de

huecos y bloquear los electrones. La característica más destacable, además de ser un material derivado de fullerenos bloqueador de electrones, es que no necesita los aditivos que spiro-OMeTAD requiere, que tienen un papel en la degradación de la perovskita. Además, las celdas solares con FU7 muestran mayor estabilidad respecto a las fabricadas con spiro-OMeTAD. En relación a la eficiencia con el nuevo HTM, se obtuvieron valores alrededor del 80% respecto a las eficiencias obtenidas en las celdas solares con spiro-OMeTAD.

Por último, se ha estudiado una metodología innovadora para la preparación de las capas de perovskita en celdas solares de capa fina. Las celdas solares preparadas con la nueva metodología, FIRA, tienen eficiencias y propiedades similares a las muestras preparadas por uso de antisolvente. La caracterización por SEM muestra una morfología diferente, sin embargo, no afecta a la eficiencia, propiedades optoelectrónicas y su funcionamiento. El uso de disolventes y el tiempo de tratamiento de la muestra se reducen significativamente, lo cual es una característica muy importante para su futura preparación a gran escala y su comercialización, además de reducir considerablemente el impacto medioambiental.

Esta tesis resalta como la interacción de las perovskitas de haluro con otros materiales puede variar la emisión o las propiedades fotovoltaicas del sistema, siendo una herramienta muy valiosa tanto para optimizar dispositivos como para abrir camino hacia otras configuraciones y aplicaciones. Además, las metodologías de preparación de perovskitas de haluro deben dirigirse hacia la fabricación de dispositivos eficientes a gran escala, reduciendo el impacto medioambiental. FIRA es una solución que permite aplicar estos métodos a la industria reduciendo drásticamente el impacto medioambiental.

Los diferentes trabajos presentados sirven como base para diversas líneas de investigación. A partir de las moléculas utilizadas en el trabajo de los puntos cuánticos, se pueden diseñar derivados de éstas que aporten una mayor mejoría de sus propiedades y faciliten su incorporación a dispositivos optoelectrónicos. Asimismo, los trabajos enfocados a la fabricación de celdas solares podrían combinarse, preparando así dispositivos con el nuevo material transportador de

huecos y la deposición de perovskitas por el nuevo método. Otra posible futura investigación podría ser la utilización de este método de deposición de la perovskita en substratos flexibles, seguido de su análisis y caracterización, tanto en capa como dispositivos.

Annex I. List of publications

Publications included in this PhD thesis:

1. Sebastian F. Völker, Marta Vallés-Pelarda, Jorge Pascual, Silvia Collavini, Fernando Ruipérez, Elisabetta Zuccatti, Luis E. Hueso, Ramón Tena-Zaera, Iván Mora-Seró, Juan Luis Delgado. Fullerene-Based Materials as Hole-Transporting/Electron Blocking Layers. Applications in Perovskite Solar Cells. Chemistry - A European Journal, 2018, 24,34, 8524-8529.
2. Sanchez, S.; Vallés-Pelarda, M.; Alberola-Borràs, J.A.; Vidal, R.; Jerónimo-Rendón, J.J.; Saliba, M.; Boix, P.P.; Mora-Seró, I. Flash infrared annealing as a cost-effective and low environmental impact processing method for planar perovskite solar cells. Materials Today, 2019, 31, 39-46.
3. M. Vallés-Pelarda, A. F. Gualdrón-Reyes, C. Felip-León, C. A. Angulo-Pachón, S. Agouram, V. Muñoz-Sanjosé, J. F. Miravet, F. Galindo, I. Mora-Seró, Adv. Opt. Mater. 2021, 2001786

Publications not included in this PhD thesis:

1. Belarbi, E.; Vallés-Pelarda, M.; Clasen, B.; Sánchez, R.; Barea, E.M.; Maghraoui-Meherzi, H.; Mora-Seró, I. Transformation of PbI2, PbBr2 and PbCl2 salts into MAPbBr3 perovskite by halide exchange as an effective method for recombination reduction. Physical Chemistry Chemical Physics, 2017, 17, 10913.
2. Fabregat-Santiago, F.; Kulbak, M.; Vallés-Pelarda, M.; Hodes, G.; Cahen, D.; Mora-Seró, I. Deleterious Effect of Negative Capacitance on the Performance of Halide Perovskite Solar Cells. ACS Energy Letters, 2017, 2, 2007-2013.
3. Contreras-Bernal, L.; Aranda, C.; Vallés-Pelarda, M.; Ngo, T.T.; Ramos-Terrón, S.; Gallardo, J.Jesús; Navas, J.; Guerrero, A.; Mora-Seró, I.; Idígoras, J.; Anta, J.A. Homeopathic Perovskite Solar Cells: Effect of Humidity during Fabrication

on the Performance and Stability of the Device. The Journal of Physical Chemistry C, 2018, 122, 5341−5348.

4. Pitarch-Tena, D.; Ngo, T.T.; Vallés-Pelarda, M.; Pauporté, T.; Mora-Seró, I. Impedance Spectroscopy Measurements in Perovskite Solar Cells: Device Stability and Noise Reduction. ACS Energy Letters, 2018, 3, 1044-1048.
5. Suárez, I.; Vallés-Pelarda, M.; Gualdrón-Reyes, A.Fabián; Mora-Seró, I.; Ferrando, A.; Michinel, H.; Salgueiro, J.Ramón; Pastor, J.P.Martine Outstanding nonlinear optical properties of methylammonium- and Cs-PbX3 (X = Br, I, and Br–I) perovskites: Polycrystalline thin films and nanoparticles. APL Materials, 2019, 7, 41106.
6. Suri, M.; Hazarika, A.; Larson, B.W.; Zhao, Q.; Vallés-Pelarda, M.; Siegler, T.D.; Abney, M.K.; Ferguson, A.J.; Korgel, B.A.; Luther, J.M. Enhanced Open-Circuit Voltage of Wide Bandgap Perovskite Photovoltaics by Using Alloyed (FA1−xCsx)Pb(I1−xBrx)3 Quantum Dots. ACS Energy Letters, 2019, 4, 1954−1960.